POLITECNICO DI MILANO

Facoltà di Ingegneria Industriale

Corso di Laurea in
Ingegneria Meccanica

A study on surface finish and electric signal of a PZT piezoelectric ceramic machined by abrasive water jet

Supervisori: Prof. Massimiliano ANNONI
Prof. Dragos AXINTE

Tutor: Dr. Amir RABANI

Tesi di Laurea di:
Federico ATTUATI

Matricola 770008

Anno Accademico 2011 - 2012

To my family and my girlfriend for their constant support in this long journey

Contents

List of Abbreviations

ANOVA	Analysis of variance
AWJ	Abrasive water jet
BNC	Bayonet Neill-Concelman
DOE	Design of experiments
EDM	Electrical discharge machining
FFT	Fast Fourier transformation
FIR	Finite impulse response
PSD	Power spectral density
PZT	Lead titanate zirconate
PWJ	Pure water jet
RMS	Root mean square
SEM	Scanning electron microscope
SiC	Silicon carbide
WJ	Water jet

List of Symbols

D	Electric displacement
d	Piezoelectric constant
E	Electric field
E_{c}	Coercive electric field
g	Gravitational acceleration
H_{t}	Hardness of target material
H_{p}	Hardness of particle
L	Evaluation length
L_{c}	Characteristic length describing the resistance of materials
K_{c}	Fracture toughness
p_0	Water relative pressure before the orifice
p_1	Water relative pressure after the orifice
P_{oil}	Oil pressure
P_{water}	Water pressure
R_{a}	Surface roughness
R_{z}	Ten-point mean roughness
S	Mechanical strain
S_{oil}	Water pressure application section
s^{E}	Elastic compliance constant at constant electric field

S_{water}	Oil pressure application section
T	Mechanical stress
T_{c}	Curie point
V_0	Speed of water before the orifice
V_1	Speed of water after the orifice
X_{RMS}	RMS of the vector X
z_0	Vertical position before the orifice
z_1	Vertical position after the orifice
α	Significance level of the test
γ	Specific weight of water
ε^{T}	Dielectric constant under constant stress
λ_{c}	Cut-off length
ρ	Water density

Abstract

Piezoelectric ceramics can satisfy the needs of optical, electronic, mechanical and biomedical applications thanks to their properties such as electrical behaviour and electromagnetic response, high mechanical and corrosion resistance, high resistance to thermal stresses and chemical inertness. As these type of material are generally difficult to machine by conventional technologies, abrasive water jet is a promising technology compared to laser, EDM or micromachining thanks to the low forces involved in the cut, the absence of thermal stresses, high versatility and flexibility. The work will demonstrate the capability of water jet technology to successfully machine such materials, investigate the effect of process parameters on the surface finish of a thin sheet of a piezoelectric ceramic called lead zirconate titanate (PZT) and analyze the electric signal directly acquired from the workpiece during the cut in order to have a deeper understanding of the cutting process and jet-piece interaction.

Keywords: Piezoelectric, ceramic, PZT, abrasive water jet, roughness, electric signal.

Sommario

Le ceramiche piezoelettriche possono soddisfare i bisogni di molteplici applicazioni in numerosi campi, come ad esempio quello ottico, elettronico, meccanico e biomedico, grazie all'accoppiamento elettromeccanico dovuto all'effetto piezoelettrico e alle loro proprietà quali l'alta resistenza meccanica, alla corrosione, agli stress termici e l'inerzia chimica. Generalmente questo tipo di materiali è difficile da lavorare con tecnologie convenzionali e innovative come il laser, l'EDM o le microlavorazioni. La tecnologia water jet, al contrario, risulta promettente poiché presenta basse sollecitazioni meccaniche e termiche unitamente ad un'alta flessibilità e versatilità. Questo lavoro dimostrerà la capacità della tecnologia water jet di lavorare con successo una ceramica piezoelettrica chiamata zirconato titanato di piombo (PZT). Verrà investigata la finitura superficiale del taglio e analizzato il segnale elettrico acquisito direttamente dal pezzo in lavorazione nel tentativo di aumentare le conoscenze sul processo di taglio e sull'interazione getto-materiale.

Parole chiave: Piezoelettricità, ceramica, PZT, abrasive water jet, rugosità, segnale elettrico.

Chapter 1

Introduction and State of Art

1.1 Introduction

Piezoelectric ceramics are nowadays widely used thanks to their capability to transform an electrical field into a mechanical displacement and vice versa in addition to the high hardness, the wear resistance, the thermal resistance and the chemical inertness typical of a ceramic material. Their peculiar property makes them particularly suitable for a number of applications, for example sensors, actuators, transducers or generators. However, conventional machining methods such as grinding, turning or diamond wheel machining are expensive. In fact, the brittle behavior of the material makes it hard to obtain a high dimensional precision, while the high hardness causes a severe tool wear. Moreover, the shapes of the features cannot be too complex because of the limitation imposed by the tool geometry. Electrical discharge machining can achieve strict geometrical tolerances and can machine complex geometries but can be used only with conductive materials. Thermal damage can occur with laser machining, thus deteriorating the performance of the final product. On the other hand, water jet is an appealing technology thanks to the low mechanical and thermal stress during the cut and the absence of chemical alterations.
The aim of this work is to demonstrate that a hard-to-cut material as a piezoelectric ceramic can be successfully machined with a water jet, to investigate the surface finish of the kerf and to analyze the electrical signal collected from the workpiece during the cut since useful information regarding the cutting process can be obtained from it. To have a better insight into the microstructural aspects and to better understand the interaction between the material and the water jet, a SEM analysis has been performed.
The first chapters will introduce the water jet technology and explain the characteristic of the ceramic material employed in the work. The following chapters will give a detailed description of the experimental work and of the used procedure. Lastly, conclusions and possible future developments will be presented.

1.2 State of art

Abrasive water jet technology is relatively young and various aspects, like the jet structure or the material – jet interaction, are still being investigated. The erosion mechanisms of ductile material are known thanks to the works of Finnie [1][2] and Hashish [3][4][5]. However, brittle materials exhibit a more complex behavior still not completely assessed. A few models for abrasive water jet machining of brittle materials have been proposed. They are based on the indentation fracture mechanics, as the damage pattern observed in the experiments is similar to the one observed in the quasi-static indentation tests with diamond indenters. The material removal is based on formation and propagation of cracks. The impact zone is surrounded by median-radial cracks and presents an irreversible deformation. During the unload phase, if the load exceeds a threshold value, lateral cracks are developed thus leading to chipping and, consequently, to erosion [6].

Despite the fact that ceramics are brittle materials, it is believed that plastic deformation takes part in the erosion mechanism [7]. In [8] the researchers found proofs of ductile erosion if the kinetic energy is below a threshold value.

This idea is confirmed in [9][10]. The authors present evidences of development of high local temperatures due to abrasive high energy and low thermal conductivity of ceramics. The presence of such high temperatures leads to chemical reactions (e.g. oxidation) and softening of the material, which can consequently show a plastic behavior.

There exist some predictive models for brittle materials which consider plastic deformation mechanism: two elastic-plastic models are presented in [11] for predicting the depth of cut. Both models include fracture toughness K_c into the formulation and one of them starts from the assumption that plastic deformation is relevant in material removal mechanisms. Zeng and Kim [12] present a model for the prediction of material removal rate for brittle materials. They consider the total eroded volume to be the sum of volume eroded by plastic flow, which is predicted using Finnie's model, and volume eroded by brittle fracture.

However, models start from the assumption that abrasive particles are infinitely hard and rigid. [13][14][15] demonstrate that this is a correct assumption when the ratio between material hardness H_t (target hardness) and abrasive hardness H_p (particle hardness) is << 1. An indention-induced fracture mechanism is observed in this case and the machined surface shows an high wear. When the ratio tends to the unity, the value of material removal rate considerably drops, the microchipping erosion mechanism becomes dominant and the surface is smoother. Models based on infinitely hard abrasive are not valid in this situation anymore.

Abrasive energy is another important factor that must be taken into account when discussing cutting mechanisms. [9][10][16] show the presence of two

different removal mechanisms in brittle materials according to the energy density. In fact, two different wear zones are observable. In the upper side of the kerf, where abrasive still has a high amount of energy, transgranular fractures and microcutting occur. Moreover, the grains and the binder are equally eroded. Conversely, intergranular cracking dominates the lower part of the surface and the erosion occurs on the softer binder, while the grains fall apart as the matrix is eroded. Non-linear fracture phenomena such as crack arrest and crack branching have been observed in [16]. [17] suggests to use a characteristic length L_c to describe the resistance of strain-softening materials to a jet impact.

The surface roughness is not usually the main topic in water jet papers, and few works can be found specifically on it. Hocheng and Chang [18] affirm that, when machining Al_2O_3 and Si_3N_4 ceramics, the roughness increases with the feed rate, while an increase in abrasive mass flow helps to improve the surface finish. Pressure provides the energy to cut thicker materials, but has no relevant effect on the roughness. In [19] roughness is modeled using artificial neural network and regression analysis method. In [1] an investigation on the finish of metals is carried out. The decrease in feed rate improves the surface finish, which, on the other hand, gets worse with the increase in thickness. [20] presents an optimization of the cutting parameters to obtain the best kerf quality of a thin sheet of a piezoelectric ceramic.

Despite the efforts and the knowledge already acquired on the water jet technology, more studies are required for a deeper understanding and a better control of the water jet machining process of ceramic materials. This work will contribute to the study of surface finish of ceramics machined by abrasive water jet and to the study of the interaction between the jet and the material.

Chapter 2

Water Jet Technology

Water jet (WJ) is a non-conventional technology with its strength lying in simplicity and flexibility in addition to some peculiarity of the process which will be explained later in this chapter.
Simplicity can be found in the operating principle: water is pressurized up to 600 MPa in a hydraulic circuit by a pump, then is let flow through a small hole named orifice which converts water pressure into speed. In this way, water can reach speeds higher than 800 m/s. Flexibility comes from the ability of water jet technology of machining virtually every material and cutting shapes both in 2D and 3D; the maximum piece thickness that can be cut depends only on the maximum water pressure provided by the pump. Water has been chosen for carrying energy because it is characterized by large availability, low costs and no environmental issues.
First experiments date to 1950's, when Norman Franz, a forestry engineer, started experimenting which high pressure water to cut trees into lumber. His experiments did not lead to a successful commercial cutting machine but they prove that water under high pressure and high velocity could cut materials.
However, the technology did not advance considerably until 1970's, when Mohamed Hashish had the idea of introducing abrasive into the jet; this represented the turning point of water jet technology, allowing the WJ technology to expand its application field. Since then, many types of water jet have been developed, including abrasive water jets, cavitation jets, ice water jets, hybrid jets [21]. The possibility to easily cut a wide variety of materials and shapes, the low forces transmitted to the workpiece, the absence of heat affected zone and the environmental sustainability make WJ a particularly suitable and competitive technology for modern unconventional machining.

2.1 Water jet classification

As stated before, various types of jets have been developed to satisfy the needs of particular applications. However, the most common classification of water jets focuses on the presence of abrasive into the flow, resulting in a division into two groups: pure water jets (PWJ) and abrasive water jets (AWJ)
Pure water jet relies only on the cutting power of the water stream. Orifice with small diameters, usually between 0.05 and 0.15 mm, focalizes the jet in order to have a small impinging area and an high density of energy. PWJ is suitable for cutting softer materials such as food, paper, wood, fabric and leather. PWJ problems are related to the failure or the clogging of the orifice, but a proper purification of the water can extend the life and the efficiency of this component.

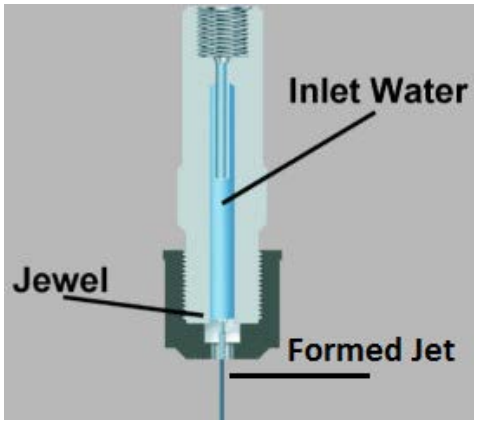

Figure 2.1: Pure water jet cutting head [22]

Harder materials such as ceramics, metals and glass cannot be machined using a pure water jet. Abrasive water jet technology has been developed to compensate the lack of cutting power of a pure water jet. A sand, usually garnet, is added to the stream in a component called mixing chamber, usually placed below the orifice, where the flowing water creates a suction effect which makes the abrasive enter the jet. After that, a focusing nozzle makes the jet coherent.
On the contrary of what happens in pure water jetting, water is now used to accelerate and direct the abrasive against the workpiece rather than a tool for machining the workpiece. In fact, the actual cutting is performed by the abrasive, which has a hardness equal or greater than the hardness of the target material.

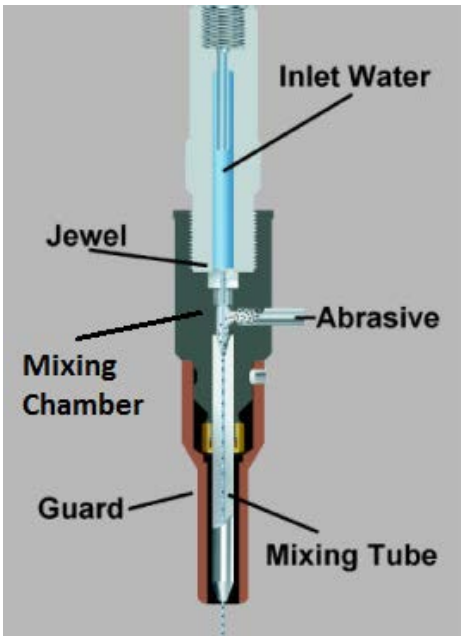

Figure 2.2: Abrasive water jet cutting head [22]

To drag abrasive more efficiently, water flow is increased by means of bigger diameters compared to the ones of a pure water jet machine. The orifice diameter is usually 0.3 mm and the focuser is three times bigger, having a diameter of 1.02 mm. The length of the focusing nozzle is usually 76 mm.
An abrasive water jet machine is more expensive in respect to a pure water jet machine. The higher costs are caused by a more complex set up (a feeder for the abrasive, the mixing chamber), by the abrasive itself and by the wear of the focusing tube caused by the fact that the AWJ machine erodes itself; the nozzle has a cost of 80-100 € and last for 80-100 hours when the abrasive used is garnet and less if the abrasive is harder as alumina or silicon carbide. The substitution of the focuser, together with abrasive, is a large part of operative costs.
Another issue of AWJ machining is the formation of agglomerates of abrasive in the focuser which lead to an arrest of the process. However, with new and improved designs of the mixing chamber, this occurrence is becoming less and less present.
In conclusion, abrasive water jetting is a more powerful but also more delicate and costly technology compared to pure water jetting. For soft materials, the better choice is PWJ due to the lower costs involved, whereas the AWJ is the only solution for machining metals and ceramics.

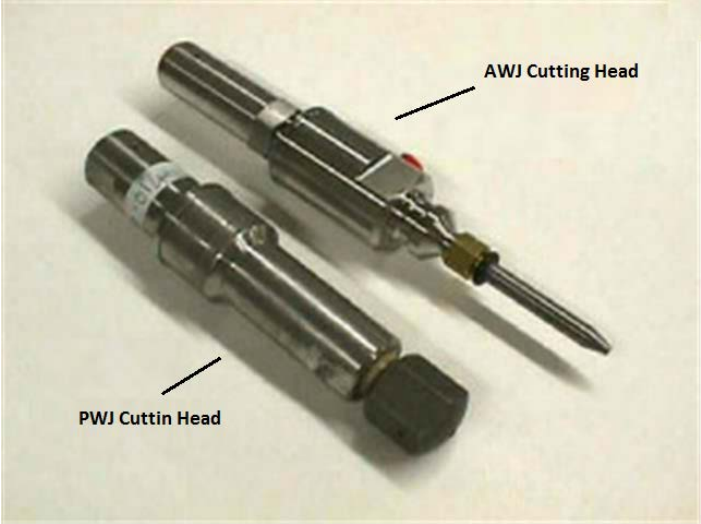

Figure 2.3: Water jet cutting heads [22]

2.2 The water jet system

This section will explain in detail the composition of a water jet machine.
A water jet system is composed by [23]:

- Water treatment system
- Low-pressure circuit (oil)
- Pumping system
- High-pressure circuit (water)
- Cutting head
- Abrasive feeder (only abrasive water jet)
- Catcher

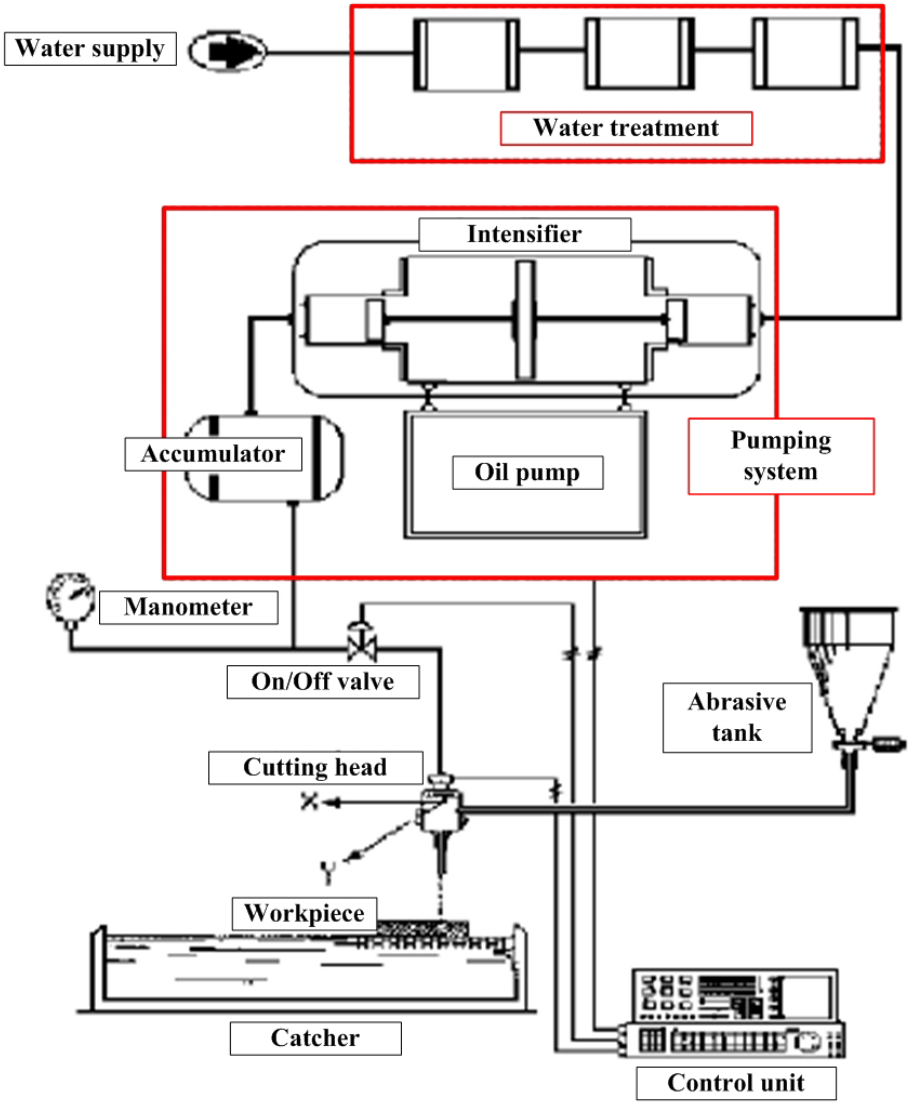

Figure 2.4: Abrasive water jet plant [24]

2.2.1 The water treatment system

The water treatment system is needed for filtering the water coming from the water network and is designed specifically for the characteristic of the water supply. It usually consists of micrometrics filters, carbon filters and an inverse osmosis apparatus intended to eliminate solid particles and some chemical elements like calcium, magnesium, chlorides and sulfides known to be detrimental to the water jet system. In fact, solid particles accelerate the wear of pumping system, pipes, valves, orifice and focuser, while calcium and

magnesium are known to form deposits which cause inefficiencies leading to pressure drops. Lastly, chlorides and sulfides lead to corrosion of metallic parts. The water treatment system is thus necessary for granting the correct functioning of a water jet machine.

2.2.2 The pumping system

The pumping system is the heart of a water jet machine. Its task is to raise water pressure to the value used in the process, usually between 200 and 600 MPa. It is composed by a pressure intensifier, a water accumulator, an oil accumulator and an hydraulic pump. In the pumping system, the pressure in the oil circuit is increased and transmitted to the water circuit thanks to the equilibrium of forces principle. The hydraulic pump is used to compress the oil, while the intensifier is the part in contact both with water and oil in which the transformation occurs. The equation describing the phenomenon, graphically represented in **Figure 2.5**, is the following:

$$P_{\text{water}} \cdot S_{\text{water}} = P_{\text{oil}} \cdot S_{\text{oil}} \tag{2.1}$$

$$P_{\text{water}} = P_{\text{oil}} \cdot \frac{S_{\text{oil}}}{S_{\text{water}}} \tag{2.2}$$

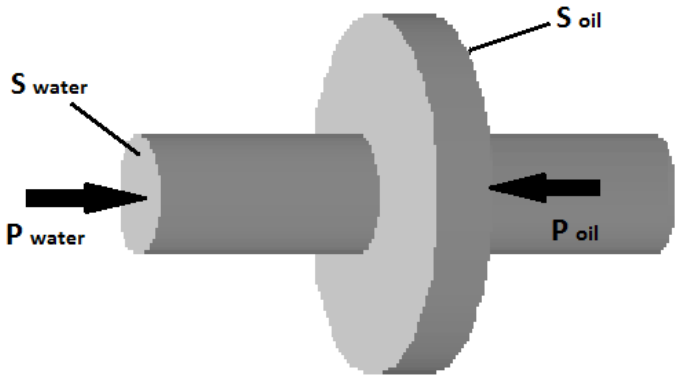

Figure 2.5: Equilibrium of forces principle applied to the intensifier [23]

The oil chamber is at low pressures but the area of application of the pressure is big, while the water side has a smaller section, therefore allowing the water to reach high pressures. Common values for the intensification ratio (the ratio $\frac{P_{\text{water}}}{P_{\text{oil}}}$) are between 10 and 40.

There are two types of intensifiers: single-acting and double-acting (**Figure 2.6**). Single-acting intensifiers can pressurize the water only in the compression stroke and, in order to obtain an adequate water flow and reduce water pressure fluctuations, there should be at least two of them in the machine. To increase the

maximum water flow and reduce even more the pressure fluctuations, three or more intensifiers can be used; however, attention must be paid to their phasing. Double effect intensifiers, instead, pressurize water in each stroke direction.

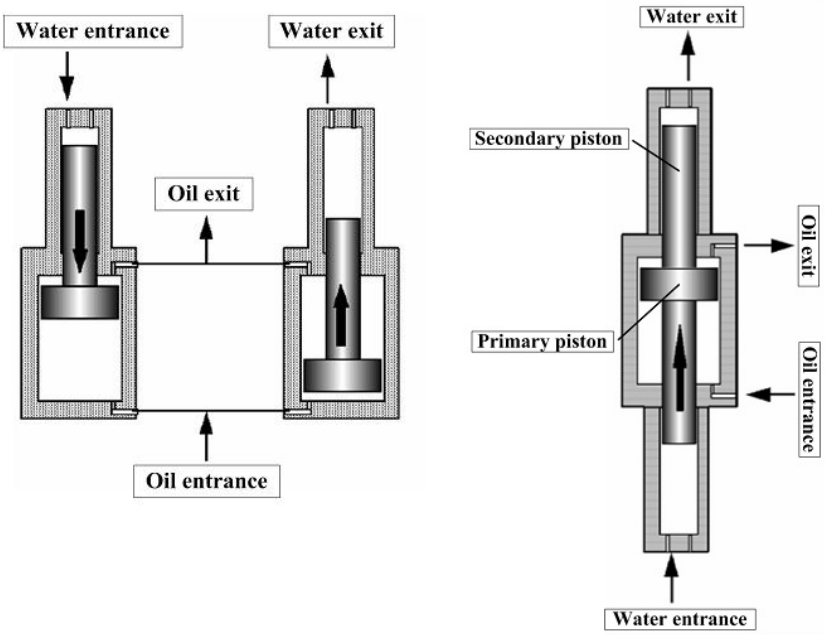

Figure 2.6: Single-acting intensifier (left) and double-acting intensifier (right)

In a pumping system there are two accumulators, one for the water circuit and one for the oil circuit, damping the fluctuations in pressure and accumulating energy and fluid. The presence of a water accumulator directly influences cutting quality. In fact, at high pressures like those used in a water jet machine, water is compressible and the supply of water coming from the intensifier is discontinuous (the first part of the piston stroke compress the water instead of inject it in the high-pressure circuit). The oil circuit, too, presents pressure fluctuations which, despite being damped by the oil accumulator, are reflected in the intensifier moving less fluidly, thus causing water pressure fluctuations. All those effects sum up and lead to a discontinuous cutting action which is clearly detrimental for the quality of the cut, making necessary the presence of a water accumulator.

2.2.3 The cutting head

The cutting head is the part of the machine in which the transformation of pressure energy into kinetic energy, the jet focusing and the mixing of water and abrasive in case of abrasive water jet occur. Each part composing the head (orifice, mixing chamber and focuser tube) must be coaxial in order to obtain the best possible result in terms of jet shape and, thus, cutting quality.

The orifice jewel

The orifice jewel, or simply orifice, is the part that converts the pressure energy of water into kinetic energy. It is made by synthetic or natural diamond, ruby or sapphire due to their high resistance to heat, wear, corrosion and pressure. **Figure 2.7** shows a ruby orifice.

Figure 2.7: A ruby orifice [25]

It is possible to explain how the energy transformation works thanks to Bernoulli's principle (**Equations 2.3 and 2.4**). In the following discussion, the hypothesis of perfect fluid, meaning that the fluid is incompressible and with a coefficient of viscosity equal to zero, and the hypothesis of no losses of energy during the transformation are considered. It can be said:

$$\frac{p_0}{\gamma} + \frac{V_0^2}{2g} + z_0 = \frac{p_1}{\gamma} + \frac{V_1^2}{2g} + z_1 \tag{2.3}$$

$$\frac{(p_0 - p_1)}{\gamma} + \frac{(V_0^2 - V_1^2)}{2g} + (z_0 - z_1) = 0 \tag{2.4}$$

The subscript 0 identifies the section before the orifice, the subscript 1 the section after the orifice, g is the gravitational acceleration, γ is the specific weight of water, p is the relative pressure, meaning that the contribute of atmospheric pressure has been subtracted, and for this reason p_1, which is the pressure of the water after the orifice, is equal to zero as it is the atmospheric pressure. $z_0 - z_1$ is a value close to 0 and much smaller compared to the other two terms, thus it can be neglected. V_0 is the speed of the water before the orifice, usually 2-3 $\frac{m}{s}$, and can be neglected because it is much smaller in

comparison with V_1 (the speed of the water after the orifice) which is usually above 800 $\frac{m}{s}$.
After these simplifications and solving for V_1, the equation is:

$$V_1 = \sqrt{\frac{2\,p_0}{\rho}} \tag{2.5}$$

where ρ is the density of water.
However, water compressibility must be taken into account because the high pressures involved in the process. The model which considers water compressibility is shown in **Equation 2.6**, and the speed of the water after the orifice is calculated in **Equation 2.7** [26]:

$$\frac{\rho}{\rho_0} = \left(1 + \frac{P}{L}\right)^C \tag{2.6}$$

$$V_1 = \sqrt{\frac{2\,L}{\rho_0(1-C)}\left[\left(1 + \frac{P}{L}\right)^{1-C} - 1\right]} \tag{2.7}$$

where C = 0,1368 and L = 300 MPa are two constants.
Equation 2.7 shows the value of the theoretical speed of the water out of the orifice when no energy losses occur and water is considered compressible.

The mixing chamber
In case of injection abrasive water jets, grit and water are merged in the cutting head inside the mixing chamber. The abrasive flows from the hopper, a container attached to the cutting head which stores the sand, to the cutting head through a plastic tube. There are various solutions proposed by cutting heads producers in attempt to make the mixing process as uniform as possible in order to achieve a higher cutting quality. So, abrasive can enter mixing chamber from one up to four different holes, usually placed at equal distances one from the other, and the conveying tubes can be perpendicular or slightly tilted. **Figure 2.8** shows the different shapes of the mixing chambers:

Figure 2.8: Commercial mixing chambers produced by a) Accustream, b) Accustream, c) PTV

The abrasive grit enters the mixing chamber thanks to gravity and Venturi effect. Venturi effect is the reduction in pressure generated by a high speed fluid; in this case, the high speed water jet create a depression inside the mixing chamber, easing the flow of the abrasive from the hopper to the mixing chamber. Inside the mixing chamber, a depression caused by the high speed jet which creates a suction effect helping the flow of abrasive.
Water starts to transfer momentum to abrasive particles as they are absorbed into the jet before reaching the last part of the cutting head: the focusing tube.

The focusing tube
The last part of the machine right before the workpiece is the focusing tube (**Figure 2.9**). In it, the jet is made coherent and with the desired diameter, while water completes the transferring of momentum to the abrasive.
The top of the focusing tube presents a conical entrance to help the channeling of the jet.

Figure 2.9: Focusing tube

The focuser is subject to severe wear due to erosion and abrasion caused by abrasive particles as shown in **Figure 2.10**. Erosion occurs at the beginning of the tube, where impingement angles are high. Toward the end of the focuser, where the jet is almost aligned with the axis of the focuser and impact angle tends to zero, the material removal is caused by abrasion.

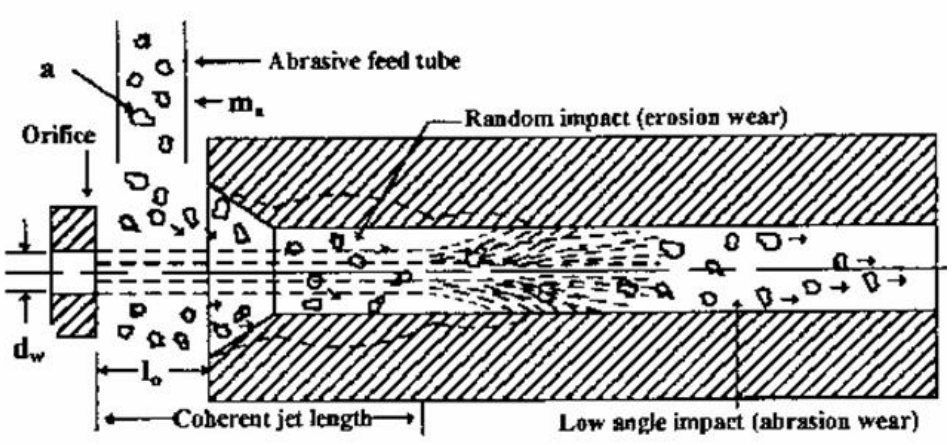

Figure 2.10: The wear process of a focuser

In order to resist to such a high wear, focusers are usually made by materials with high hardness as sintered tungsten and boron carbides.

2.2.4 The abrasive feeder

Attached to the moving part of the machine above the cutting head there is the abrasive feeder, also called hopper, which is a container filled with the sand used during the cut. A plastic tube goes from the feeder to the mixing chamber allowing the flow of abrasive from the hopper to the cutting head. The abrasive flow can be regulated rotating a marked indicator.

Figure 2.11: Abrasive feeder produced by Accustream

2.2.5 The catcher

Right below the workpiece, there is a big water tank called catcher with the functions of collecting the jet, dissipating its remaining energy (usually around 75% of the starting energy), damping the noise caused by the machine, avoiding dangerous jet back-reflections which can damage the machine or hurt people and collect scraps and abrasive particles for recycling or disposal.
A metal grid is usually placed above the catcher in order to support the workpiece.

2.3 The abrasive

In AWJ, abrasive sand is added to the jet. Abrasive should not be hygroscopic and should have a low dust content for safety matters and for avoiding clogging in the mixing chambers. The abrasive is sold in bags and the average dimension of the grit is indicated using the mesh size, commonly #80 or #120, which correspond to an average particle diameter of 180 and 125 microns. Thanks to its low cost and good cutting performance, garnet is the most used abrasive. Harder and sharper abrasives such as alumina or silicon carbide can be used when an higher cutting power is needed, allowing the machining of thicker or harder materials. However, the better cutting performances are also reflected in a faster wear of the focuser. **Figure 2.12** shows some of the most common abrasives employed in abrasive water jetting.

Figure 2.12: garnet (left), white alumina (middle), olivine (right)

2.4 Water jet applications

The great flexibility, scalability and the peculiar characteristic of water jet technology makes it suitable for a great number of applications [27].

Cutting of 2D and 3D shapes
The main application of water jet. A pure water jet is capable of cutting leather, food, wood and other soft materials; abrasive water jet is needed for harder materials such as metals, ceramics and stones. Composite materials can be easily cut with WJ because the different properties of the matrix and the fibers do not affect the process. The maximum thickness which can be cut depends only on the maximum pressure provided by the pump, but it is generally around 300 mm.
Water jet is commonly used for cutting 2D shapes out of a plate, but thanks to 5-axis machines it is also possible to cut 3D shapes. The complexity of the shape is limited by the jet diameter. For this reason, micro abrasive water jet technology has been developed. It is capable of machining features in the range of 200 – 300 µm [28].

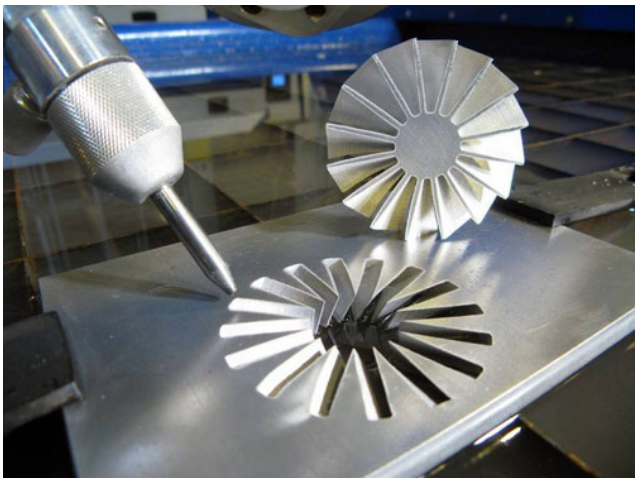

Figure 2.13: A 3D shape cut with WJ technology [29]

Drilling
It is possible to make holes as small as the jet diameter and, thanks to 5-axis machines, holes can have an angle different from 90 degrees.

Turning and milling
These two applications, in particular turning, are still in a development phase but tests showed water jet capability of turning axis-symmetric parts (for example grinding wheels [30]) and milling surfaces. In WJ turning (**Figure 2.14**), the workpiece rotates while the abrasive water jet is traversed axially and

radially to produce the required turned surface. This technique may facilitate production of rotational-symmetries in hard to cut materials.

Figure 2.14: Water jet turning

WJ milling works in control of depth, meaning that process parameters are chosen in order to keep the depth of penetration to a fixed value. A mask made by a material harder than the target one can be used to obtain better results when cutting thin walls or corners [31]

Figure 2.15: A shape obtained by water jet milling [32]

Forming
The jet is used to generate permanent deformations on the workpieces [33]

Dismantling and decommissioning
Thanks to the low temperatures during the cut and the capability of machining big parts, water jet can be used for the decommissioning of nuclear facilities [34] and dismantlement of weapons

Surface treatments
Water jet can be used in processes that modify the surface like cleaning [35], rust removal, peening [36], stripping, polishing [8] or texturing.

2.5 Water jet Advantages

The Water jet machining rise in popularity is completely justified by a series of advantages which, together with simplicity and flexibility, make this technology suitable for a wide range of applications. The general advantages of WJ machining are listed below [22]:

- Cutting virtually any materials: the target material does not need to have specific properties in order to be machined. The only property of interest is its hardness when choosing between PWJ and AWJ.

- Machining thick materials: despite the majority of parts are less than 25 mm thick, WJ is capable of cutting through thickness up to 300 mm of steel.

- Cold cut: the little heat WJ machining generates (the maximum workpiece temperature is around 50 °C during piercing) is removed by water, thus avoiding the formation of a heat affected zone (HAZ) which would cause alterations in chemical and physical properties of the material. For this reason, it is possible to machine parts that have already been heat treated.

- Low cutting force: WJ cutting forces are really low (some newtons). This results in no residual stresses. Moreover, brittle materials and thin features like walls 0.25 mm thick can be easily machined.

- Almost burr free: by correctly setting up the process it is possible to avoid the formation of burrs which would require further machining operations.

- No extra coolant needed: it is not necessary to buy any coolant since the water needed for cutting also removes heat from the cutting area.

- Simple fixturing: forces developed by WJ machining are mostly vertical, with small forces in the horizontal direction. For this reason, the fixturing generally consists in fixing the workpiece to the metal grid above the catcher with clamps or weights.

- A few material removed: WJ cuts are around 1 mm wide resulting in a limited production of scraps, meaning it is possible to save money since less material is needed. Moreover, if the material is hazardous, the costs related to the disposal will be less compared to the costs of other machining technologies.

- Environmentally friendly: as long as the machined material is not hazardous, the spent abrasive and waste material become suitable for landfill. The most commonly used abrasive, garnet, is an inert mineral and can be disposed of with other trash. Excess water is simply drained to the sewer. When hazardous materials are machined, water must be recycled and scraps must be disposed of appropriately. However, very little metal is actually removed in the cutting process, keeping the environmental impact relatively low.
  Probably, the biggest environmental impact of WJ machining is caused by the pumps as they require a considerable amount of electricity.

To fully understand the potentiality of WJ machining, it is necessary to compare it to its direct competitors: laser machining and electrical discharge machining (EDM).

2.5.1 Advantages of water jet machining compared to laser machining

Nowadays, laser technology is the best choice for a fast and precise cutting of materials compatible with the laser radiation when the parts are thin and high volumes of production are involved. Anyway, WJ technology presents some advantages compared to laser technology [22]:

- Machining a wider range of materials: WJ can machine reflective materials such as copper and aluminum and heat-sensitive materials which laser machining cannot cut.

- No heat affected zone: WJ does not heat the workpieces and does not change their properties. There are also no thermal distortions, which can occur with certain types of laser.

- Thicker parts: laser can cut through a limited thickness, usually around 5 mm. WJ can cut successfully parts up to 300 mm thick by lowering feed speed and increasing pressure.

- Homogeneity of material is not important: multilayer and composite material cannot be machined using a laser beam because of the different response to laser radiation of each material. WJ is not affected by a change in composition.

- Planarity is not fundamental: in laser application, the material has to be as uniform as possible since a change in surface planarity leads to a loss of focus and therefore cutting power. On the other hand, such changes have negligible effect on the efficiency of a WJ cut.

- No burrs and better edge finish: most types of the laser cutting causes the melting of the material which is difficult to remove completely, resulting in burrs on the lower side of the kerf and a rougher, scaly edge. WJ, due to the abrasive nature of the process, does not have burrs and have a fine, sand-blasted surface.

- Lower capital equipment and maintenance costs: it is possible to buy some water jet centers for the same price of a laser machine. Moreover, maintenance is easier and cheaper on a water jet machine.

2.5.2 Advantages of water jet machining compared to EDM machining

In EDM, a series of electric arcs rapidly discharge between an electrode and the workpiece, causing the melting and vaporization of the material. A continuous flow of non-conductive coolant such as kerosene or deionized water flushes away the removed particles. While the process is extremely slow, it can create complex features that are hard to machine with other technologies and satisfy strict tolerances.
A list of advantages of WJ on EDM is presented below:

- Faster: WJ machining is faster than EDM.

- Machining a wider range of materials: EDM requires the target material to be electrically conductive. WJ does not have this limitation.

- Bigger parts: the only dimensional limit of parts made using WJ is the size of the x-y table. It is uncommon to machine big parts with EDM due to its low removal rate.

- Less set up: in general, EDM set up requires more attention, while in WJ the fixturing consists in weighing down the material without the need of being elaborate or precise.

- Makes its own piece hole: in some types of EDM, such as wire-EDM, a hole must be created by a different process. Water jet can pierce the material on its own, requiring no additional machining.

Chapter 3

Properties and Applications of Piezoelectric Ceramics

Advanced ceramics are widely used thanks to their high hardness, wear resistance, thermal resistance and chemical inertness. The following chapter will introduce the piezoelectric effect, will give an overview of piezoceramics and will describe PZT, the material used in the experimentation. The material removal mechanisms of ceramics will be also discussed.

3.1 Piezoelectric materials

In 1880 Jacques and Pierre Curie discovered the piezoelectric effect which links the electrical and mechanical behavior in piezoelectric materials. The electric charge displacement caused by a mechanical stress is called direct piezoelectric effect [37]. Vice versa, the arise of mechanical stress in a material in response to an electrical voltage is the converse piezoelectric effect [37]. The effect is caused by an asymmetry in the distribution of the electrical charge in the crystal that generates an electric dipole moment when a strain is applied. **Figure 3.1** shows the two piezoelectric effects.

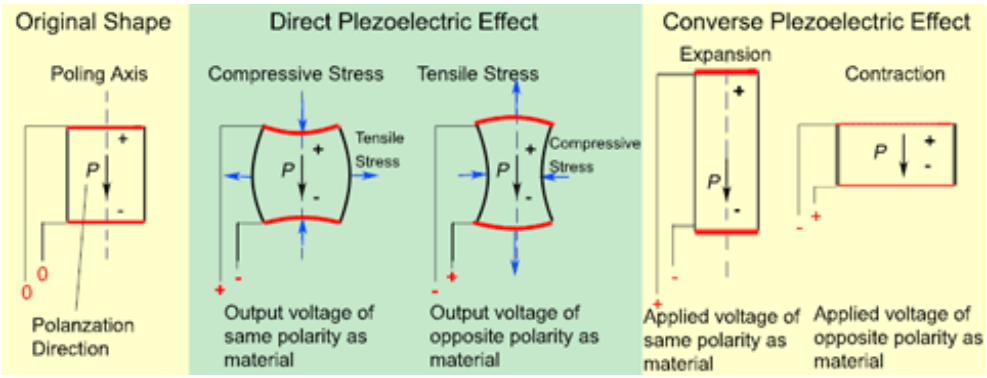

Figure 3.1: Direct and converse piezoelectric effect [38]

Some naturally piezoelectric materials such as quartz, tourmaline or Rochelle salt can be found but nowadays most of the materials employed are made artificially as, for example, piezoeceramic (e.g. PZT), piezocomposites and piezopolymers (e.g. polyvinylidene fluoride also called PVDF).

3.2 Theory of piezoelectricity

Monographs like [37] discuss the various mathematical aspects of the theory of piezoelectricity. The simplest formulation of the theory of piezoelectricity is the linear theory which applies when small electrical and mechanical amplitudes are involved. In this condition, the relationships between the mechanical strain or stress components and the electric field or the dielectric displacement components are linear and the relations are coupled. The relations describing the coupling between mechanical stress *T*, mechanical strain *S*, electric field *E* and electric displacement *D* are the following:

$$S_p = s_{pq}^E T_q + d_{pk} E_k \tag{3.1}$$

$$D_i = d_{iq} T_q + \varepsilon_{ik}^T E_k \tag{3.2}$$

where s_{pq}^E is the elastic compliance constant at constant electric field, ε_{ik}^T is the dielectric constant under constant stress, d_{pk} is the piezoelectric constant, S_p is the mechanical strain in p direction, D_i is the electric displacement in i direction, T_q is the mechanical stress in q direction and E_k is the electric field in k direction. The matrix form of Eq. 3.1 and Eq. 3.2 is the following [39]:

$$\begin{bmatrix} S_1 \\ S_2 \\ S_3 \\ S_4 \\ S_5 \\ S_6 \end{bmatrix} = \begin{bmatrix} s_{11}^E & s_{12}^E & s_{13}^E & s_{14}^E & s_{15}^E & s_{16}^E \\ s_{21}^E & s_{22}^E & s_{23}^E & s_{24}^E & s_{25}^E & s_{26}^E \\ s_{31}^E & s_{32}^E & s_{33}^E & s_{34}^E & s_{35}^E & s_{36}^E \\ s_{41}^E & s_{42}^E & s_{43}^E & s_{44}^E & s_{45}^E & s_{46}^E \\ s_{51}^E & s_{52}^E & s_{53}^E & s_{54}^E & s_{55}^E & s_{56}^E \\ s_{61}^E & s_{62}^E & s_{63}^E & s_{64}^E & s_{65}^E & s_{66}^E \end{bmatrix} \begin{bmatrix} T_1 \\ T_2 \\ T_3 \\ T_4 \\ T_5 \\ T_6 \end{bmatrix} + \begin{bmatrix} d_{11} & d_{12} & d_{13} \\ d_{21} & d_{22} & d_{23} \\ d_{31} & d_{32} & d_{33} \\ d_{41} & d_{42} & d_{43} \\ d_{51} & d_{52} & d_{53} \\ d_{61} & d_{62} & d_{63} \end{bmatrix} \begin{bmatrix} E_1 \\ E_2 \\ E_3 \end{bmatrix} \tag{3.3}$$

$$\begin{bmatrix} D_1 \\ D_2 \\ D_3 \end{bmatrix} = \begin{bmatrix} d_{11} & d_{12} & d_{13} & d_{14} & d_{15} & d_{16} \\ d_{21} & d_{22} & d_{23} & d_{24} & d_{25} & d_{26} \\ d_{31} & d_{32} & d_{33} & d_{34} & d_{35} & d_{36} \end{bmatrix} \begin{bmatrix} T_1 \\ T_2 \\ T_3 \\ T_4 \\ T_5 \\ T_6 \end{bmatrix} + \begin{bmatrix} \varepsilon_{11}^T & \varepsilon_{12}^T & \varepsilon_{13}^T \\ \varepsilon_{21}^T & \varepsilon_{22}^T & \varepsilon_{23}^T \\ \varepsilon_{31}^T & \varepsilon_{32}^T & \varepsilon_{33}^T \end{bmatrix} \begin{bmatrix} E_1 \\ E_2 \\ E_3 \end{bmatrix} \tag{3.4}$$

and the compact form is:

$$\{S\} = [s]\{T\} + [d]^T\{E\} \tag{3.5}$$

$$\{D\} = [d]\{T\} + [\varepsilon]\{E\} \tag{3.6}$$

The first equation represents the converse dielectric effect, the second the direct piezoelectric effect. The axis directions used in **Equation 3.3** and **Equation 3.4** are shown in **Figure 3.2**:

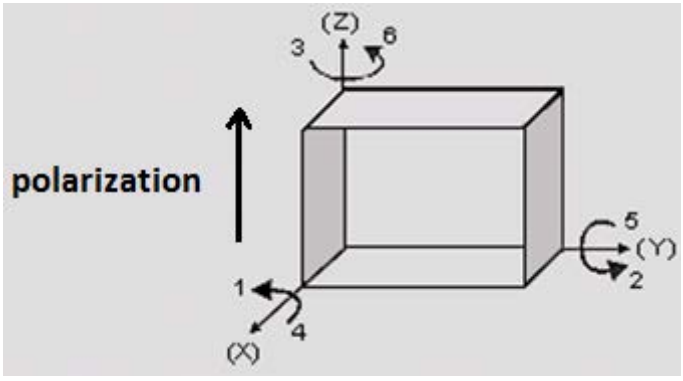

Figure 3.2: Tensor directions for defining the constitutive relations [40]

The reference axis 3 is parallel to the direction of polarization, while axis 1 and 2 are defined arbitrarily in order to form a cartesian system with axis 3. 4, 5 and 6 represent the shear movements around axes 1, 2 and 3. In many cases the presence of crystal symmetries reduces the complexity of the dielectric constant, elastic compliance and piezoelectric tensors as some of the components of the tensors are equal to zero. **Equation 3.3** and **Equation 3.4** can be rewritten as following after simplifying [39]:

$$\begin{bmatrix} S_1 \\ S_2 \\ S_3 \\ S_4 \\ S_5 \\ S_6 \end{bmatrix} = \begin{bmatrix} s_{11}^E & s_{12}^E & s_{13}^E & 0 & 0 & 0 \\ s_{21}^E & s_{22}^E & s_{23}^E & 0 & 0 & 0 \\ s_{31}^E & s_{32}^E & s_{33}^E & 0 & 0 & 0 \\ 0 & 0 & 0 & s_{44}^E & 0 & 0 \\ 0 & 0 & 0 & 0 & s_{55}^E & 0 \\ 0 & 0 & 0 & 0 & 0 & s_{66}^E \end{bmatrix} \begin{bmatrix} T_1 \\ T_2 \\ T_3 \\ T_4 \\ T_5 \\ T_6 \end{bmatrix} + \begin{bmatrix} 0 & 0 & d_{31} \\ 0 & 0 & d_{32} \\ 0 & 0 & d_{33} \\ 0 & d_{24} & 0 \\ d_{15} & 0 & 0 \\ 0 & 0 & 0 \end{bmatrix} \begin{bmatrix} E_1 \\ E_2 \\ E_3 \end{bmatrix} \tag{3.7}$$

$$\begin{bmatrix} D_1 \\ D_2 \\ D_3 \end{bmatrix} = \begin{bmatrix} 0 & 0 & 0 & 0 & d_{15} & 0 \\ 0 & 0 & 0 & d_{24} & 0 & 0 \\ d_{31} & d_{32} & d_{33} & 0 & 0 & 0 \end{bmatrix} \begin{bmatrix} T_1 \\ T_2 \\ T_3 \\ T_4 \\ T_5 \\ T_6 \end{bmatrix} + \begin{bmatrix} \varepsilon_{11}^T & 0 & 0 \\ 0 & \varepsilon_{22}^T & 0 \\ 0 & 0 & \varepsilon_{33}^T \end{bmatrix} \begin{bmatrix} E_1 \\ E_2 \\ E_3 \end{bmatrix} \quad (3.8)$$

3.3 Polycrystalline piezoceramics

The material used in this work is a polycrystalline piezoceramic called lead zirconate titanate or PZT. Piezoelectric ceramics as PZT belong to the group of ferroelectric materials, a subgroup of piezoelectric materials in which the material crystal is polar without the application of an electric field. In general, a polycrystalline piezoceramic is a mass of perovskite ceramic crystals each consisting of a small, tetravalent metal ion, usually titanium or zirconium, in a lattice of larger, divalent metal ions, usually lead or barium, and O_2 ions. Above a critical temperature, the Curie point (T_c), each perovskite crystal in the ceramic lattice exhibits a simple cubic symmetry with no dipole moment (**Figure 3.3a**). At temperatures below the Curie point, however, each crystal has tetragonal or rhombohedral symmetry and a dipole moment (**Figure 3.3b**).

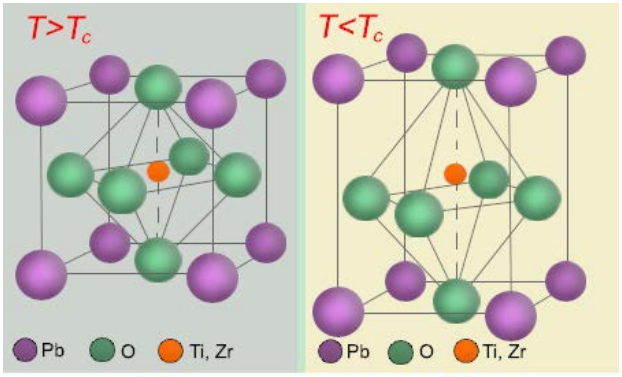

Figure 3.3: Crystal structure of a piezoelectric ceramic [38]

The direction of polarization among neighboring domains is random so the ceramic element has no overall polarization. The initial orientation is shown in **Figure 3.4a**. The domains in a piezoceramic element are aligned artificially in order to generate a net polarization by exposing the material to a strong, direct current electric field, while keeping it at a temperature slightly below the Curie point (**Figure 3.4b**). This process is called polarizing (poling) treatment. When

the electric field is removed, most of the dipoles are locked into a configuration of near alignment (**Figure 3.4c**) in the direction of the electric field previously applied and the material now has a permanent polarization.

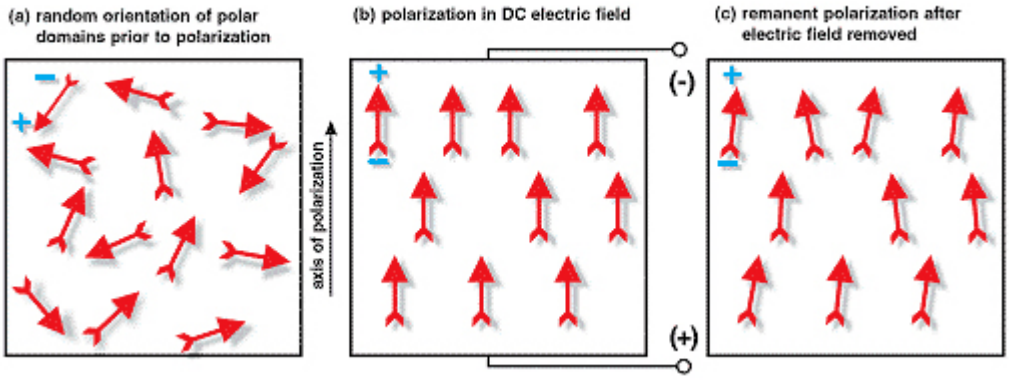

Figure 3.4: Poling process [41]

However, the poled polycrystalline ceramics present some drawbacks as they could lose the piezoelectric properties if heated above its critical temperature, exposed to electric fields opposite to the one used in the poling treatment or if the stress in the material is too high. Moreover, the piezoelectric properties are subject to time decay (ageing).

A poled ferroelectric material exhibits hysteresis. A typical hysteresis curve is the P-E loop (**Figure 3.5**). It shows the polarization reversal (or switching), an important characteristic of the ferroelectric materials. When removing the polarizing field, a residual polarization remains in the material. However, the material loses its polarization if the applied electric field reaches the value of the coercive field $-E_c$. A further increase of the field in the negative direction will cause a repolarization in the direction opposite to the initial one. An ideal hysteresis loop is symmetrical, so the positive and negative coercive fields and positive and negative remaining polarization are equal. The coercive field, spontaneous and remaining polarization and shape of the loop are affected by many factors including the thickness of the sample, the presence of defects, mechanical stresses, thermal treatment and preparation conditions.

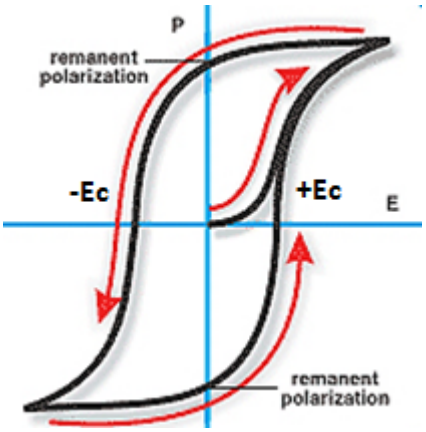

Figure 3.5: P-E loop [41]

Another characteristic hysteresis loop is the so called butterfly loop (**Figure 3.6**).

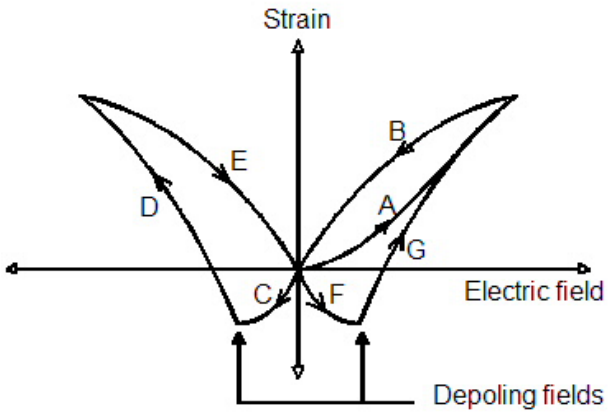

Figure 3.6: Butterfly loop

It shows the relation between electric field and strain. The relation is linear until the coercive (depoling) field is reached. At this point, the strain starts to grow, switching its initial behavior. The butterfly diagram provides a complete characterization of the depoling and repoling process [42].

3.3.1 Lead zirconate titanate (PZT)

One of the most employed piezoelectric ceramic is the lead zirconate titanate or PZT. It is a metallic oxide-based piezoelectric polycrystalline ceramic developed by scientists at the Tokyio Institute of Technology in 1952. PZT is widely used thanks to the low production costs and the simplicity of the manufacturing process, the relatively high Curie temperature, the high efficiency in the electro-mechanical transformation and the vast range of applications. Its

chemical formulation is $Pb[Zr_xTi_{1-x}]O_3$ and it is formed by perovskite crystals consisting of a tetravalent metal ion (titanium or zirconium) in a lattice of large divalent metal ions (lead) and O_2 ions as shown in **Figure 3.7**.

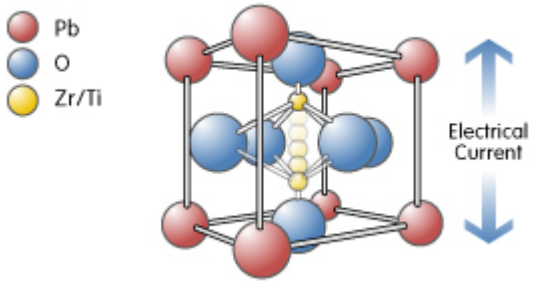

Figure 3.7: PZT crystal **[43]**

The manufacturing process of PZT is the following:

1) Materials selection: high purity raw materials are selected and weighed according to the formulation
2) Wet milling: the powder are wet-milled together to achieve an uniform particle size distribution.
3) Calcination: the product is dried and then calcinated in air at a temperature of 1000 °C using high-purity crucibles in order to avoid the presence of chemical contaminants in the final product. The desired PZT phase is formed in this step.
4) Milling: the powder is returned to the mill to ensure homogeneity. An organic binding agent is added.
5) Spray drying: the purpose of the spray drying is to remove water and provide a product in the form of binder-containing hollow spheres with a narrow particle size distribution.
6) Pressing: the powders are compacted using presses capable of applying forces up to 1 MN.
7) Sintering: the material is sintered at temperatures around 1300 °C to achieve the final material structure.
8) Shaping: the material is lapped, grinded and cut in order to achieve the desired shape.
9) Electrode application: metal electrodes are used to collect the electric signal or to transmit a voltage to the piece. They can be applied with numerous technics, for example by sputtering or screen printing, and are generally made by noble metals as Au or Ag or by metal alloys such as CuNi.
10) Polarization: the material is poled as explained in **Section 3.3**.

PZT classification

PZT is divided in two categories: hard and soft. The classification refers to the mobility of the dipoles and hence also to the polarization and depolarization behavior; in fact, the higher is the domain mobility, the easier the material can be polarized or depolarized. Soft PZT is characterized by a high mobility domain and for this reason it is relatively easy to polarize. Soft PZT has a high relative permittivity, large electromechanical coupling factors, large piezoelectric constants, low mechanical quality factors and, in general, a lower Curie point. On the other hand, the advantages of hard PZT are the low dielectric and mechanical losses, high piezoelectric charge constants, very good stability under high mechanical loads and operating electric fields and a higher Curie point compared to soft PZT. **Figure 3.8** illustrates the different PZT typologies produced by PICeramic. It shows how the soft PZT relative permittivity is higher than the hard PZT permittivity both in the direction parallel and perpendicular to the polarization direction, meaning that soft PZT is easier to polarize. The dielectric loss factor, which indicates how many electromagnetic energy is dissipated, is lower for hard PZT. The piezoelectric coupling factors in the various directions are higher for soft PZT.

				Soft PZT					Hard PZT			
Piezo Material type				PIC 151	PIC 255	PIC 155	PIC 153	PIC 152	PIC 181	PIC 141	PIC 241	PIC 300
Parameter												
Physical and Dielectric Properties												
Density		ρ (g/cm^3)		7,80	7,80	7,80	7,60	7,70	7,80	7,80	7,80	7,80
Curie Temperature		Tc (°C)		250	350	345	185	340	330	295	270	370
Permittivity	in the polarization direction	$\varepsilon_{33}^T/\varepsilon_0$		2400	1750	1450	4200	1350	1200	1250	1650	1050
	perpendicular to the polarity	$\varepsilon_{11}^T/\varepsilon_0$		1980	1650	1400			1500	1500	1550	950
Dielectric loss factor		tan δ (10^{-3})		20	20	20	30	15	3	5	5	3
Electromechanical Properties												
Coupling factors		k_p		0,62	0,62	0,62	0,62	0,48	0,56	0,55	0,50	0,48
		k_t		0,53	0,47	0,48			0,46	0,48	0,46	0,43
		k_{31}		0,38	0,35	0,35			0,32	0,31	0,32	0,25
		k_{33}		0,69	0,69	0,69		0,58	0,66	0,66	0,64	0,46
		k_{15}			0,66				0,63	0,67	0,63	0,32
Piezoelectric charge constants		d_{31}	(10^{-12} C/N)	-210	-180	-165			-120	-140	-130	-80
		d_{33}		500	400	360	600	300	265	310	290	155
		d_{15}			550				475	475	265	155
Piezoelectric voltage constants		g_{31}	(10^{-3} Vm/N)	-11,5	-11,3	-12,9			-11,2	-13,1	-9,8	-9,5
		g_{33}		22	25	27	16	25	25	29	21	16
Acousto-mechanical properties												
Frequency constants		N_p	(Hzm)	1950	2000	1960	1960	2250	2270	2250	2190	2350
		N_1		1500	1420	1500			1640	1610	1590	1700
		N_3		1750		1780			2010	1925	1550	1700
		N_t		1950	2000	1990	1960	1920	2110	2060	2140	2100
Elastic constants (compliance)		S_{11}^E	(10^{-12} m^2/N)	15,0	16,1	15,6			11,8	12,4	12,6	11,1
		S_{33}^E		19,0	20,7	19,7			14,2	13,0	14,3	11,8
Elastic constants (stiffness)		C_{33}^D	(10^{10} N/m^2)	10,0		11,1			16,6	15,8	13,8	16,4
Mechanical quality factor		Qm		100	80	80	50	100	2000	1500	1200	1400
Temperature stability												
Temperature coefficient of ε^T_{33} (in the range -20°C up to +125°C)		TK ε_{33} (x10^{-3} /K)		6	4	6	5	2	3	5		2
Aging stability (relative change of the parameter per decade in %)												
Relative dielectric constant		C_ε	(%)		-1,0	-2,0				-4,0		
Coupling factor		C_K			-1,0	-2,0				-2,0		

Figure 3.8: PICeramic PZT coefficients table [44]

3.4 Piezoelectric ceramics applications

Nowadays, piezoceramics are widely used in industry. They are employed as electric generators, actuators, sensors and transducers.

3.4.1 Piezoelectric generators

A mechanical stress is converted to electricity using the direct piezoelectric effect. As power requirements for microelectronic decrease, a piezoelectric generator could be a feasible alternative to a battery. Generators can be single-layer or multilayer (obtained by stacking various single layer actuators alternated with electrodes). Multilayer generators produce a lower voltage compared to the voltage generated by single layer generators but the current produced is higher. Common applications of piezo generators are ignition systems in cigarette lighters (**Figure 3.9**) and coocking grills or energy sources for wireless sensors or munitions.

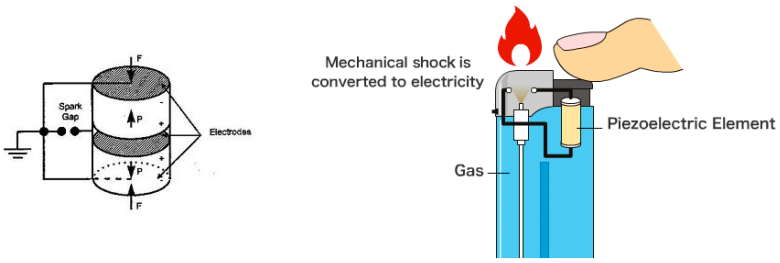

Figure 3.9: Piezo generator in a cigarette lighter

3.4.2 Piezoelectric actuators

Piezoelectric actuators (**Figure 3.10**) use the inverse piezoelectric effect to transform a voltage into a change in length. They are characterized by high mechanical load capacities, low power and energy losses, short responses times, high motion resolutions and high reliability. The field of application of piezoelectric actuators are numerous. For example, they are employed in optics, aerospace, medical and instrumentation fields, principally as micropositioning or nanopositioning systems.

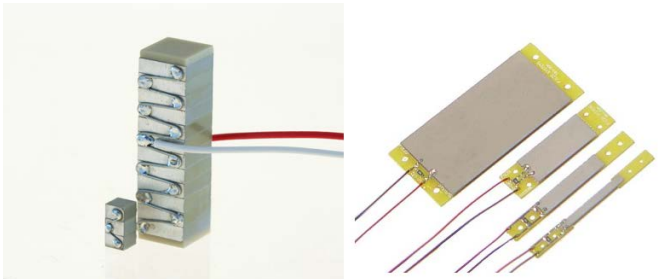

Figure 3.10: Piezoactuators [42] [45]

3.4.3 Piezoelectric sensors and transducers

Piezo sensors (**Figure 3.11**) are used to convert mechanical actions, such as forces, accelerations or pressures, into electric signals, while as transducers they receive and transmit waves. They offer reliability and compactness, low energy consumption, high temperature ranges, time stability and a wide linear range. Piezoelectric ceramics are commonly used as accelerometers, force sensors, shock sensors, strain and deformation sensors, microphones or ultrasonic transducers.

Figure 3.11: A piezoelectric sensor [46]

3.5 Material removal mechanisms in ceramics

The erosion of materials as the result of the impact of abrasive particles is the basic removal mechanism in abrasive water jet and it has generally been viewed as a brittle process in which the material is removed mainly as a result of crack formation. As shown in **Figure 3.12**, when a blunt particle comes into contact with a brittle material, lateral, conical and radial cracks form. The lateral ones are responsible for removing most of the material. [47]

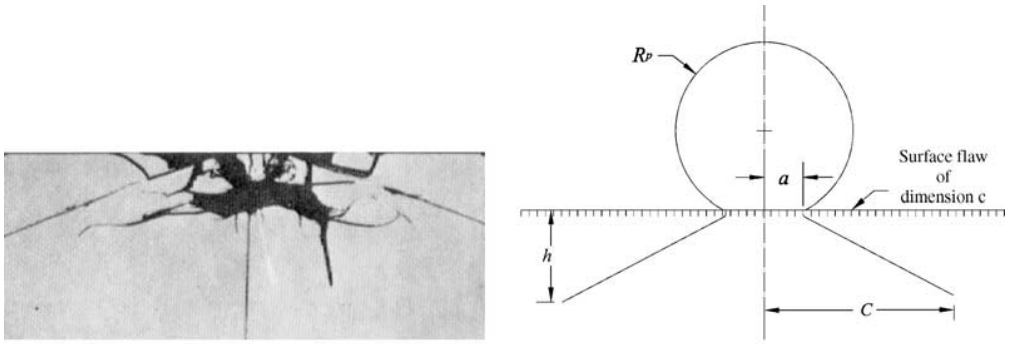

Figure 3.12: Cracking in brittle materials [47]

According to [48], the conical and radial cracks are formed during the loading period of the particle/target interation while the lateral cracks are formed during the unloading period. A study [49] revealed that the most pronounced impact damage mechanism in polycrystalline ceramics is intergranular cracking. While transgranular cracking occurs in some individual grains, intergranular cracking is dominant. Plastic flow occur at the impact site leading to microcutting. The two mechanisms are illustrated in **Figure 3.13**. At low impact angles, scratching on the kerf surface can be observed.

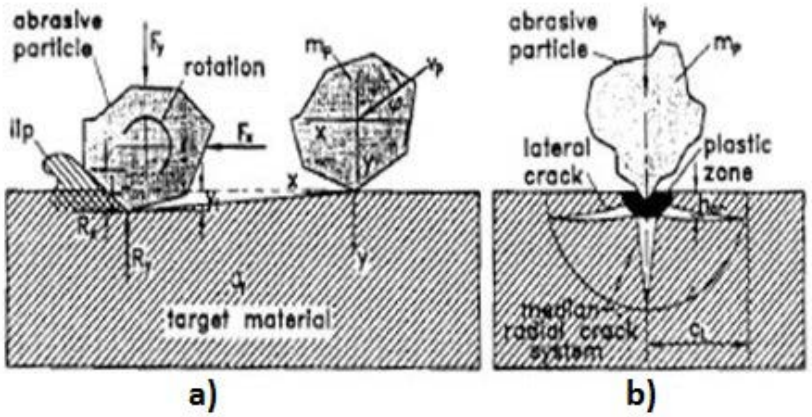

Figure 3.13: Material removal mechanisms by solid particle impact
a) microcutting b) cracking [27]

Chapter 4

Methodology

The aims of this work are to investigate the surface finish of PZT sheets machined by abrasive water jet and to analyze the electrical signal acquired from the specimen during the cuts in order to obtain information on the cutting process. To ensure a repeatability and verification of results, a detailed explanation of the procedures used in this experimental campaign is now presented.

4.1 Sieving

The abrasive size has a direct influence on the resulting surface texture. The parameter used to indicate the dimension of particles in commercial abrasives is the mesh size, in respect to the process of sieving which is used to select the abrasive particles. The mesh number is defined as the number of openings in a linear inch and, as the value increases, the holes in the sieve become less and less large. The most common values of abrasive mesh size used in WJ are 80 and 120, which correspond to an average particle diameter of 180 and 125 microns. The use of the word average must be noted: in fact, the sieving process is not deterministic, as a particle bigger than the opening can pass through due to irregularity of its shape. This results in a statistical distribution of the abrasive diameters which is usually known and provided by the abrasive seller. **Figure 4.1** shows the different distributions per abrasive mesh size (HPX is the commercial name of the sand, the number indicate the mesh size) of Barton garnet [50].

Grade		50 HPX	65 HPX	80 HPX	85 HPX	120 HPX	150 HPX	220 HPX	230 HPX
Recommended Nozzle Size		.040"	.040"	.040"	.030"	.030"	.020"	.020"	.015"
Minimum Nozzle Size		.040"	.040"	.030"	.030"	.020"	.015"	.015"	.015"
Screen Size Tyler / US	Opening Micron / Inch	Percent by Weight							
28 / 30	600 / .0234	<1							
32 / 35	500 / .0197	2	1						
35 / 40	425 / .0165	25	6						
42 / 45	355 / .0139	40	26	5	1				
48 / 50	300 / .0117	22	23	19	10				
60 / 60	250 / .0098	8	19	26	13				
65 / 70	212 / .0083	3	13	21	14	2			
80 / 80	180 / .0070		7	17	13	14			
100 / 100	150 / .0059		3	7	18	29	1		
115 / 120	125 / .0049		2	5	17	28	19	5	<1
150 / 140	106 / .0041				7	15	39	21	8
170 / 170	90 / .0035				4	7	24	28	31
200 / 200	75 / .0029				3	5	12	22	29
250 / 230	63 / .0025						4	15	18
270 / 270	53 / .0021						1	5	6
325 / 325	45 / .0017							4	8

Figure 4.1: Abrasive size distribution of Barton garnet [50]

In general, two bags of abrasive with the same nominal mesh size bought from different sellers are not equal in composition. Since in this work three different abrasives bought from different producers have been used and it has not been possible to find the information about the abrasive size distribution, the only way to have mesh sizes as similar as possible has been to sieve the three powders.

A set of sieves with stainless steel wire mesh and a brass frame has been used. Sieves have been stacked as in **Figure 4.2**, placing the one with the biggest opening on top and the one with the smallest opening at the bottom. The openings were 250, 212, 180 and 125 microns going from top to bottom. All the sieves are conform to the BS 410 standard with the exception of the sieve with the opening of 212 µm which is conform to ISO 3310-1. However, this is not an issue since the two standards are equivalent.

Figure 4.2: Sieves

The Endecotts Octagon Digital sieving machine (**Figure 4.4**) was used to ensure uniformity in the sieving process. Each load of abrasive consists of around 300 g of material (**Figure 4.3**).

Figure 4.3: A load of abrasive (SiC)

The machine was set to the maximum amplitude of vibration available and the duration of the sieving process was set to 10 minutes. The machine has a base with a seat for the sieves and an adjustable cover which keeps the sieves fixed to the machine in order to transmit the vibrations.

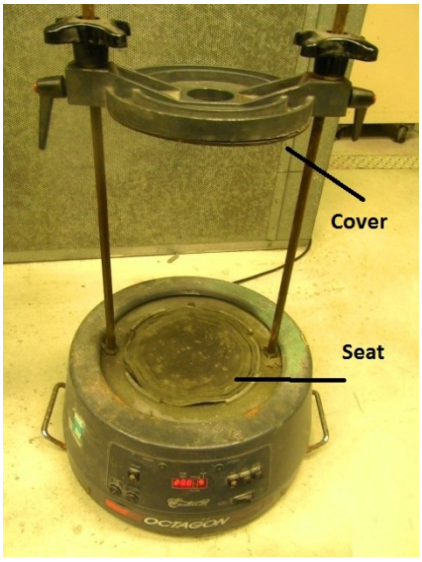

Figure 4.4: Endecotts Octagon Digital sieving machine

After loading the top sieve with the charge, a metal cover is used to close the sieves, which are then put in position in the machine seat. The machine cover is then tighten on the cover of the sieves as shown in **Figure 4.5**.

Figure 4.5: The sieving machine set up

When the sieving process is done, the sand laying in the 180 µm sieve is put in a plastic bag (**Figure 4.6**) while the grit from the other sieves is put in a different container. The sieves have been cleaned using compressed air every time a different abrasive was sieved.

Figure 4.6: The sieved abrasives (a) garnet, (b) white alumia, (c) silicon carbide

4.2 The supporting plate

A 800 x 300 mm plate made of titanium with a thickness of 5 mm was used as support for the PZT sheets (**Figure 4.7** and **Figure 4.8**). The sheet position on the supporting plate is shown in **Figure 4.14** in **Section 4.3**.

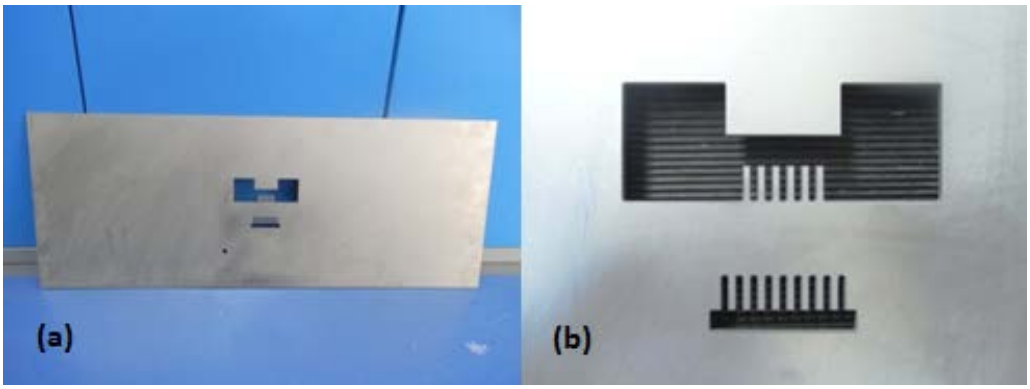

Figure 4.7: (a) supporting plate, (b) detail of the plate

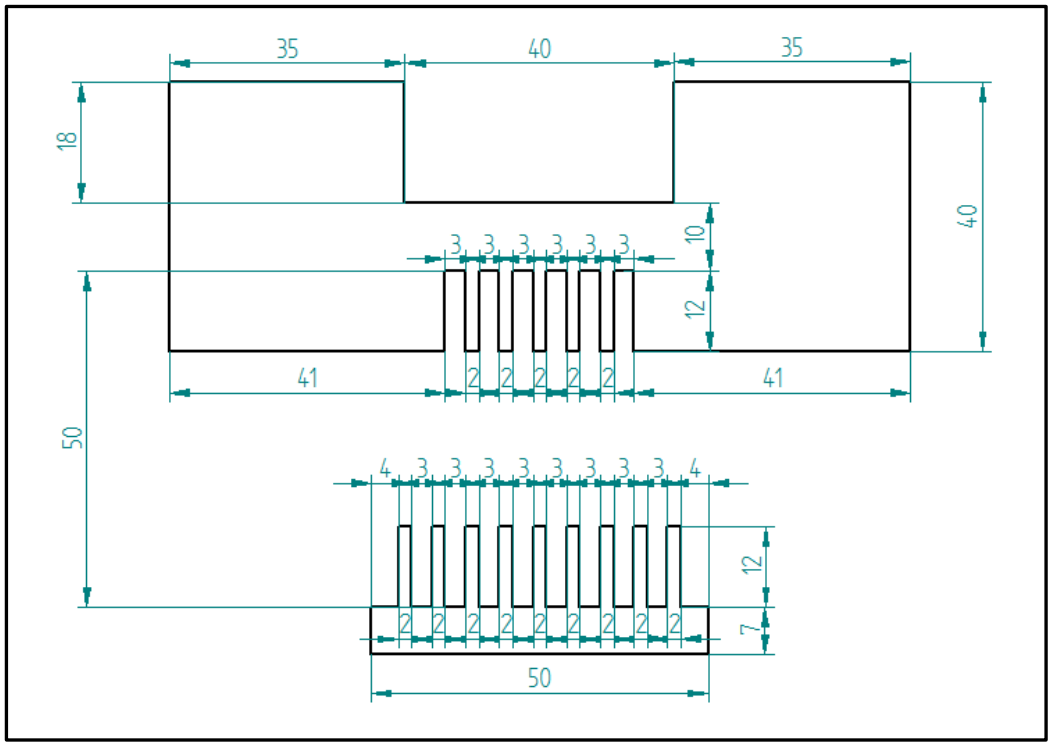

Figure 4.8: Drawing of the supporting plate

The plate has the function of supporting the thin PZT sheet and is required to be rigid enough to avoid excessive vibrations and bendings. Vibrations are caused by the water jet machining the workpiece and from the water coming up from the catcher; vibrations influence, which is random and uncontrollable, could mask the effect of the factors of interest such abrasive hardness and feed rate. Bendings must be avoided since small deformations can cause cracking and breaking of the PZT sheet.
Slits 2 mm wide have been prepared on two opposite sides of the area where the sheet is placed in order to eliminate the influence of the rebounding jet on the kerf. In fact, in case of a bulk supporting plate, the jet has to machine not only the PZT sheet but also the support, causing the mix of water and abrasive to rebound and machine again the PZT kerf, thus leading to a change in the original characteristics of the generated surface due to more rounded abrasive particles and to a jet with less energy. The cuts will be made in correspondence of the apertures. The slits have been made only on two sides instead of three in order to give a better support to the central area. The two big squared holes in the top are necessary for taking the electrical wires away from the cutting area.
Cuts can be made on the other two sides of the sheet by using a heat gun to melt the wax used to keep the sheet in position on the plate and rotating it of 90°, placing the corner with soldered wires in the other square hole.

A total of 24 cuts can be performed using this procedure: 14 before the rotation of the workpiece and 10 after. The PZT sheet appearance after the cuts is shown in **Figure 4.9**

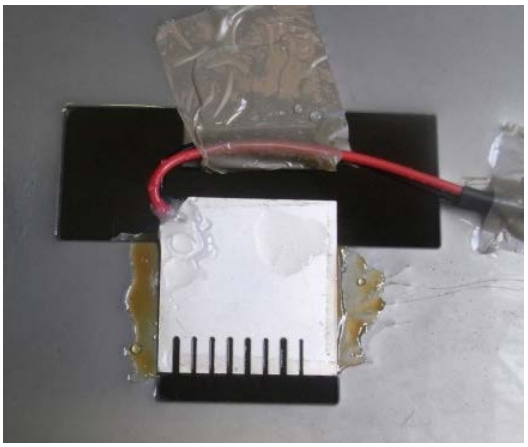

Figure 4.9: Appearance of a machined sheet of PZT

4.3 PZT sheet preparation

This section will show the procedure used for preparing the PZT sheet for the experiments. While the operations involved in the specimen preparation are not particularly complex, attention has to be paid since it is easy to break the sheet because of the brittleness of the material together with the small thickness (0.5 mm) compared to the side dimension (50 mm). **Figure 4.10** shows the PZT sheet.

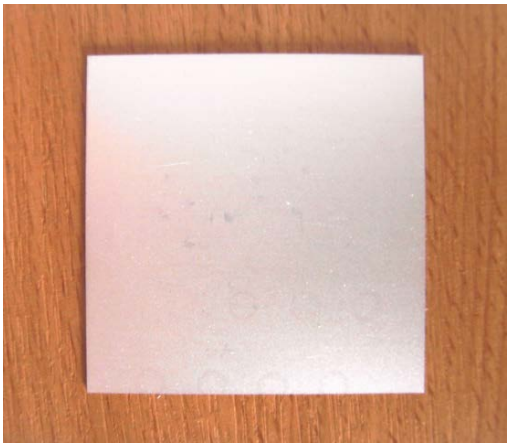

Figure 4.10: A PZT sheet

The first operation performed is the soldering of a wire on each face of the PZT sheet. In fact, the two faces are silver-covered and work as electrodes. A wire to BNC cable (**Figure 4.11**) is necessary for the acquisition of data from the sheet during the cut.

Figure 4.11: Wire to BNC cable

The two wires are soldered in the corner of the faces of the PZT sheet (**Figure 4.12**) in order to limit the occupied area and make it easier to clear the wire from the workpiece when setting it up for the cut. The functioning of contacts has been tested with a multimeter.

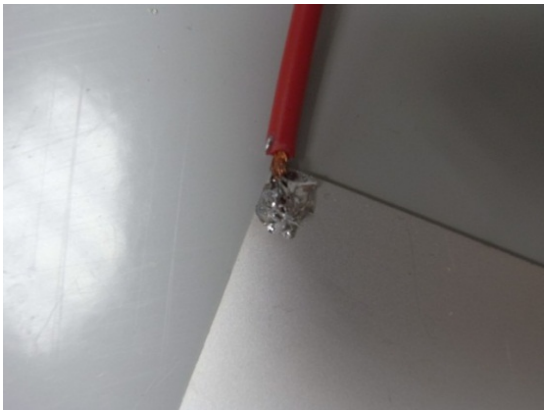

Figure 4.12: Wire soldered to the sheet

Considering the wet working environment, silicon glue has been applied to insulate the soldered area. A layer of orange hot wax has been applied to one side of the sheet: a solid piece of wax was placed on the surface, then melted and spread using a heat gun. The hot wax has the double function of electrically insulate the PZT sheet from the titanium support, thus avoiding short circuits, and strongly bond the workpiece to the supporting plate. **Figure 4.13** shows the appearance of the PZT sheet after the preparation procedure.

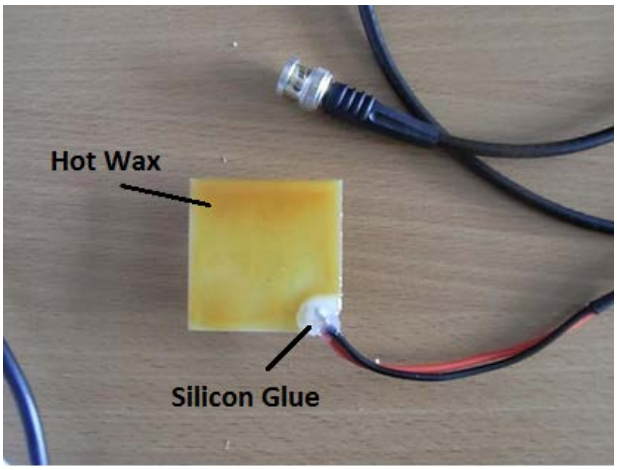

Figure 4.13: PZT sheet after the preparation

To stick the workpiece to the support, a piece of wax has been melted and spread on the titanium plate in the same way used for the PZT sheet. The ceramic has been heated too in order to let the wax melt. The plate and the support has been put in contact and pressure has been carefully applied to eliminate the wax in excess and to have an horizontal surface, paying attention in avoiding the breakage of the PZT sheet. The exceeding wax coming out from the edges has been removed while still melted.
The position of the sheet of PZT on the support is highlighted in red (**Figure 4.14a**). The electrical wires have been fixed to the support with adhesive tape (**Figure 4.14b**).

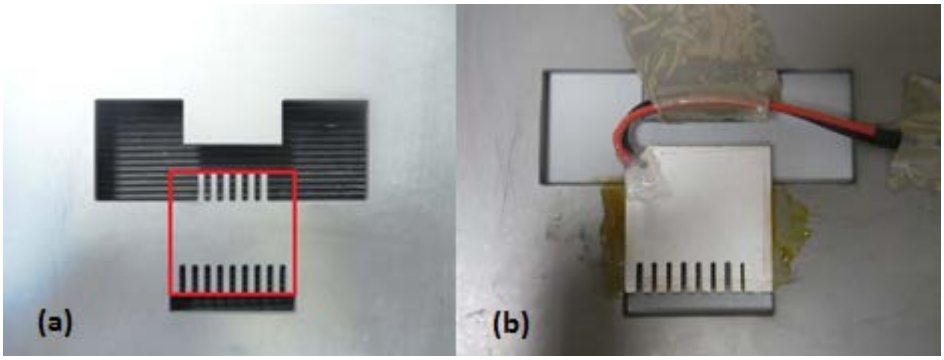

Figure 4.14: PZT sheet positioning

4.4 Signal acquisition and analysis

The electric signal generated by the workpiece during the cutting process has been acquired and analyzed. The evaluated parameters are the Root Mean Square (RMS), the Power Spectral Density (PSD) peak value, the PSD area and the frequency of the peak in the PSD. The signal has been filtered before calculating the parameters. The complete analysis can be found in **Chapter 5**, the Matlab code used for the calculations in **Appendix C** and the full tables of the calculated values in **Appendix A**.

4.4.1 Acquisition procedure

The BNC end of the cable soldered to the PZT sheet has been connected to a Mistras 2/4/6 amplifier (**Figure 4.15**) in the "single" input plug and the gain has been set to 40 dB. The Mistras amplifier has been linked to a power supply set to 0.3 mA and 28 V as required by the datasheet. Another BNC cable has been used to connect the "output" exit of the amplifier to the acquisition card in the computer. A program written in LabView has been used for the acquisition. The signal has been sampled at a frequency of 2.5 GHz. The resonance frequency of the PZT sheet, which represents the maximum frequency band available for the acquisition, has been calculated and its values was around 1.2 GHz. The Nyquist theorem affirms that the sampling frequency must be at least twice the maximum frequency of interest in the acquisition in order to avoid aliasing, thus the use of a sampling frequency of 2.5 GHz. The files with the acquisition data have been converted in .txt format in order to have the possibility to load them in a computing software. The signal has been analyzed using Matlab, a numerical computing environment.

Figure 4.15: The amplifier employed in the experimentation

4.4.2 Extraction of the portion of signal used in the calculations

The central portion of signal has been extracted to evaluate the parameters of interest, thus avoiding possible transient events at the beginning and at the end of the cut. Using the code in **Appendix C**, the following procedure has been used to choose the portion: by zooming in the time domain plot of the signal, the instant corresponding to the beginning of the cut has been found. A length of 2.5 mm of cut has been discarded from that position in order to avoid the transient events and 5 mm of cut has been considered from that point. Since the feed rate changes between the cuts, each signal has a different time length. In order to compare the cuts and considering the same spatial position, the times were converted in physical lengths. **Table 4.1** shows the conversion from cut length (millimeters) to signal length (seconds) for each feed rate used in the experiments.

Table 4.1: Length to time conversion according to feed rates

	Feed rate [mm/min]				
	10	**50**	**70**	**300**	**600**
2.5 mm	15 s	3 s	2.14 s	0.5 s	0.25 s
5 mm	30 s	6 s	4.28 s	1 s	0.5 s

To have a clearer idea of the procedure, a practical example is presented in **Figure 4.16**, which shows the filtered time domain plot of a cut made using alumina as abrasive at 50 mm/s. In this case, the machining of the PZT sheet starts at 7.5 s. As shown in **Table 4.1**, for this specific feed rate the length of 2.5 mm of cut is equivalent to 3 seconds of signal. So, the portion of signal from 7.5 s to 10.5 s is discarded. The considered portion of signal goes from 10.5 s to 16.5 s, as 5 millimeters of cut at 50 mm/min are equal to 6 seconds of signal.

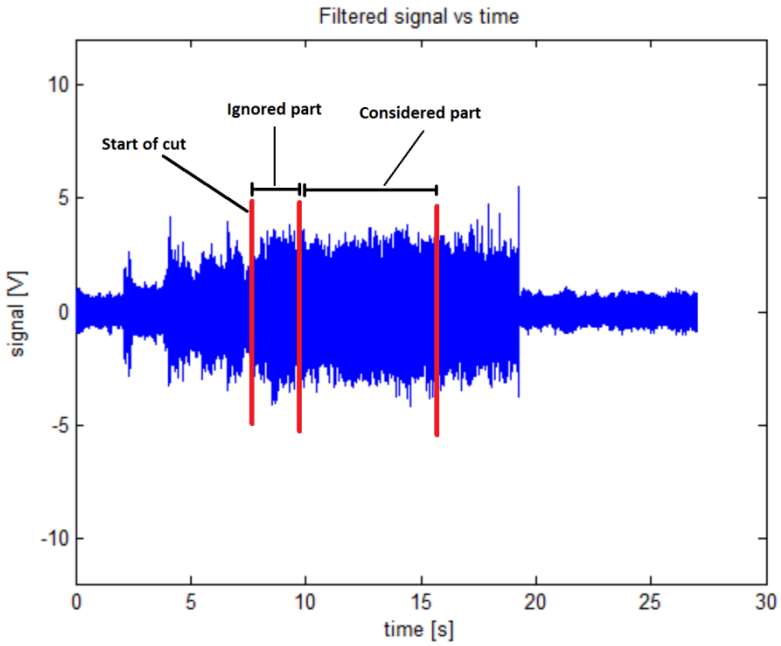

Figure 4.16: Procedure for the extraction of the analyzed signal portion

Each starting and ending position has been found by observing the time domain plot of the signal and using as support the times registered during the experiments by means of a chronometer.

4.4.3 Signal filtering

The signal has been filtered using a lowpass equiripple FIR filter (**Figure 4.17**) with a passband frequency of 200 kHz, a stopband frequency of 300 kHz, a ripple amplitude of 0.1 dB and a stopband attenuation of 100 dB designed using the Matlab Filter Design and Analysis tool (fdatool). The passband and stopband frequencies have been chosen by looking at the PSD graphs (see **Section 4.4.6** for the details about the PSD calculation) of the unfiltered signal and finding where the signal energy was present as in the example shown in **Figure 4.18**. **Figure 4.19** shows a comparison between the time domain plot of the unfiltered signal (**Figure 4.19a**) and filtered signal (**Figure 4.19b**) obtained in a cut using garnet as abrasive, an abrasive mass flow of 100 g/min and a feed rate of 300 mm/min.

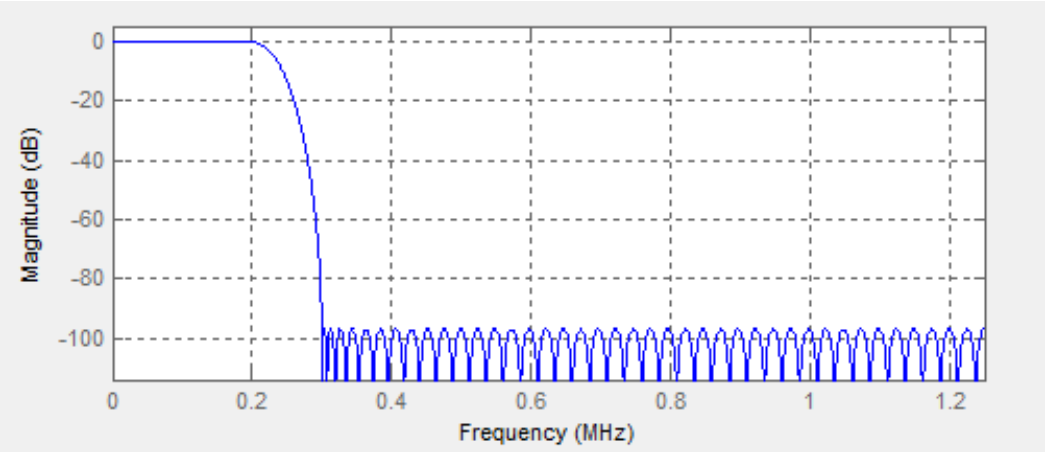

Figure 4.17: FIR pass low filter

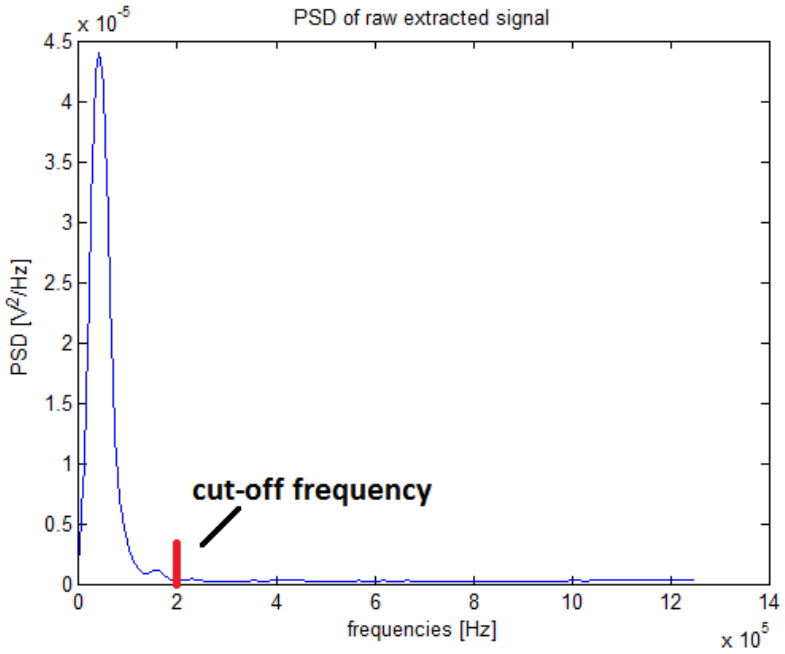

Figure 4.18: PSD of a cut made with garnet, feed rate = 300 mm/min, abrasive mass flow = 100 g/min. All the energy of the cut is before the cut-off frequency

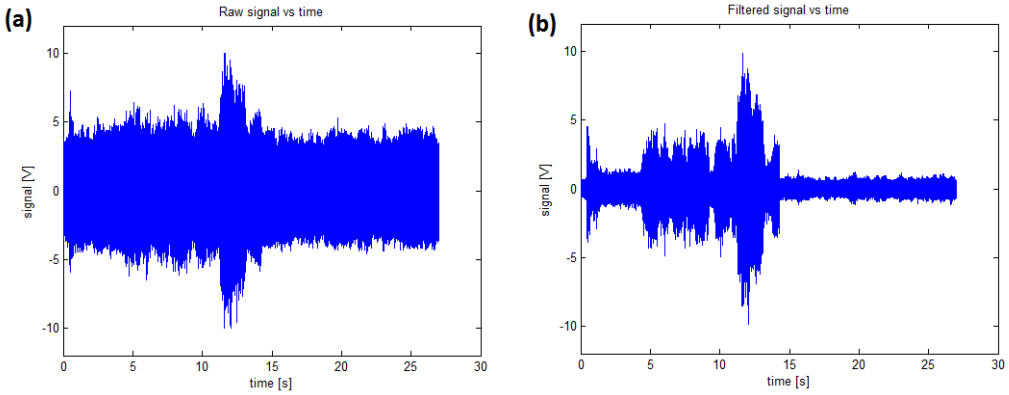

Figure 4.19: Unfiltered (a) and filtered (b) time domain plot of a cut made with garnet, feed rate = 300 mm/min, abrasive mass flow = 100 g/min

4.4.4 RMS calculation

The portion of filtered signal previously extracted as explained in **Section 4.4.2** has been used to evaluate the RMS (Root Mean Square). The RMS is a measure of the magnitude of a varying quantity and is especially useful when the signal oscillates between positive and negative values. The function calculating the RMS value of a vector X N points long is already built in Matlab and uses the following formulation:

$$X_{\mathrm{RMS}} = \sqrt{\frac{1}{N}\sum_{n=1}^{N}|X_n|^2} \tag{4.1}$$

The first second of acquisition has been used to evaluate the noise RMS because the water jet machine is off in that time span and the signal acquired correspond to the electrical noise of the set up. The noise RMS is calculated in order to confront it with the signal RMS. A complete analysis on the signal RMS can be found in **Chapter 5**, **Section 5.3.2**.

4.4.5 FFT calculation

The Fast Fourier Transform has been evaluated for the extracted portion of filtered signal and for the noise. The FFT graphs are single-sided and the amplitudes have been normalized. **Figure 4.20b** shows the filtered FFT of a cut made using alumina as abrasive, an abrasive mass flow of 100 g/min and a feed rate of 300 mm/min. Even if the FFT has not been analyzed, it gives useful information on the signal. A peak in the signal FFT can be found at around 50 kHz for every signal, in accordance to the results of the PSD. The analysis regarding the peak frequency of the PSD can be found in **Section 5.3.5**. The first second of acquisition has been used to evaluate the noise FFT because the water jet machine is off in that time span and the signal acquired correspond to the electrical noise of the set up. The noise FFT has been calculated in order to have

an idea of the behavior of the noise in the frequency domain. **Figure 4.20a** shows the noise FFT of a cut made using alumina as abrasive, an abrasive mass flow of 100 g/min and a feed rate of 300 mm/min. It can be seen that the noise is equally spread on the entire frequency axis and is not concentrated at a particularly frequency. This type of noise is called white noise.

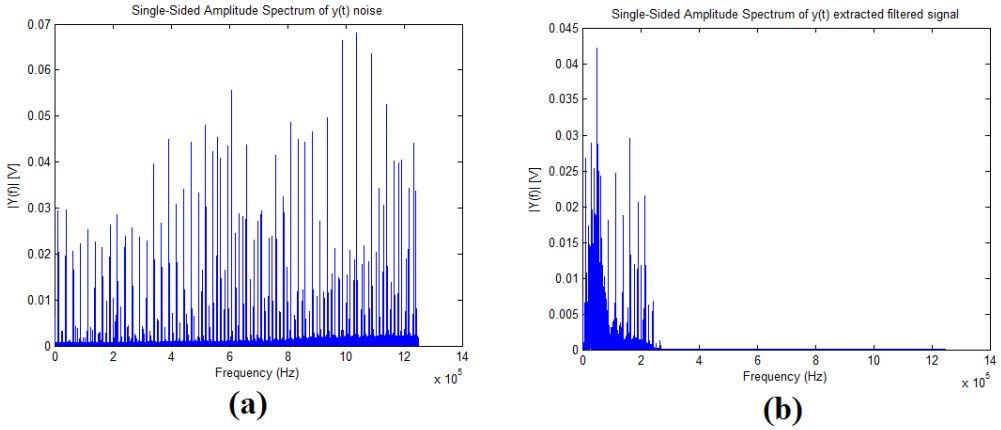

Figure 4.20: FFT of a) noise and b) filtered signal of a cut made with alumina, feed rate = 300 mm/min, abrasive mass flow = 100 g/min (b)

4.4.6 PSD, PSD peak, PSD peak frequency and PSD area calculation

The Power Spectral Density (PSD) of the extracted portion of filtered signal is evaluated using the Welch's method. The peak values and the correspondent frequency have been extracted using the code in **Appendix C** by means of the command "max" which finds the maximum value of an array and the corresponding index. Using the Matlab command "trapz", the area below the PSD curve has been calculated in the 0-200 kHz interval. By definition, the calculated value of the PSD area on the entire frequency domain is equal to the square of the RMS value. **Figure 4.21** shows the PSD graph of a cut made with garnet, feed rate = 300 mm/min, abrasive mass flow = 100 g/min. A complete analysis on PSD peak, PSD peak frequency and PSD area can be found in **Chapter 5** (**Section 5.3.3** for the PSD peak, **Section 5.3.4** for the PSD area and **Section 5.3.5** for the PSD peak frequency).

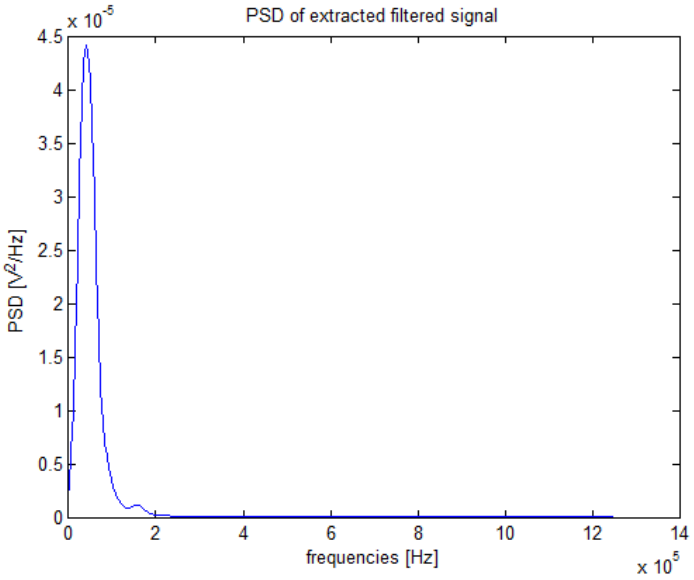

Figure 4.21: PSD of a cut made with garnet, feed rate = 300 mm/min, abrasive mass flow = 100 g/min

4.4.7 Graph examples

This section will present some signal graphs as example. As the graphs for the various cuts are really similar in shape (while the amplitude may vary), only the meaningful ones will be showed.

Time domain plot

Filtered and unfiltered signal time domain plots obtained at different feed rates will be showed. The graphs represent cuts made with alumina, with the abrasive mass flow set at 400 g/min and a variable feed rate of 50 mm/min (**Figure 4.22a** and **Figure 4.23a**), 300 mm/min (**Figure 4.22b** and **Figure 4.23b**) and 600 mm/min (**Figure 4.22c** and **Figure 4.23c**). **Figure 4.22** shows the unfiltered signals while **Figure 4.23** shows the filtered signals.

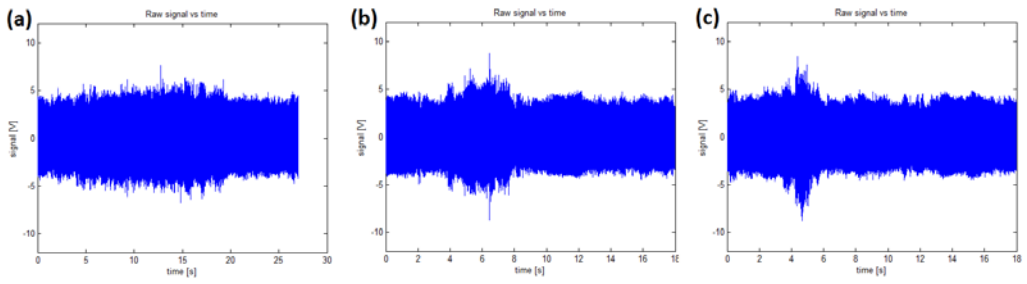

Figure 4.22: Unfiltered signals of cuts made with alumina, abrasive mass flow = 400 g/min, feed rate = 50 (a), 300 (b), 600 (c) mm/min

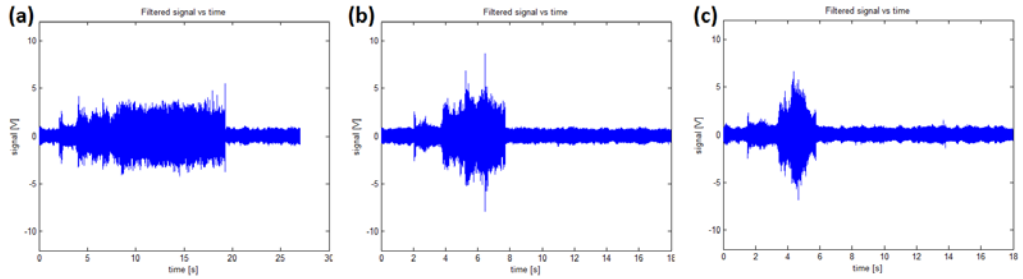

Figure 4.23: Filtered signals of cuts made with alumina, abrasive mass flow = 400 g/min, feed rate = 50 (a), 300 (b), 600 (c) mm/min

Time domain plots of the filtered signal show clearly where the cuts start compared to time domain plots of the unfiltered signal.

FFT plot

The FFT plots of noise, unfiltered and filtered signal are shown in **Figure 4.24a**, **Figure 4.24b** and **Figure 4.24c**. The graphs belong to a cut made with alumina, with the abrasive mass flow set at 400 g/min and a feed rate of 300 mm/min. The FFT plots of the other cuts are similar in shape and are not shown.

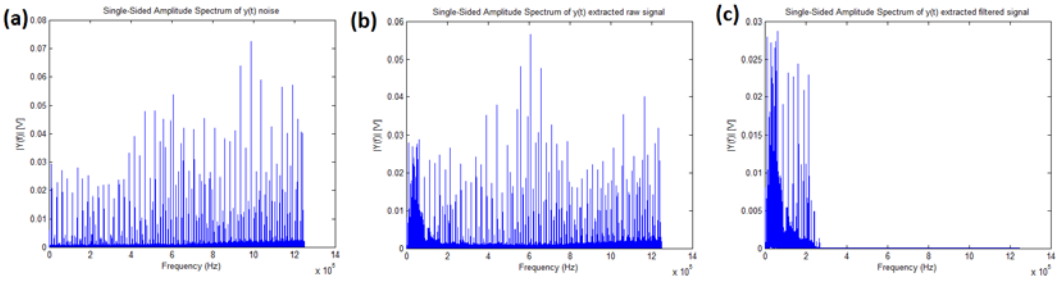

Figure 4.24: FFT of (a) noise, (b) unfiltered signal, (c) filtered signal of a cut made with alumina at feed rate = 300 mm/min and abrasive mass flow = 400 g/min

The noise FFT is distributed uniformly on the frequency axis (**Figure 4.24a**) and thus it is white noise. **Figure 4.24b** shows the presence of the noise in the FFT of the unfiltered signal, while in Figure 4.24c the noise has been removed after the frequency of 200 kHz, making the peak on the left more evident.

PSD plot

As in the case of FFT plots, PSD plots of the various cuts are similar in shape and are not shown except the PSD graphs of unfiltered and filtered signal of a cut made with alumina, with the abrasive mass flow set at 400 g/min and a feed rate of 300 mm/min. **Figure 4.25a** is the PSD plot of the unfiltered signal, **Figure 4.25b** is the PSD plot of the filtered signal.

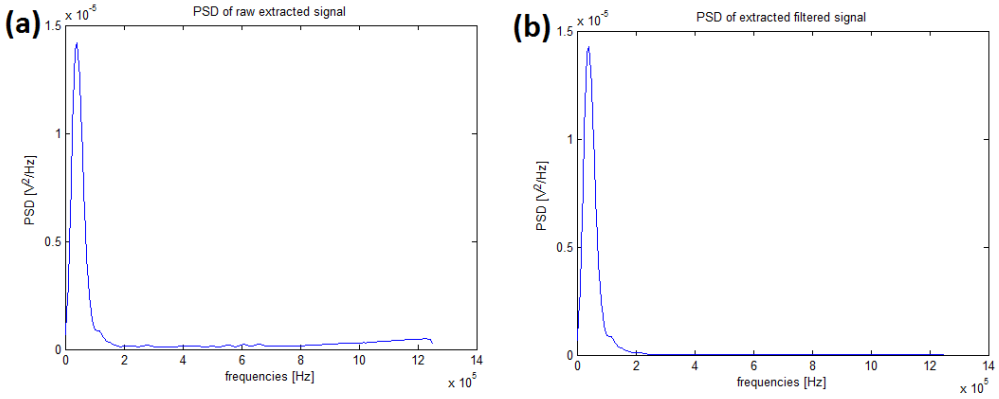

Figure 4.25: PSD of unfiltered signal (a) and filtered signal (b) of a cut made with alumina at feed rate = 300 mm/min and abrasive mass flow = 400 g/min

The peak at around 50 kHz is evident. Since the PSD is almost flat after 200 kHz, the filtering process does not affect remarkably the PSD graph.

4.5 Roughness measurement

To measure the roughness of the kerf, each tooth has been removed from the sheet and cleaned from the remaining wax using a specific powder sold by the producer of the wax. The cleaning powder is dissolved into boiling water and the specimen is dipped into the mix. Measurements have been carried out using the laser gauge of the Taylor-Hobson's Talysurf CLI 1000 machine (**Figure 4.26**).

Figure 4.26: Talysurf CLI 1000

The parameter used for characterizing the surface is the arithmetical mean roughness R_a, defined as follows.

$$R_a = \frac{1}{L} \int_0^L |z(x)| \, dx \tag{4.2}$$

where L is the considered length and z is the measured height.
Since the scanning returns discrete points, the software evaluates R_a by calculating the summation of the absolute height values and averaging them by the number of point as shown in Equation 4.2:

$$R_a = \frac{1}{N} \sum_{i=1}^{N} |z_i| \tag{4.3}$$

Where N is the number of considered points and z_i the height of the i-th point. The correct positioning of the workpiece is relevant, since having the surface rotated respect the machine axis causes a change in the value of R_a. To ensure a correct and coherent positioning of each specimen, the following set up has been used (**Figure 4.27**): two gauges, placed on a metal support, kept the tooth perpendicular to the table. A square ruler has been used to keep the support aligned to the machine axis, while a parallelepiped has been used to keep the gauges parallel to the side of the support. Both the square ruler and the parallelepiped were removed before the beginning of the measurement paying attention in not altering the specimen position.

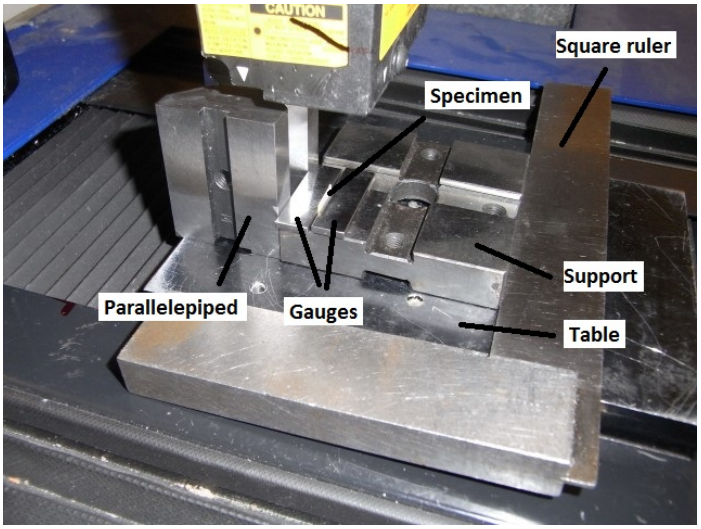

Figure 4.27: Roughness measurement set up

The surface has been measured with a speed of 500 microns/s and one sample per micron on the Y axis (the long side of the specimen). A spacing of 50

microns in the X direction has been used between each scanned line. The scanned length was 5.6 mm, the scanned width 0.9 mm. Then, the surface obtained has been zoomed in to select a 5.6 mm x 0.5 corresponding to the workpiece and leveled in order to remove the slope of the surface by defining a plane P using the least square error method and then by subtracting it from the surface. A line in the central area of the specimen has been extracted. The waviness and the roughness profiles have been separated using a Gaussian filter with a cut-off length λ_c of 0.8 mm and a measured length of $7 * \lambda_c = 5.6$ mm, as the firsts and last 0.8 mm are discarded since they may contains errors related to accelerations and decelerations of the gauge, resulting in an evaluation length of 4 mm. The cut off is the greatest spacing of surface irregularities which are included in the measurement of the surface. It should always be greater than the roughness width in order to obtain a correct evaluation of the R_a value. The values of λ_c and measurement length used are the ones commonly employed when assessing the R_a of mechanical components. The ISO 4288-1996 standard suggests cut off lengths and evaluation lengths depending on the expected roughness for non-periodic profiles as shown in **Table 4.2**. As the expected value of the specimen surface roughness is between 2 and 10 µm (see measured R_a of preliminary cuts in **Appendix A**), the cut-off length, evaluation length and measured length should be equal to 2.5, 12.5 and 17.5 mm. However, this is not possible since the specimen is 10 mm long. For this reason, the cut-off length, evaluation length and measured length are 0.8, 4 and 5.6 mm. In order to not influence the surface roughness with sebum, tweezers have been used for the positioning of the specimens. **Figure 4.28** shows an example of a scansion and parameters evaluation. A complete analysis on surface roughness can be found in **Chapter 5**, **Section 5.3.1**.

Table 4.2: Recommended cut-off [51]

Recommended cut-off			
Non-periodic profiles		Cut-off length Evaluation length	Evaluation length
R_a [µm]	R_z [µm]	λ_c [mm]	L [mm]
to 0.02	to 0.1	0.08	0.4
> 0.02 – 0.1	> 0.1 – 0.5	0.25	1.25
> 0.1 – 2	> 0.5 – 10	0.8	4
> 2 – 10	> 10 – 50	2.5	12.5
> 10	> 50	8	40

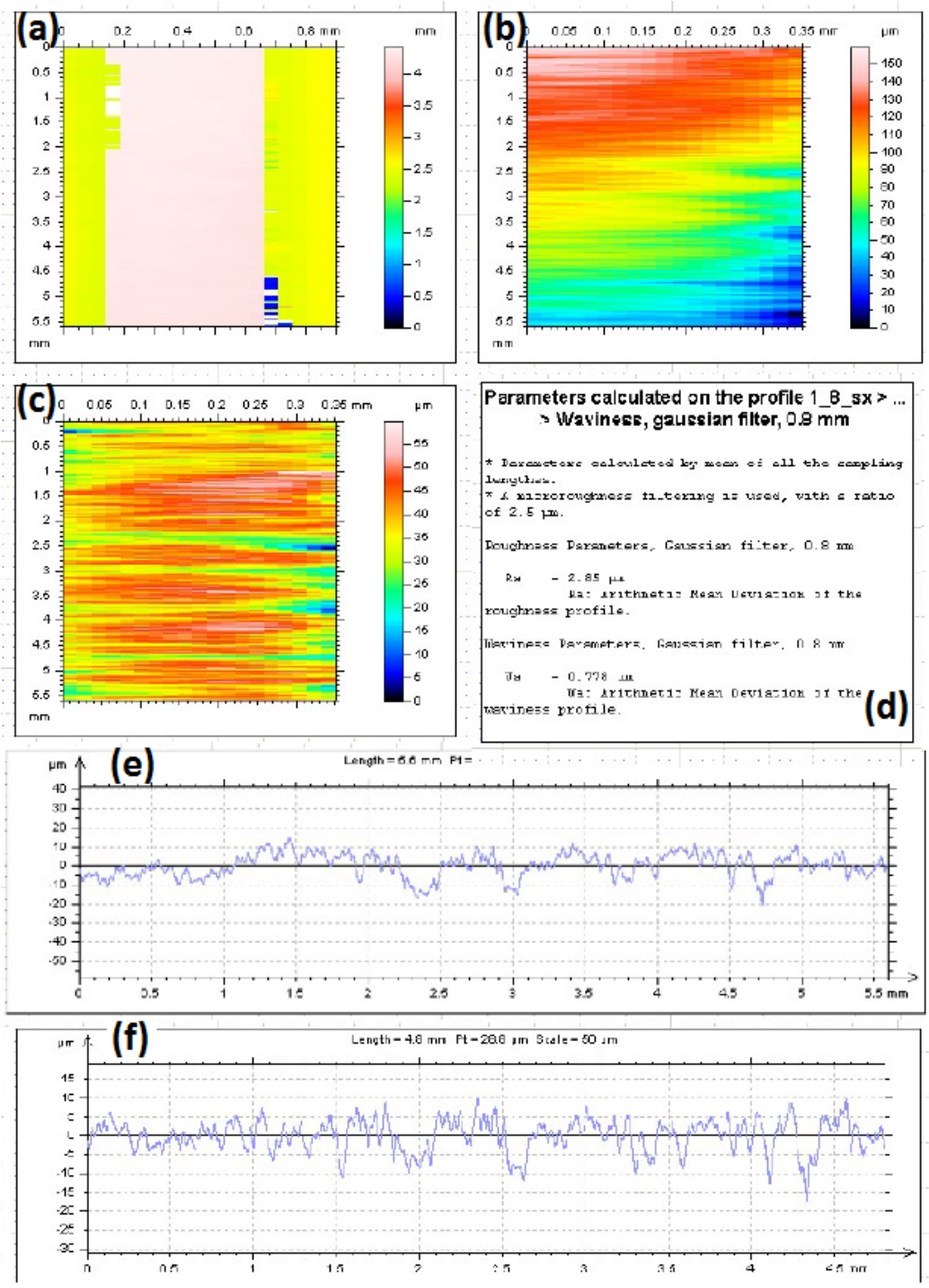

Figure 4.28: a) original scan, b) zoomed surface, c) leveled surface, d) evaluated parameters, e) extracted line, f) roughness profile

4.6 Optical microscope

An optical microscope has been used to observe the wear of the focuser and the abrasive sands. Both the upper and lower sides of the focuser have been evaluated to see if irregular wear was happening. The focuser was flushed with water to eliminate the residuals of abrasive inside the tube, then placed in a vertical position on the microscope table. An enlargement of 50x has been used for the images. The abrasive has been placed on a piece of plastic and pictures have been taken with an enlargement of 100X. The information obtained using the optical microscope has been used in **Chapter 5**, **section 5.3.1** in the analysis of surface roughness.

4.7 Scanning electron microscope

Since PZT is a non conductive material, it must be prepared before the SEM analysis by covering it with a thin layer of a conductive metal. The specimens have been coated of platinum using the sputtering technique. Subsequently, they have been observed in the SEM using the secondary electron beam mode with the beam voltage set at 20 kV. The information obtained using the SEM has been used in **Chapter 5**, **section 5.3.1** in the analysis of surface roughness.

Chapter 5

Experimental Campaign

The experimental campaign has been divided in two parts: the first consists of preliminary cuts, whose aim was to investigate the feasibility of the experiment and have a basic indication of the effect on the signal and on the roughness of the factors of interest. The second part is the proper experimental plan, designed starting from the results of the preliminary cuts.

5.1 Topography of a surface obtained by abrasive water jet

The material removal is caused by complex coexisting phenomena involving plastic deformation, shear and cracking. The material removal is caused by abrasive particles impinging the surface and water erosion. The superior side of the kerf, where the jet has the totality of its energy, presents a cutting wear mode characterized by a smooth surface defined by the roughness values; deeper in the kerf, the surface is generated by deformation wear mode and is characterized by waviness as the jet lost part of its energy and cuts the material more difficultly. [52]
In [27] it is possible to find a summary of the influence of the different water jet and abrasive parameters on the surface roughness. In general, an increase in water pressure affects positively the surface quality causing a reduction in the surface roughness. A higher pressure leads to an increase in abrasive fragmentation probability and this fragmentation reduces the size of the impacting particles. Also, raising the pump pressure increases the abrasive water jet kinetic energy, allowing part of the excess energy to smoothen the surface. As shown in **Figure 5.1a**, the influence of the pump pressure on the roughness value is more evident with the increase of depth of the cut. **Figure 5.1b** illustrates the influence of the orifice diameter and traverse rate on the surface finish. The differences in roughness are not large, despite about a 100% difference in the orifice diameter. What changes with the orifice diameter is the waviness, not the roughness. On the other hand, an increase in the traverse feed leads to a higher value of roughness. The increase in the number of impacting particles at lower traverse rates contributes to the improved surface finish. The additional particles serve to smoothen the surface that forgoing particles generated. **Figure 5.1c** shows that the focusing tube length has no influence on

the surface roughness. **Figure 5.1d** illustrates the changes in roughness due to a variation of the focus diameter. As a certain focus diameter is exceeded, the surface roughness increases with an increase in the focuser diameter. The deeper the cut, the more pronounced becomes the influence of the focuser diameter. The influence of abrasive particles parameters are shown in **Figure 5.2**. Roughness decrease with an increase in the abrasive mass flow rate (**Figure 5.2a**) because a higher number of abrasive particles involved in mixing increases the probability of particle collisions that decreases the average diameter of the impacting particles. For small diameters, **Figure 5.2b** illustrates an almost linear relation between particles diameter and surface roughness: as the diameter increases, the roughness decreases. However, if the particle diameter is higher than a critical value, a further increase in abrasive diameter causes an increase in roughness. Choosing an harder abrasive such as aluminum oxide improves the surface finish if compared to a softer abrasive like garnet (**Figure 5.2c**). Moreover, an harder abrasive could compensate the roughness increase caused by a higher traverse rate. **Figure 5.2d** shows that selecting an appropriate abrasive particle size distribution improves the surface finish.

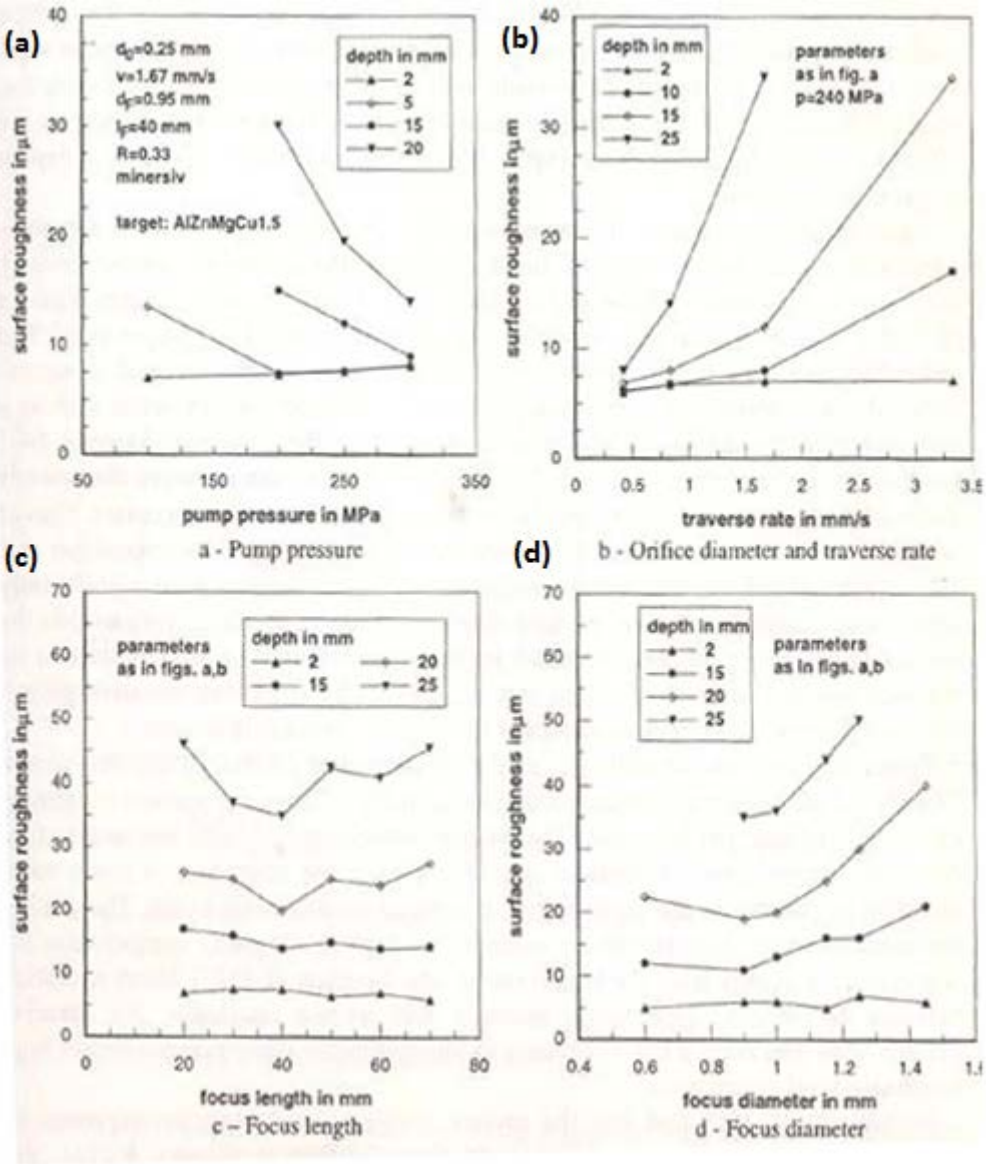

Figure 5.1: Influence of process parameters on surface roughness [27]

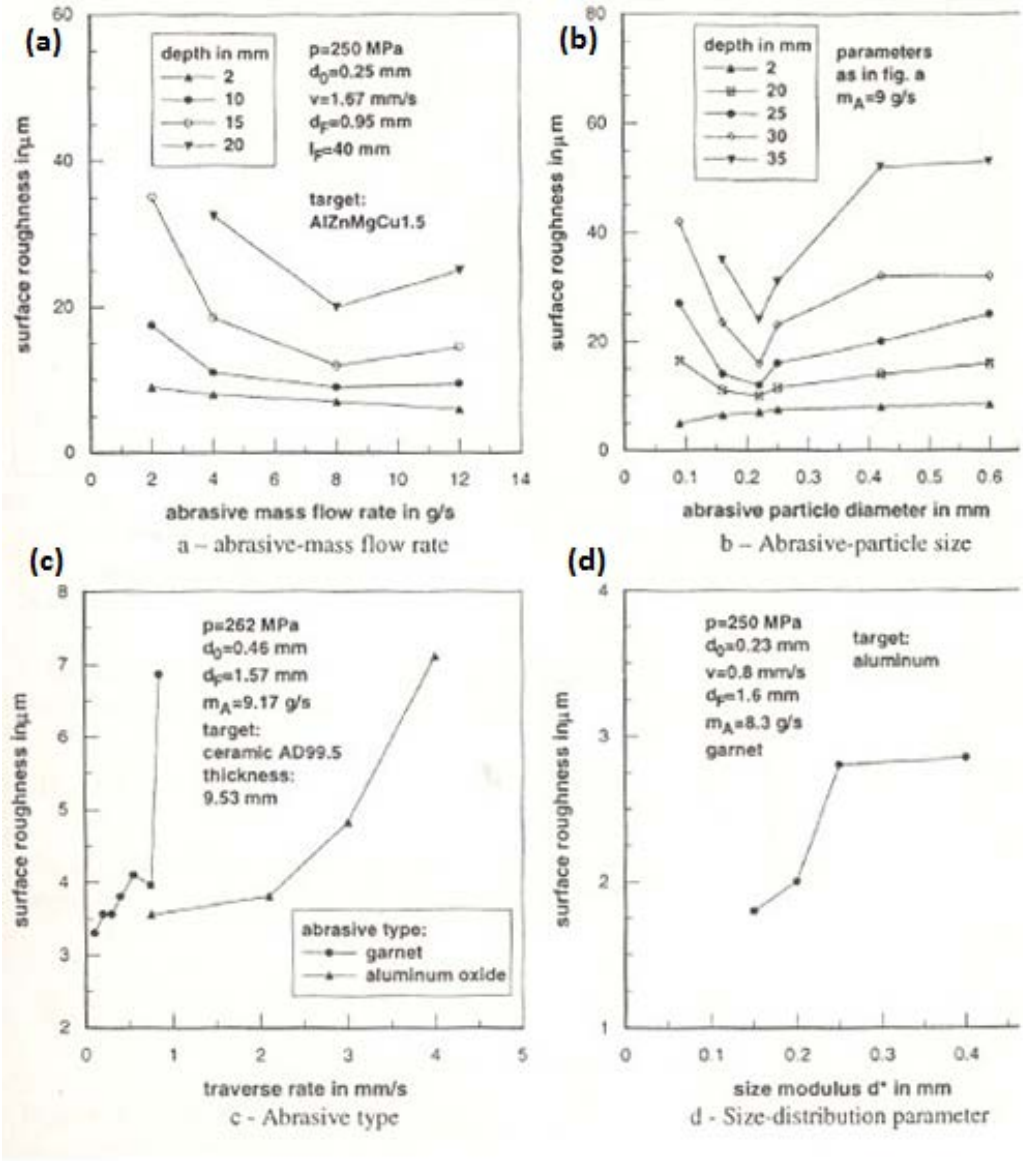

Figure 5.2: Influence of abrasive parameters on surface roughness [27]

5.2 Preliminary tests

Using the set up shown in **Section 4.3**, eight cuts of the length of 10 mm have been performed changing the feed rate and the abrasive mass flow rate while keeping constant the abrasive type and size, the water pressure, the stand off distance, the orifice and focuser diameters as shown in **Table 5.1**. The first experiments were performed at fixed abrasive mass flow (80 g/min) and variable feed rate (10, 70 and 300 mm/min); the following cuts were performed at fixed feed rate (70 mm/min) and variable abrasive mass flow (0, 20, 80, 200 g/min). A table listing the experiments performed in the preliminary phase are listed in **Appendix A**. The parameters evaluated are the surface roughness R_a, the filtered signal RMS, the PSD area of the filtered signal, the filtered signal PSD peak value and the filtered signal PSD peak frequency and the measured values can be found in **Appendix A**.

Table 5.1: Preliminary cuts summarizing table

Fixed parameters	
Stand off distance	1 mm
Pressure	35000 PSI (≈240 MPa)
Orifice diameter	0.3 mm
Focuser diameter	1.02 mm
Cut length	10 mm
Abrasive type	Garnet (mesh 80)
Variable parameters	
Feed rate	10 - 70 - 300 mm/min
Abrasive mass flow	0 - 20 – 80 – 200 g/min
Acquisition parameters	
Amplifier gain	20 - 40 dB
Sampling frequency	2.5 MHz
Evaluated parameters	
Surface roughness Filtered signal RMS Filtered signal PSD area Filtered signal PSD peak value Filtered signal PSD peak frequency	

Cuts axis are 5 mm distant one from the other and the direction of cut is perpendicular to the side of the sheet. The final shape resembles a comb and each "tooth" is 10 mm long and around 4 mm wide since the jet diameter is a little wider than 1 mm (**Figure 5.3**).

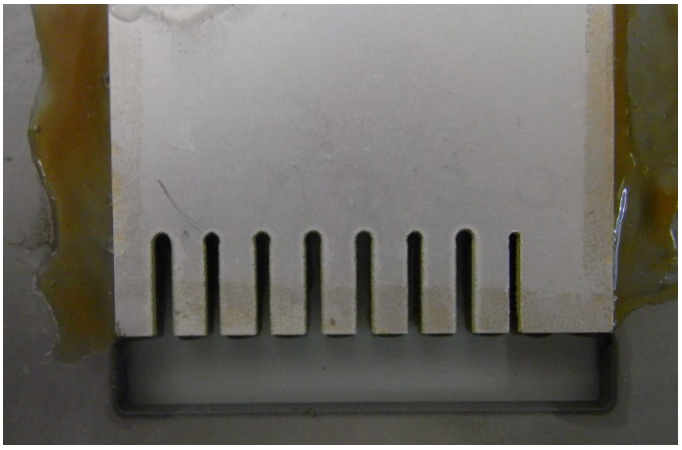

Figure 5.3: Preliminary cuts

A knob on the machine control panel regulate the abrasive mass (**Figure 5.4**). To set the correct value for the abrasive mass flow, the abrasive flow was switched on for a minute and the grit was collected in a container. The sand was then weighted on a scale. The calibration has been performed while the jet was off and for this reason the suction effect generated by the jet will increase the actual mass flow by an unknown quantity. The suction effect depends on the speed of the jet (which depends on the water pressure, see **Section 2.2.3**), but since the pressure is kept constant during the experimentation, the increase in abrasive mass flow will be the same for each cut and thus not relevant.

Figure 5.4: Abrasive mass flow control

After setting the machine up, the procedure used for the cuts was Water pressure and abrasive mass flow controls the following:

1) Positioning of the nozzle 2 millimeters from the workpiece edge
2) Starting of the jet without moving the nozzle
3) Starting moving the nozzle and cutting

The signal has been acquired and analyzed as explained in **Section 4.4**. The preliminary cuts have not been made with the intention of perform a statistical analysis of the result, but only to see which parameters were adequate to machine the material and to have a general indication on the responses trends, if there were any.

5.2.1 Surface roughness analysis

R_a has been measured Using the procedure explained in **Section 4.5**. The table listing the results can be found in **Appendix A**. The R_a analysis is divided in two parts, the first regarding the cuts at fixed abrasive mass flow, the second regarding the cuts performed at fixed feed rate, in order to discover if there are trends related to the abrasive mass flow or to the feed rate. **Figure 5.5** represents the variation in R_a when changing the feed rate with the value of abrasive mass flow set to 80 g/min. It seems that the roughness remain constant for a speed of 10 and 70 mm/min, while increasing the feed to 300 mm/min the surface finish improves. As each manufacturing process has its own process parameters which optimize the final quality of the cut, it is probable that the value of 300 mm/min is close to the optimal process value, thus resulting in a lower value of R_a, or simply the feed rate has no influence on surface roughness and the trend is just random. **Figure 5.6** is obtained by keeping constant the value of the feed rate at 70 mm/min and varying the abrasive mass flow. Cuts made with different values of abrasive mass flow do not seem to present differences in the surface roughness value.

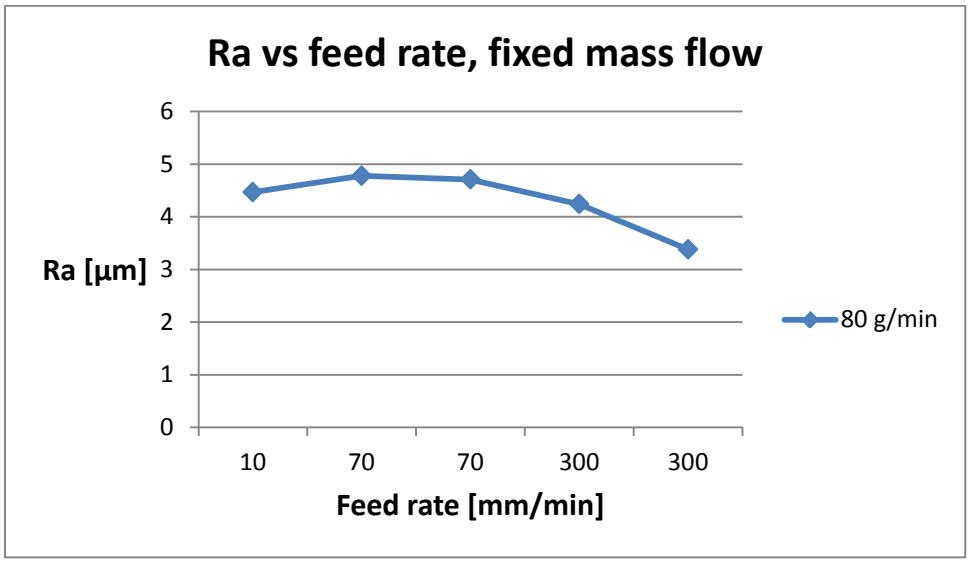

Figure 5.5: R_a vs Feed rate at fixed abrasive mass flow

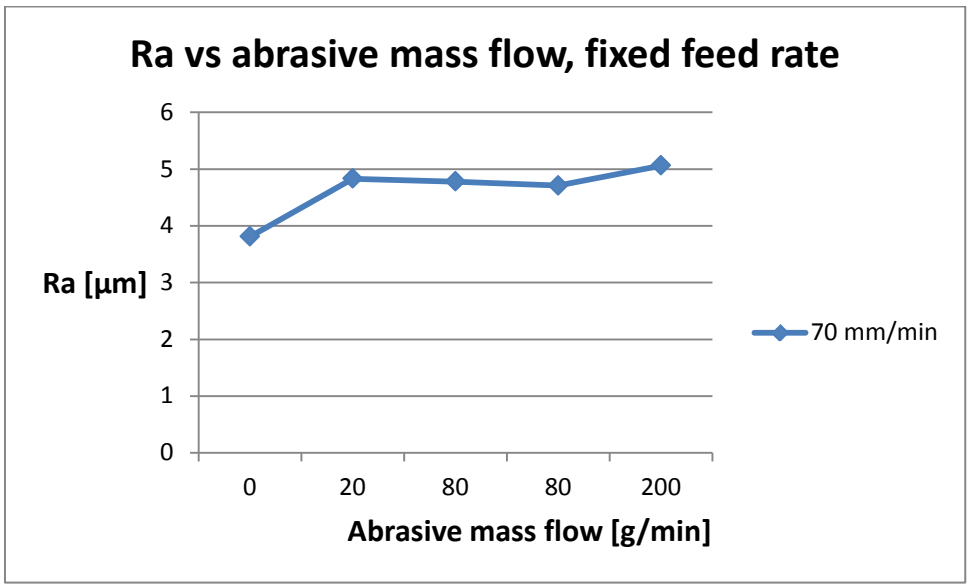

Figure 5.6: R_a vs Abrasive mass flow at fixed feed rate

5.2.2 Signal analysis

Using the Matlab code in **Appendix C**, the signal has been evaluated as explained in **Chapter 4**. Cuts garnet 2 and garnet 3 from **Table A.1** in **Appendix A**, which are made in the same condition (feed rate = 300 mm/min, abrasive mass flow = 80 g/min), have been used for a comparison between a gain of 20 dB (**Figure 5.7a**) and one of 40 dB (**Figure 5.7b**). The gain has been set to 40 dB after comparing the appearance of the two signals. In fact, a gain of 40 dB offers an higher resolution on the vertical axis, in addition to a better distinction between the noise and the proper cut signal.

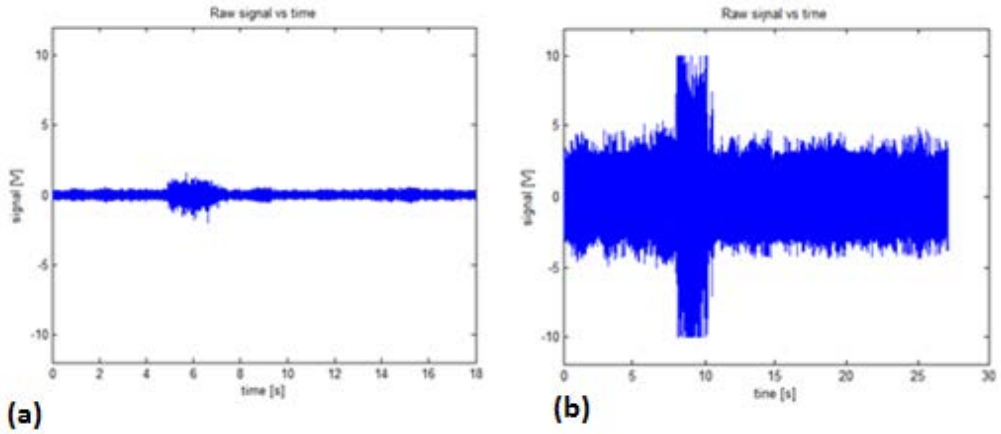

Figure 5.7: Comparison between signals (a) 20dB gain, (b) 40 dB gain

To compare the signal of cut 2 with the other cuts, the acquired data has been multiplied by 10 in order to convert the values obtained using a 20 dB gain to a 40 dB gain. The relationship between voltage gain and decibels gain is the following [53]:

$$G_{\mathrm{dB}} = 20\ \log_{10}\left(\frac{V_2}{V_1}\right) \tag{5.1}$$

A difference in 20 dB is equivalent to a ratio of 10 between voltages.
The cut with a feed rate of 10 mm/min is not present in the following graphs because it has not been possible to calculate the signal parameters. In fact, the file with the signal data is really large and it caused crashes of the computational software and of the computer. The signal analysis is divided in two parts, the first regarding the cuts at fixed abrasive mass flow, the second regarding the cuts performed at fixed feed rate, in order to discover if there are trends related to the abrasive mass flow or to the feed rate. **Table A.5** in **Appendix A** lists all the values of the parameters analyzed in this section. **Figure 5.8**, **Figure 5.9**, **Figure 5.10** and **Figure 5.11** show the results for the preliminary cuts in terms of RMS, PSD area, PSD peak value and PSD peak frequency when the feed

speed is varied between the cuts but the abrasive mass flow is kept constant at 80 g/min. From the preliminary cuts, it seems that increasing the feed rate causes an increase in RMS, PSD area and PSD peak value. On the other hand, there are no visible trends in the peak frequency value.

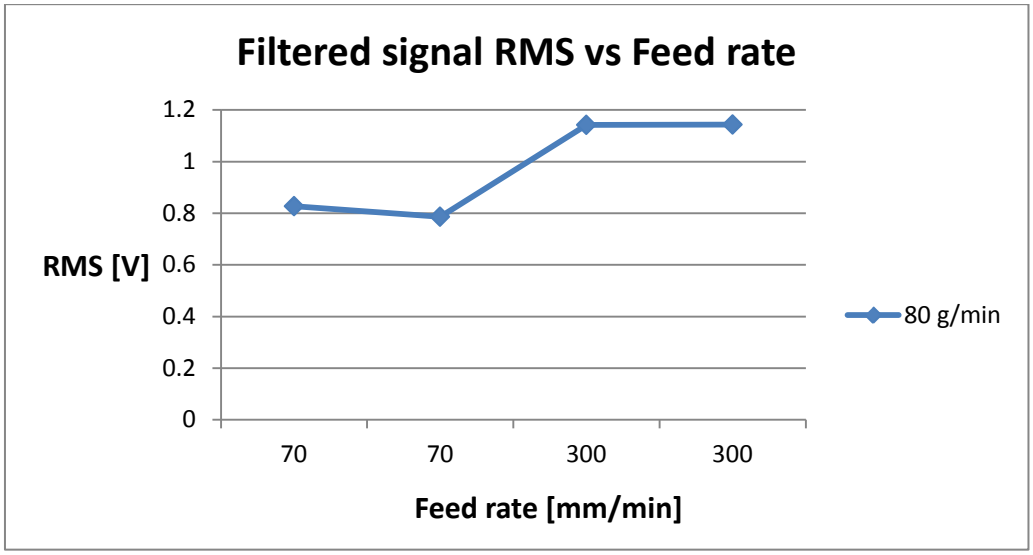

Figure 5.8: Filtered signal RMS vs Feed rate at fixed abrasive mass flow

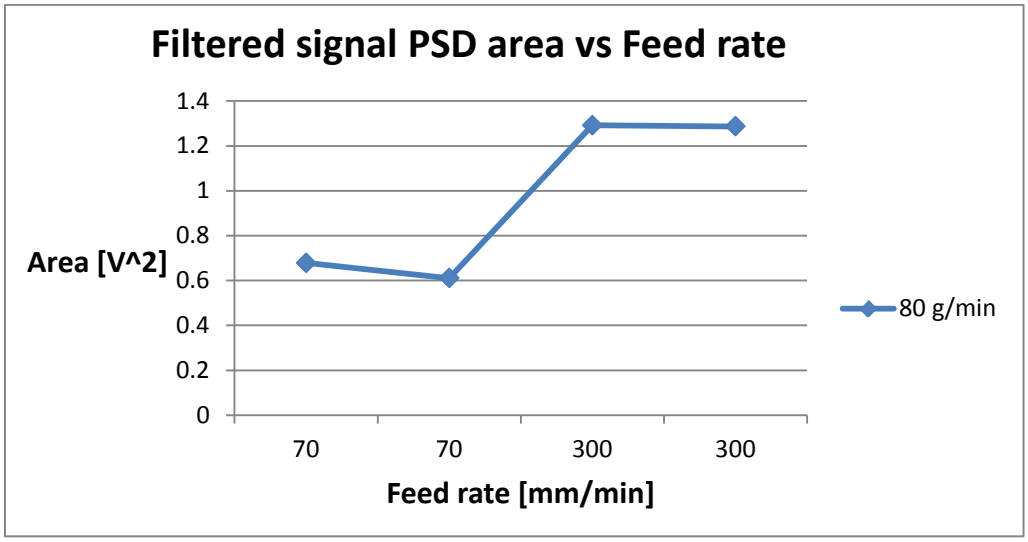

Figure 5.9: Filtered signal PSD area vs Feed rate at fixed abrasive mass flow

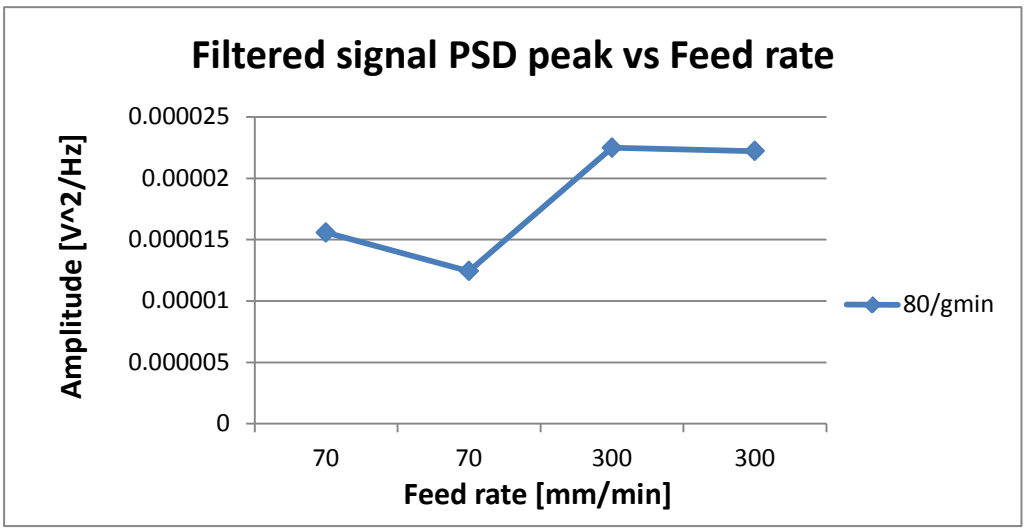

Figure 5.10: Filtered signal PSD peak vs Feed rate at fixed abrasive mass flow

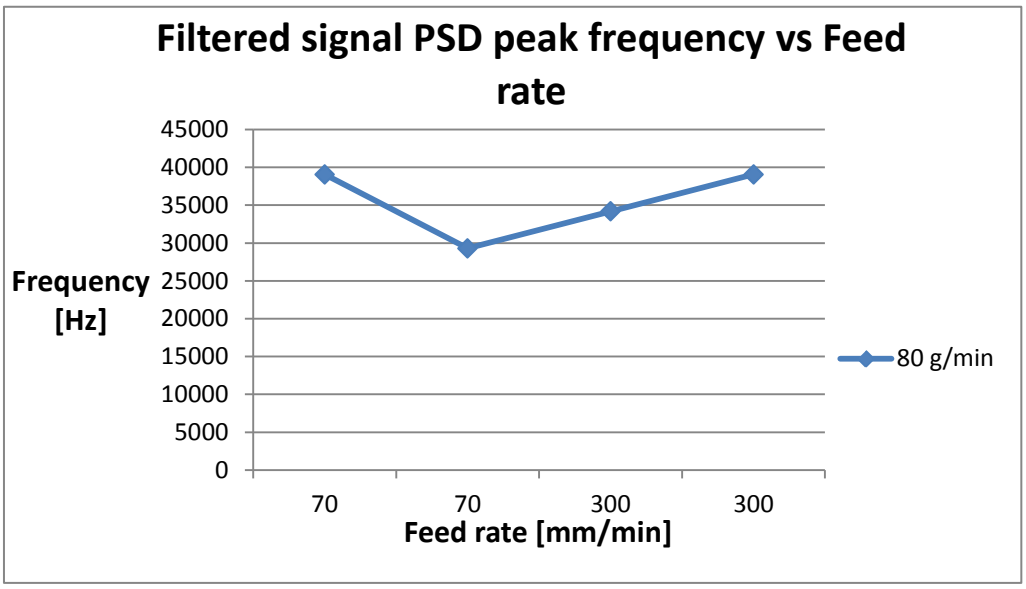

Figure 5.11: Filtered signal PSD peak frequency vs Feed rate at fixed abrasive mass flow

Conversely, in **Figure 5.12, Figure 5.13, Figure 5.14 and Figure 5.15** the results for the preliminary cuts in terms of RMS, PSD area, PSD peak value and PSD peak frequency when the feed rate is set to the constant value of 70 mm/min and the abrasive mass flow is changed are shown. In all those four graphs, no trends are present. The RMS of the cut performed at 20 g/min in **Figure 5.12** seems too low compared to the other values. However, no external events that could have influenced the test happened.

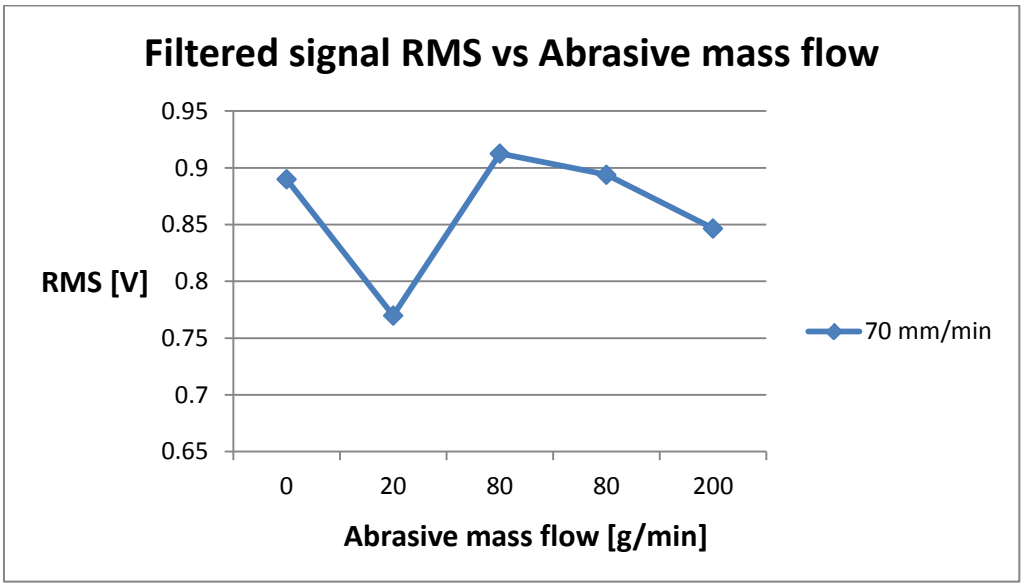

Figure 5.12: Filtered signal RMS vs Abrasive mass flow at fixed feed rate

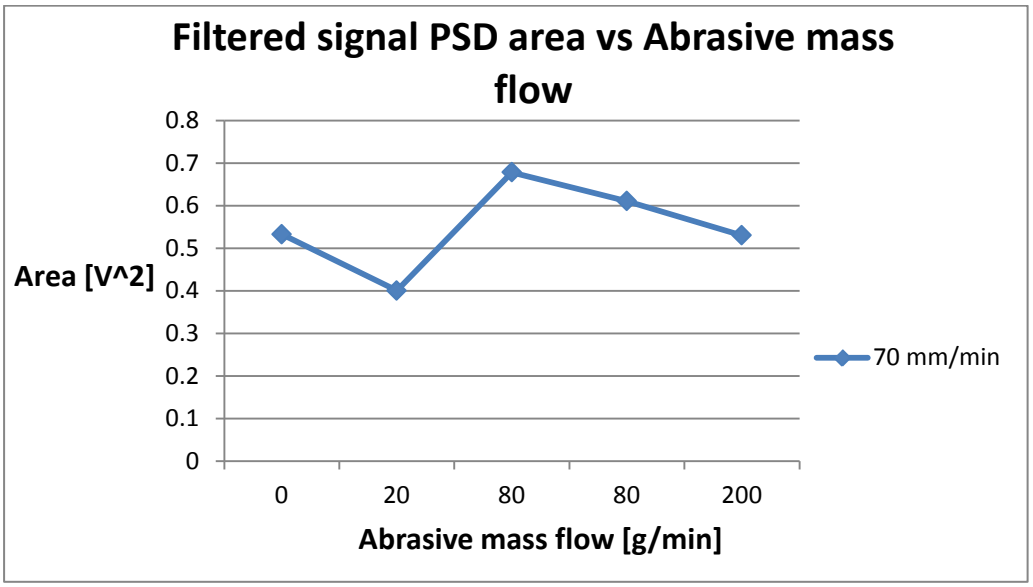

Figure 5.13: Filtered signal PSD area vs Abrasive mass flow at fixed feed rate

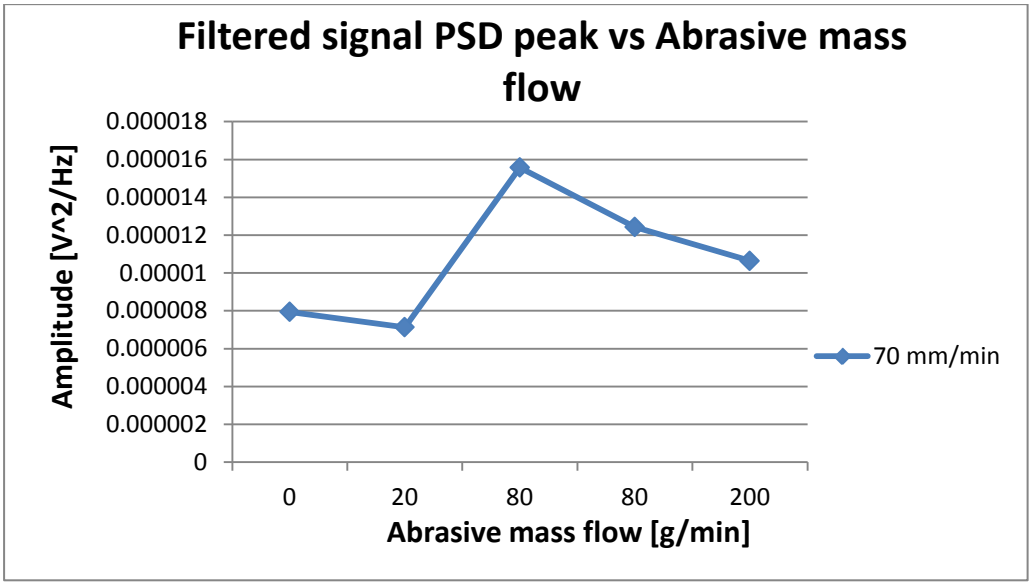

Figure 5.14: Filtered signal PSD peak vs Abrasive mass flow at fixed feed rate

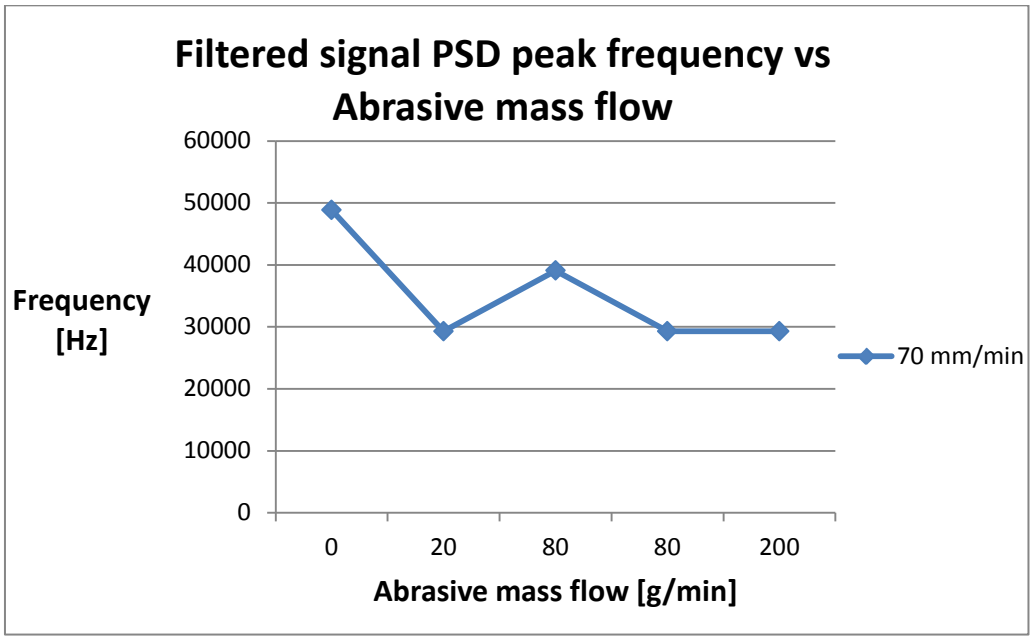

Figure 5.15: Filtered signal PSD peak frequency vs Abrasive mass flow at fixed feed rate

5.3 DOE experimental plan

A DOE approach has been used to design an experimental plan. In fact, the high cost of a material sheet, the scarcity of abrasive and the limited availability of the water jet machine require a careful planning. As this work is an attempt to understand the behavior of a ceramic material in terms of surface finish and no information are available regarding the outcomes of the signal acquisition, the plan must offer the possibility to analyze all the possible influences and interaction while keeping the number of experiments relatively low. For these reasons, the plan chosen for the experimentation is a full factorial plan with three factors, namely the abrasive mass flow, the abrasive type and the feed rate, with respectively two, three and three levels replicated twice for a total of 36 experiments (2 replicates x 3 feed rate x 3 abrasive types x 2 mass flow levels). As explained in **Chapter 4**, 24 cuts can be made on each PZT sheet. For this reason, two sheets of PZT are required. Considering the results of the preliminary analysis, it has been decided to use only two levels of abrasive mass flow. The choice of 100 g/min and 400 g/min is due to the fact that the two values should be not too close and the total consumption should be lower than the available abrasive quantity. On the other hand, feed rate seems to have an effect on the electric signal and three levels (50, 300 and 600 mm/min) were used. As one of the scopes of this work is to investigate the effect of the abrasive on the surface roughness, garnet, white alumina and silicon carbide were employed.
It has not been possible to constantly change the two sheets of PZT (as each set up change took between 30 and 45 minutes); this led to the use of a blocking approach: each replicate was placed on a different sheet and, in the statistical analysis, the block factor was introduced to take in account the effect of the change in set-up and to understand if it has an influence on the results.
Table 5.2 summarizes the experimental parameters, while **Table A.2** in **Appendix A** lists all the experiments performed in this phase of the experimentation.

Table 5.2: DOE experimental plan cuts summarizing table

Fixed parameters	
Stand off distance	1 mm
Pressure	35000 PSI (≈240 MPa)
Orifice diameter	0,3 mm
Focuser diameter	1.02 mm
Cut length	10 mm
Variable parameters	
Abrasive type	Garnet (6.5 – 7.5 Mohs), white alumina (9 Mohs), silicon carbide (9 – 9.5 Mohs)
Abrasive mass flow	100 – 400 g/min
Feed rate	50 - 30 - 600 mm/min
Acquisition parameters	
Amplifier gain	40 dB
Sampling frequency	2.5 MHz
Evaluated parameters	
Surface roughness Filtered signal RMS Filtered signal PSD area Filtered signal PSD peak value Filtered signal PSD peak frequency	

As this is an explorative campaign, a fixed value of $\alpha = 5\%$ has been used without a Bonferroni correction. α is the significance level of a test and it is a threshold value used to judge whether a factor is statistically significant. If the p-value of a parameter is less than α, that parameter has an effect on the response. The triple interaction cannot be evaluated since including it into the analysis would result in no degrees of freedom left for the evaluation of the model error. At least a replication is needed to include the triple interaction in the model. In this case, the required degrees of freedom for the evaluation of the model error would come from the replicates and not from the elimination of the triple interaction.

5.3.1 Surface roughness analysis

The ANOVA analysis shows that only the abrasive type influences the surface roughness, while abrasive mass flow and feed rate do not affect the cut. This is probably due to the small thickness of the material and the high pressure used in the cuts. In this condition, the changes in feed rate and abrasive mass flow in the range investigated do not have a relevant influence on the generated surface. **Figure 5.16** shows the main effects plot for R_a. The interaction plot (**Figure 5.17**) seems to show interactions between the parameters, but the ANOVA analysis affirms that there are no relevant interactions. Moreover, the block factor is not influencing the results. The full ANOVA table can be found in **Appendix B**, **Section B.1**, the entire list of measured values for R_a can be found in **Appendix A**.

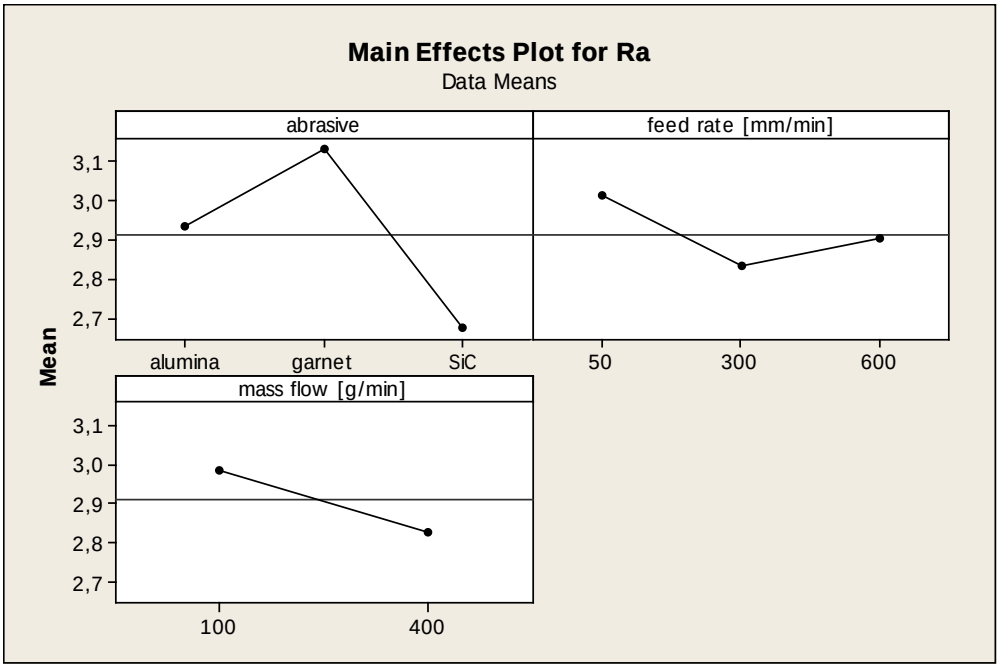

Figure 5.16: R_a main effect plot

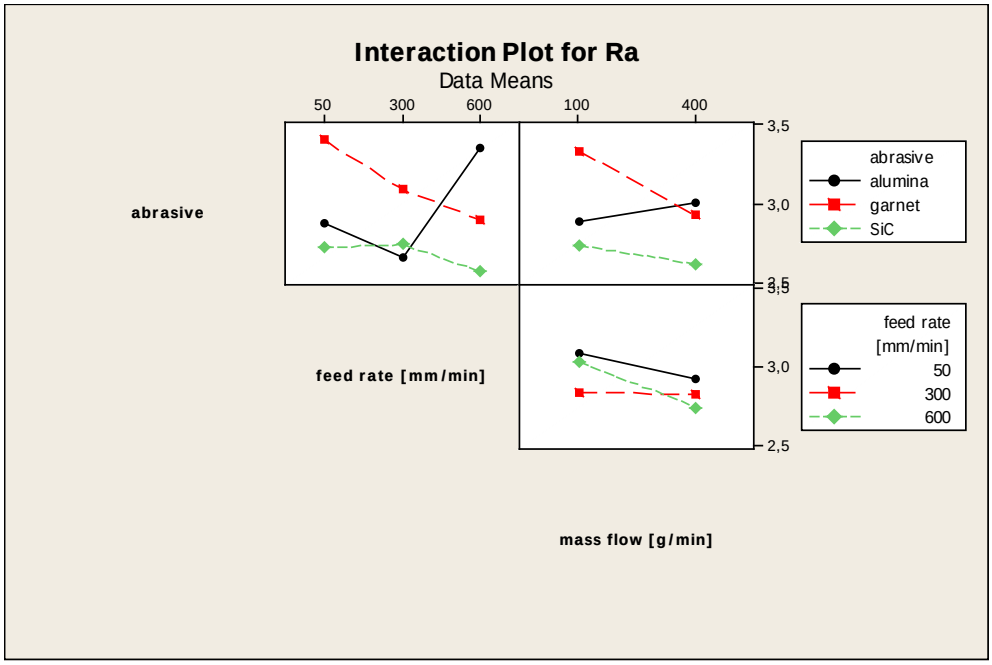

Figure 5.17: R_a interaction plot

The influence of the abrasive type is probably related to the different shape and hardness of the grains. In fact, garnet is the blunter and softer abrasive among the three used in the experiments and has the worst surface finish with an average R_a of 3.13 µm compared to a value of 2.93 µm for alumina and 2.67 µm for silicon carbide. **Figure 5.18**, **Figure 5.19** and **Figure 5.20** show the three abrasives used in the cuts with an enlargement of 100X.

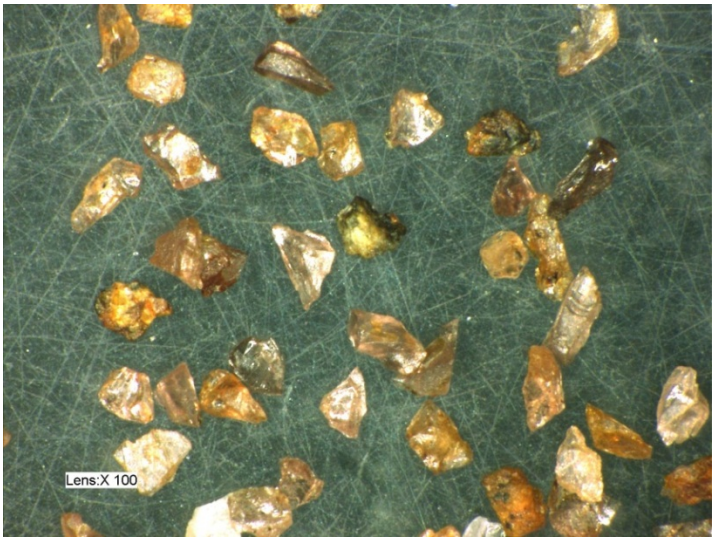

Figure 5.18: Garnet observed with an optical microscope

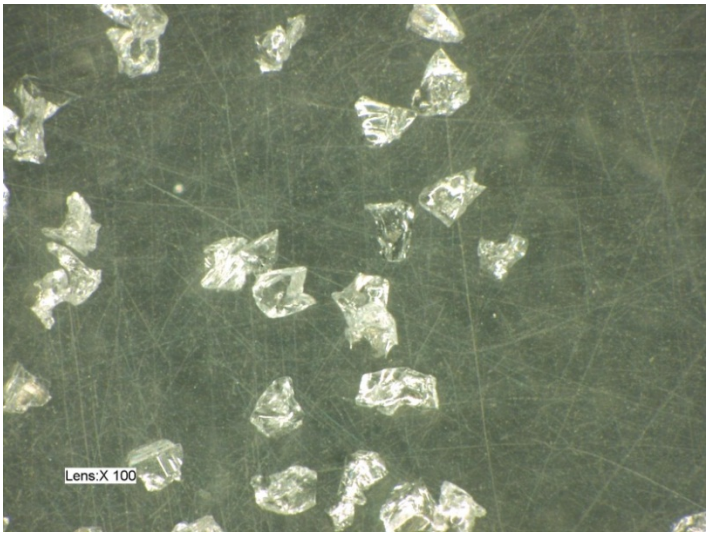

Figure 5.19: Alumina observed with an optical microscope

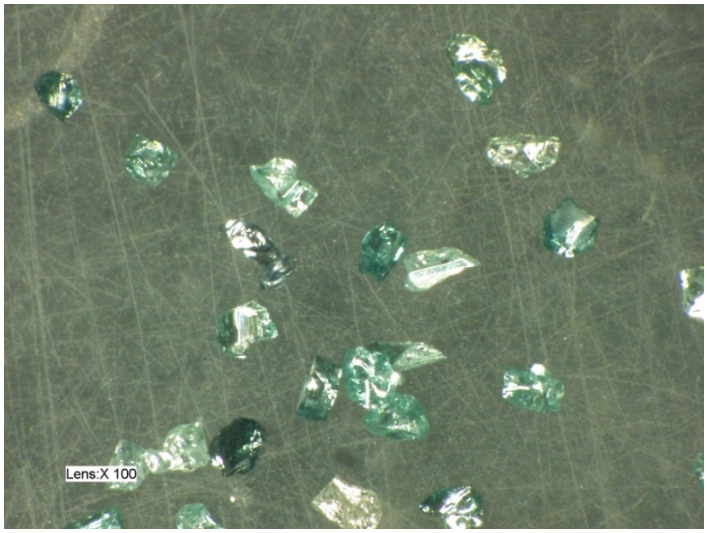

Figure 5.20: Silicon carbide observed with an optical microscope

Three surfaces obtained at a feed speed of 300 mm/min, a mass flow of 100 g/min and using the three different abrasives have also been investigated with the SEM. The surface is not cleaned in order to not affect the machined kerf. **Figure 5.21** shows the surface obtained using garnet, **Figure 5.22** using alumina and **Figure 5.23** using silicon carbide. The surface machined with silicon carbide appears to be the smoothest one, while the one obtained using garnet seems to be more rough.

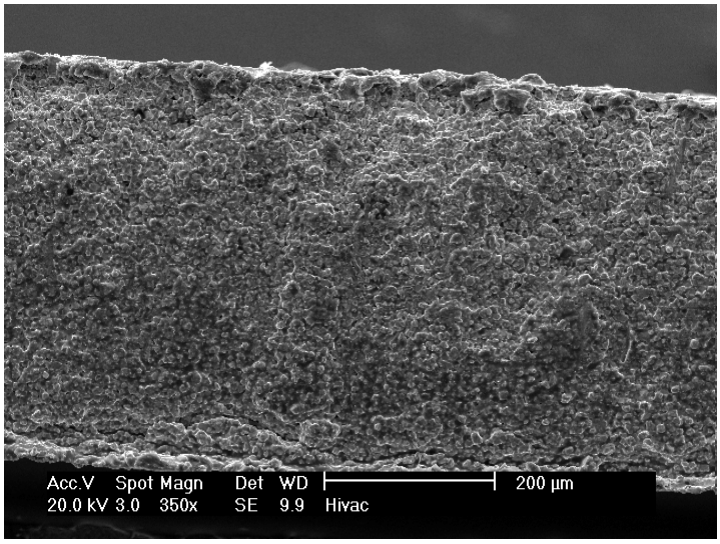

Figure 5.21: Surface machined with garnet observed with SEM at 350X

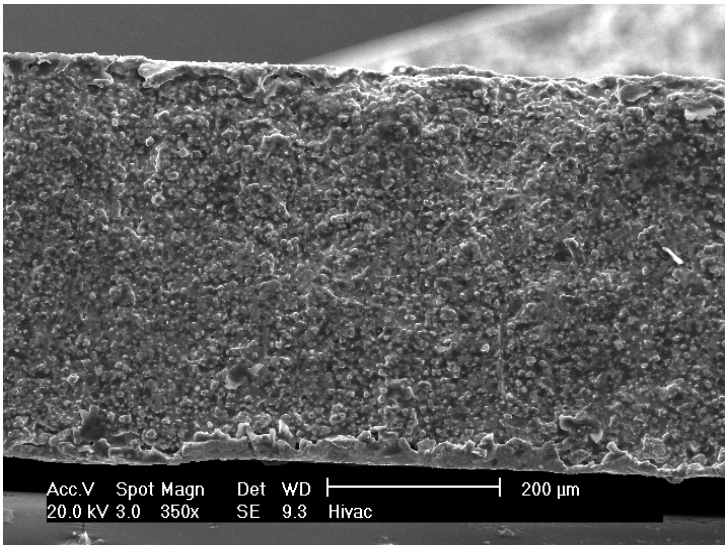

Figure 5.22: Surface machined with alumina observed with SEM at 350X

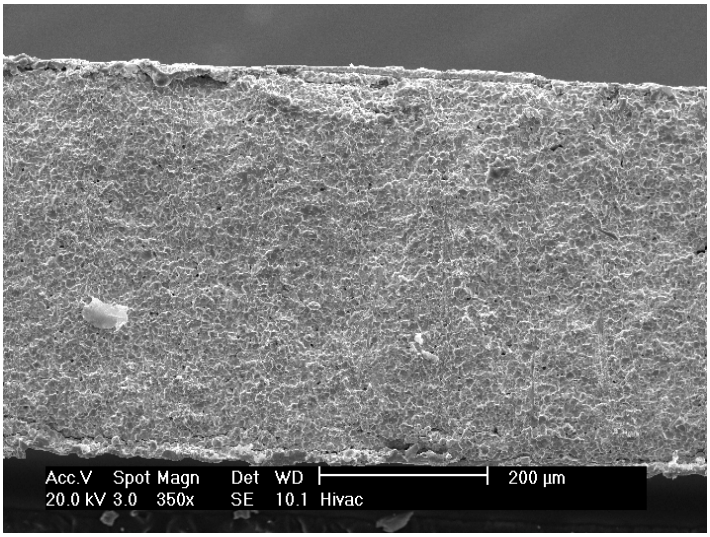

Figure 5.23: Surface machined with silicon carbide observed with SEM at 350X

The kerf surface is generated by intergranular cracking and removal of entire grains of material since the powder grains forming the surface appear to be intact. However, it is possible to find some microcuts on the surface (**Figure 5.24**). Microcuts are incisions, which are caused by the plastic flow of the machined material, left by the abrasive hitting the surface at shallow angles of impact; their number and depth increase whit the increase in abrasive hardness. Still, they have no influence on the R_a value as their number remains limited.

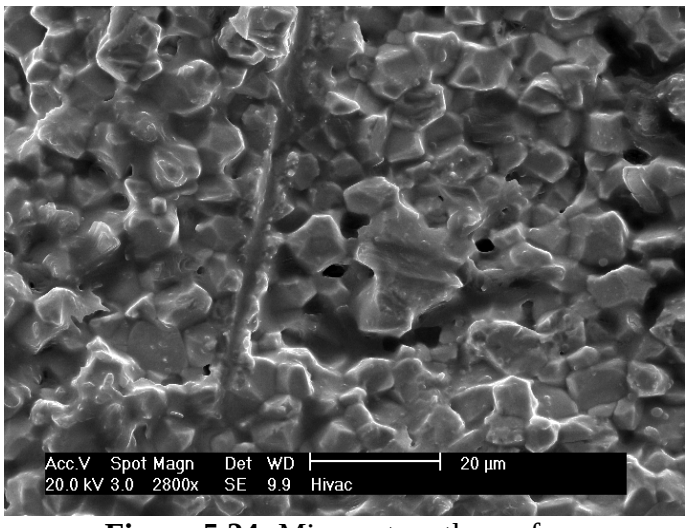

Figure 5.24: Microcut on the surface

The small thickness of the workpiece lead to a uniform surface without evident differences from the top to the bottom side of the kerf. The inferior edges (where

the jet comes out from the workpiece) do not show signs of chipping thanks to a rigid and well-supporting fixturing system. **Figure 5.25** shows an image of the machined surface obtained using an optical microscope and an enlargement of 175X. There is no chipping on the inferior edge.

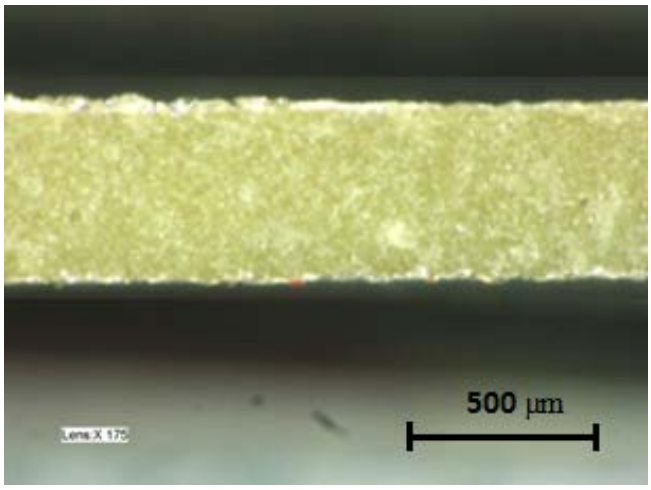

Figure 5.25: Machined surface observed at optical microscope. No traces of chipping are present

Finally, the cutting process is not influenced by the wear of the nozzle. The diameter increases by 10%, starting from 1.11 mm and ending at 1.22 mm after the experimental campaign. As explained in **Section 5.1,** such small change in dimension has no effect on the surface roughness,.

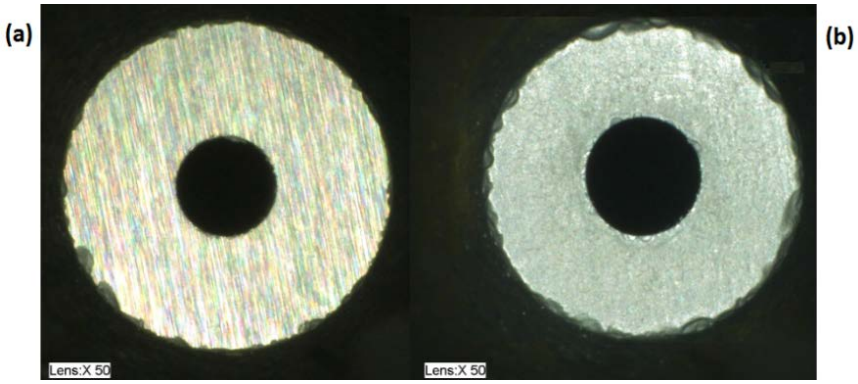

Figure 5.26: The exit diameter of the focuser before (a) and after (b) the cuts

5.3.2 Filtered signal RMS analysis

The ANOVA analysis shows that the significant parameters are the feed rate, the abrasive mass flow and the interaction between feed rate and abrasive mass flow. The block factor results not relevant in the analysis. **Figure 5.27** shows the effect of the parameters on the RMS value; **Figure 5.28** is the interaction plot between the factors investigated. The full ANOVA table can be found in **Appendix B**, **Section B.2**, the entire list of calculated values for RMS can be found in **Appendix A**.

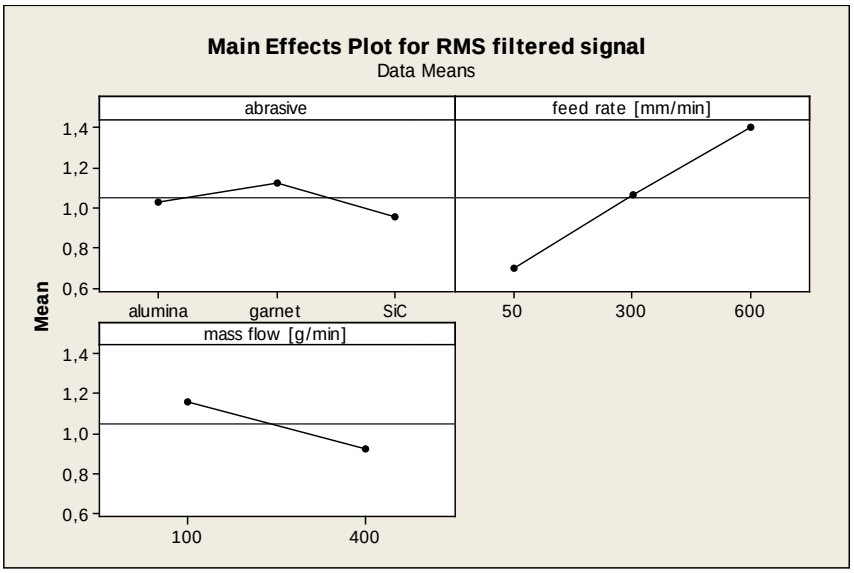

Figure 5.27: Filtered signal RMS main effects plot

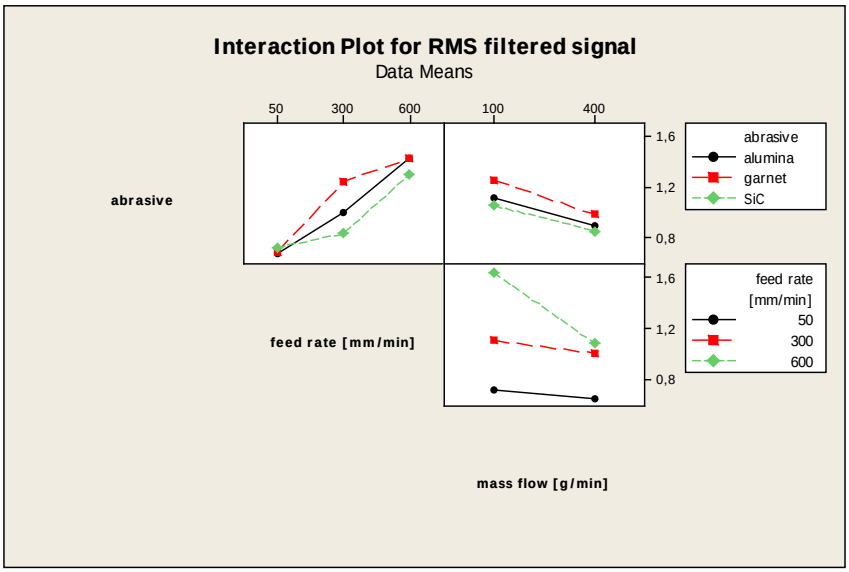

Figure 5.28: Filtered signal RMS interaction plot

5.3.3 Filtered signal PSD peak analysis

After computing the PSD, the peak value expressed in $\frac{V^2}{Hz}$ has been considered. The ANOVA results show that the block factor is not relevant. The significant parameters are the feed rate, the abrasive mass flow and the interaction between feed rate and mass flow. **Figure 5.29** and **Figure 5.30** show graphically the results of the ANOVA analysis. The full ANOVA table can be found in **Appendix B**, **Section B.3**, the entire list of calculated values for PSD peak can be found in **Appendix A**.

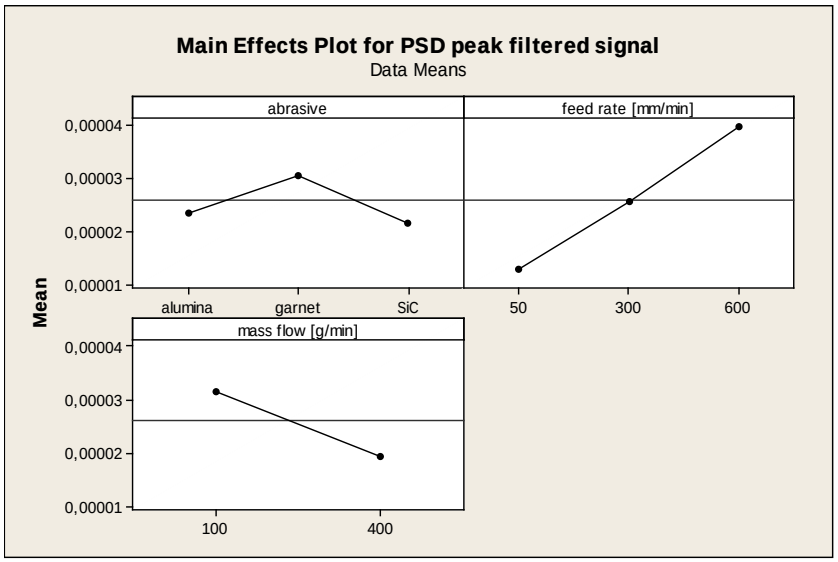

Figure 5.29: Filtered signal PSD peak value main effects plot

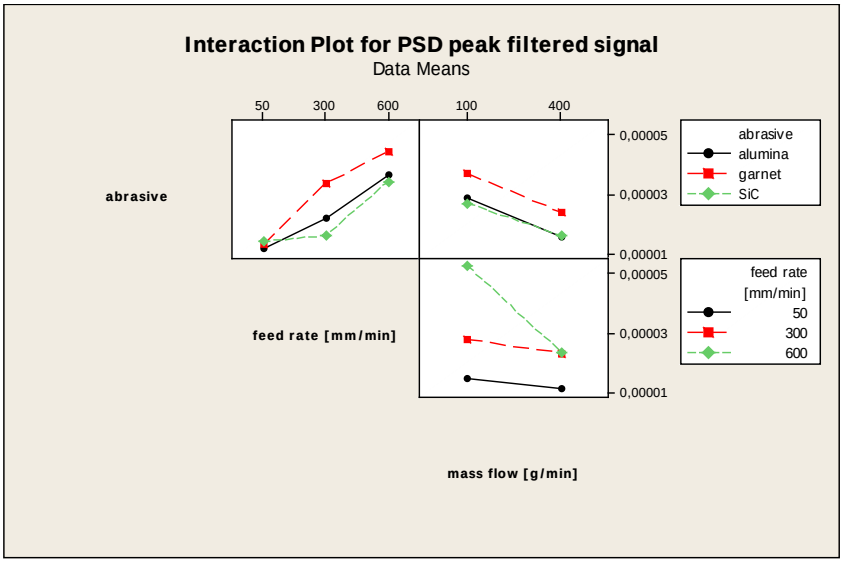

Figure 5.30: Filtered signal PSD peak value interaction plot

5.3.4 Filtered signal PSD area analysis

The area below the PSD graph has been calculated between 0 and 200 kHz. Since its value is the square of the RMS, the results of PSD area analysis are expected to be coherent with the results of RMS analysis. The block factor results not relevant in the analysis. The significant parameters are the feed rate, the abrasive mass flow and the interaction between feed rate and mass flow. **Figure 5.31** and **Figure 5.32** show respectively the main effect plot and the interaction plot of PSD area. The full ANOVA table can be found in **Appendix B**, **Section B.4**, the entire list of calculated values for PSD area can be found in **Appendix A**.

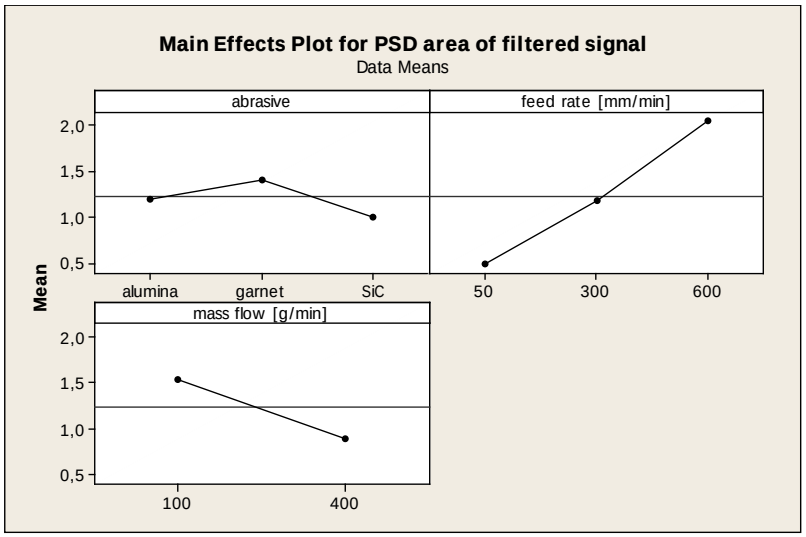

Figure 5.31: Filtered signal PSD area main effects plot

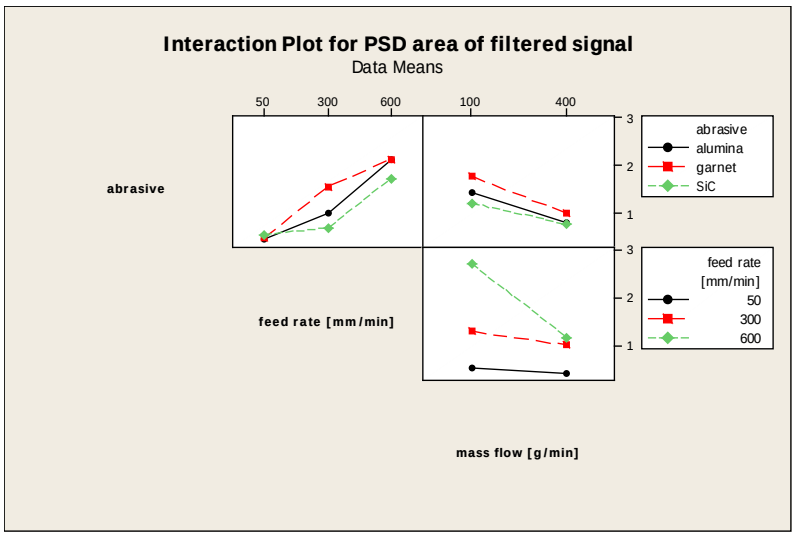

Figure 5.32: Filtered signal PSD area interaction plot

The behavior of RMS, PSD area and PSD peak value are equivalent. With a higher feed speed there seems to be a higher dispersion in data. The trend is clear with alumina and SiC, less with garnet. However, more data are needed for better results.
The electrical response measured is caused by a mechanical stress. For this reason, it can be said that a higher feed speed causes an increase in the workpiece stress state. The different values in RMS, PSD area and peak value due to feed speed are caused by a bigger jet area impinging on the piece or to an increase of the force acting on the workpiece, thus leading to an higher stress. A confirm can be found in two pure water jet cuts made after the experimental plan using a feed of 300 mm/min at a pressure of respectively 35000 PSI (240 MPa) and 15000 PSI (103 MPa). The first one managed to cut through the material and the calculated values of RMS and PSD area were 1,25 V and 1,55 V^2. The second cut did not pierce the material and removed just the superior layer. The value calculated for RMS and PSD area were in this case 2,47 V and 5,92 V^2, almost the double of all other cuts with a feed of 300 mm/min. **Figure 5.33** shows the two pure water jet cuts just described:

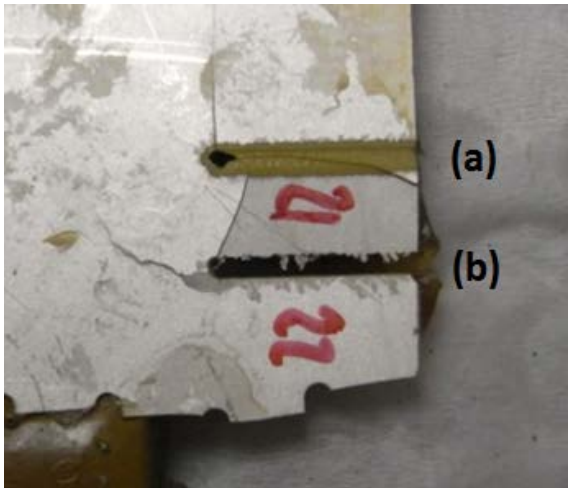

Figure 5.33: Unsuccessful cut (a) and successful cut (b) made with pure water. In cut (a) is possible to see the yellow PZT below the silver electrode

Using the values of RMS, PSD area or peak value as response, the existence of a relationship between the impacting area of the jet and the feed rate may be taken into account. However, if this relation exists, it is not linear since an increase of 6 times in feed from 50 to 300 mm/min just double the values of RMS, PSD area and PSD peak values. A possible way to test it could be to use an object with a known area, apply a known force and see if it could be related to the signal response in any way. Moreover, a research topic is the measurement of abrasive water jet cutting forces with load cells. If the forces

measured with these techniques are correct, it could be possible to obtain the impinging area by solving the piezoelectric equations.
With an increase in abrasive mass flow the RMS, PSD area and PSD peak values decrease; this can be cause by the fact that more abrasive leads to a faster material removal and a lesser portion of the jet impinges on the workpiece, thus causing a reduction in the measured values.

5.3.5 Filtered signal PSD peak frequency analysis

The last considered parameter is the frequency of the PSD peak. The block factor results not relevant. The feed rate is the only significant parameter. **Figure 5.34** and **Figure 5.35** show the main effect plot and the interaction plot. The full ANOVA table can be found in **Appendix B**, **Section B.5**, the entire list of calculated values for PSD peak frequency can be found in **Appendix A**.

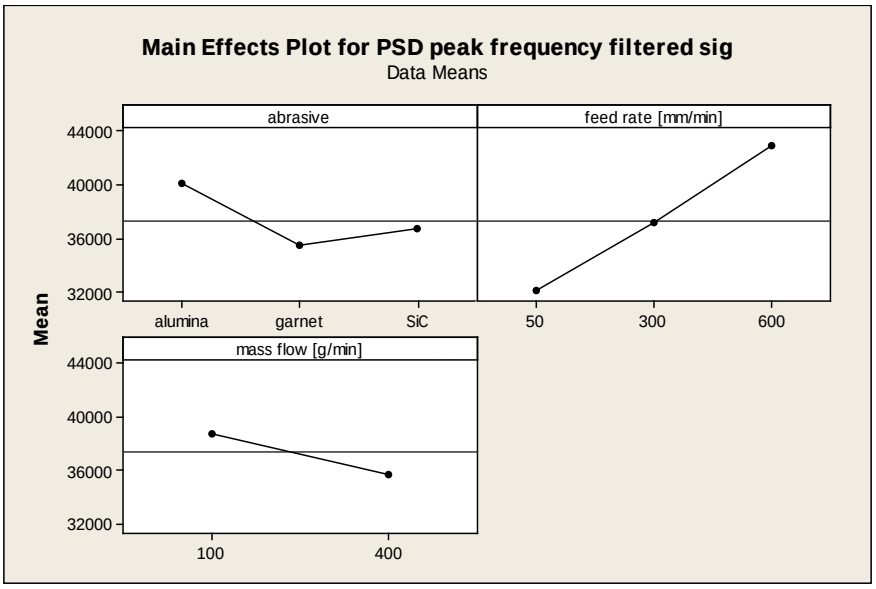

Figure 5.34: PSD peak frequency main effects plot

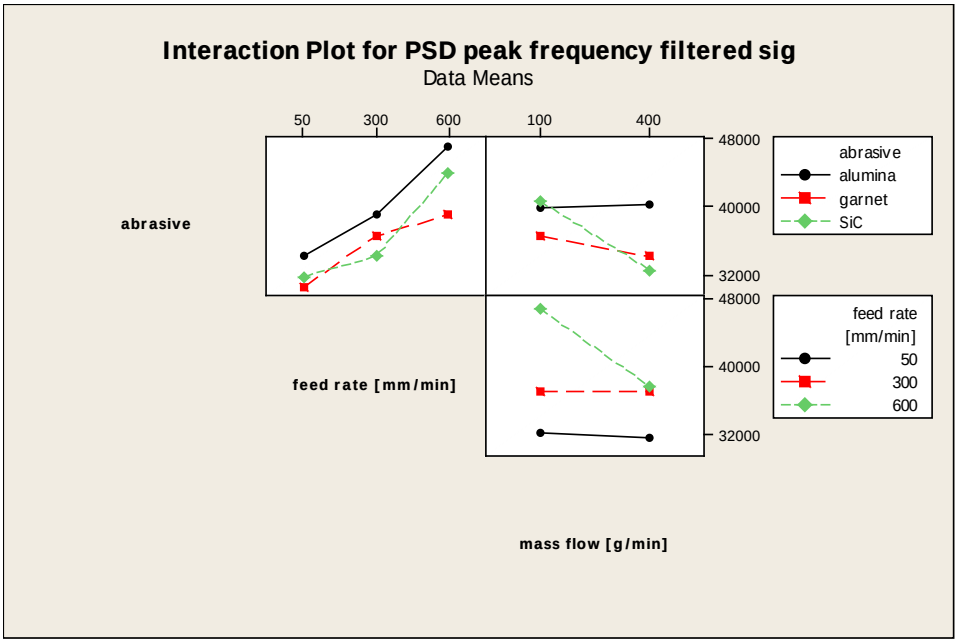

Figure 5.35: PSD peak frequency interaction plot

The feed speed is the only parameter that has an effect on the PSD peak frequency. The peak frequency is related to a mechanical action. It is not related to the number of abrasive particles hitting the workpiece as the mass flow is not relevant in the analysis. Probably, as the feed rate increases, a higher portion of the jet is involved in the cut and so there are more single droplets impacting the surface. The change in the number of impacting water drops can be the cause of the shift of the PSD peak frequency.

5.4 Discussion

With the number of applications suitable for advanced ceramics growing, water jet machining has the chance to become the leading cutting technology thanks to its high flexibility, its ability to avoid high mechanical stresses as well as thermal solicitations and the capability to successfully machine hard-to-cut materials such as piezoelectric ceramics. In particular, the Curie point represents a strong constrain in machining a piezoelectric material: exceeding this limit would result in a permanent loss of the ceramic piezoelectric properties. However, this work showed that not only water jet technology is capable of successful machining the PZT sheets without any particular issue, but also that is capable of maintaining the piezoelectric properties unaltered. Not exceeding the Curie point may represent an issue with thermal cut technologies such as plasma cutting or laser cutting.

5.4.1 Surface finish

The investigation on surface finish showed that an harder and sharper abrasive improves the results in terms of surface roughness (average R_a of 3.13 µm for garnet, of 2.93 µm for alumina and 2.67 µm for silicon carbide). Microcuts can be found on the surface and confirms the findings of [2][3][9]. In addition, the harder and sharper the abrasive, the more and deeper were the number of microcuts found on the surface. Microcuts are associated to a plastic flow of the ceramic. The material shows a ductile behavior because of the high hardness and sharpness of the abrasive. Further investigations may be needed to understand the influence of the microcuts on the material behavior and if their presence is acceptable. The use of a harder abrasive decreases the ratio H_t/H_p (the ratio between the hardness of the target material and the hardness of the abrasive particle), meaning that the hypothesis of infinite hard and rigid abrasive particles may be acceptable and models presented in [11] and [12] may be accurate. The machined surface is generated by integranular cracking and removal of entire grains of material caused by the erosion of the matrix, exposing the remaining grains kept together by the organic binder used in the manufacturing process (as describer also in [20]). Abrasive mass flow and feed rate play no role in the surface roughness analysis; this is probably due to the small thickness of the PZT sheet, namely 0.5 mm, and to the fact that the binder, which keeps the PZT grains together, is easier to machine, causing grains to fall apart. The custom fixturing system crated to sustain the PZT sheet has proven to work correctly as the influence of the rebounding jet on the machined kerf has been avoided by creating pre-made slits on the support and the chipping (the breaking of material on the exit side of the kerf) is not present, granting the uniformity and integrity of the surface (if the support is not rigid enough, the chipping occurs as shown in [20]).

5.4.2 Electric signal

The analysis of the signal parameters has given some interesting results which may be useful to deeply understand the machining process since the electrical signal generated by the workpiece is caused by the mechanical stress applied to it (the direct piezoelectric effect) by the water jet. An increase in the feed rate tends to increase the value of RMS, PSD peak value and PSD area, the increase in abrasive mass flow tends to decrease their value and the type of abrasive used in the cuts has no effect on their value. The abrasive effect could be masked by the effect of the water jet, as proved by the fact that the same parameters calculated in the case of a pure water jet cut (the first of the two pure water jet cuts described in **Section 5.3.4**) had the same values as the ones of a normal abrasive water jet cut. The variation in the values of RMS, PSD peak value and PSD area are related to a variation in the stress state of the workpiece: the higher those values, the higher the mechanical solicitation on the piece. The increase in these values, and consequently in mechanical stress, with an increase in feed rate is related to an increase of the impinging area of the jet on the workpiece or of the forces involved in the cut. **Figure 5.36** shows the change in the cutting front shape when varying the feed rate. As the jet moves faster, a bigger portion of the jet strikes the surface before the material actually break and stops generating the signal. In addition, increasing the cutting front area means that also the inner part of the jet get involved in the cutting process. The central part of the jet is more coherent and presents a higher water speed and these characteristic of the core of the jet may cause an increase in the stress state when such portion of jet hit the workpiece.

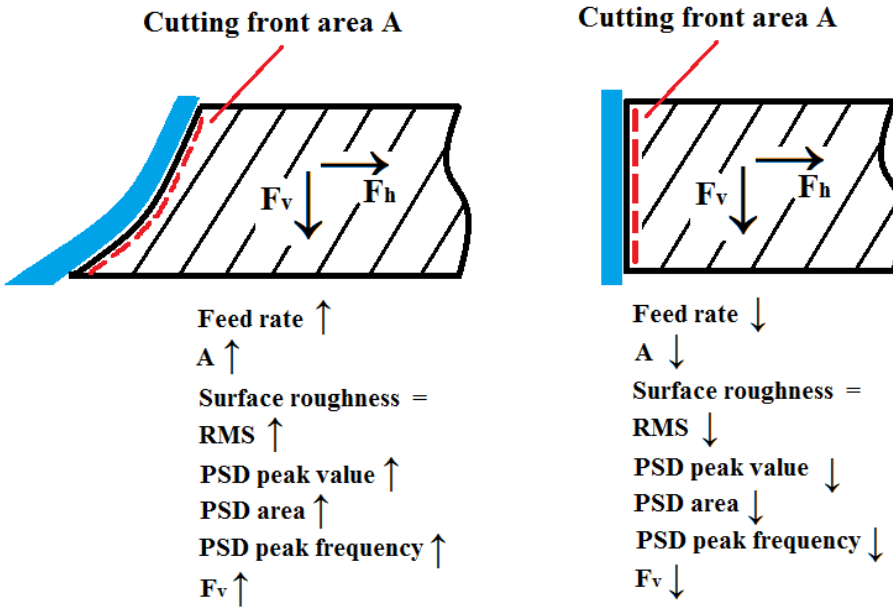

Figure 5.36: Effect of the feed rate on the parameters of interest

The decrease in RMS, PSD peak value and PSD area caused by an increase in abrasive mass flow is probably related to a more effective material removal when adding more abrasive to the water stream, thus reducing faster the impinging area of the jet and leading to inferior values of these parameters. A confirm of the previous conclusions can be found in a comparison between the signals acquired during two pure water jet cuts (see **Section 5.3.4**). The first cut, which successfully cut the workpiece, had values comparable to the ones of the cuts made in the experimental campaign. The second cut, made at half the pressure employed in the other tests, just machined the surface of the PZT sheet without piercing it and the values measured in this case were the double of the ones calculated in the same condition. In fact, a jet machining the surface without piercing the material generates a force on the workpiece higher than when piercing the material because of the conser

The PSD peak frequency indicates at which frequency most of the energy of the signal is present, meaning that there is a mechanical event happening at that specific frequency. The PSD peak frequency value is influenced only by the variation of feed rate, where an increase in feed rate cause an increase of the PSD peak frequency. The PSD peak frequency does not represents the frequency of impact of the abrasive particles since the changes in abrasive mass flow have no influence. It is probably related to a phenomenon in the water jet, possibly the increase in number of single water droplets impacting the workpiece surface. This seems to be coherent with an increase of the jet area involved in the cut suggested by the analysis on RMS, PSD area and PSD peak value. **Figure 5.36** list the effect of the feed rate on the parameters of interest.

Many efforts are put in the study of the jet as a tool. The behavior of the acquired signal is caused by the jet itself and, for this reason, the results obtained in this work are not limited to ceramic materials and may be useful for further investigations regarding the forces and areas involved in water jet cutting process in general.

Chapter 6

Conclusions

The present work has come to the following conclusions:

- PZT can be successfully machined using abrasive water jet.
- The piezoelectric properties of the material are maintained.
- The surface roughness R_a is influenced only by the type of abrasive used in the cuts. The value of R_a decrease when using a harder and sharper abrasive (garnet generates the higher value of R_a, silicon carbide the lower).
- The surface is generated mainly by intergranular cracking.
- Microcuts, that testify the plastic flow of the material, can be found on the surface. Their number and depth increases with the increase of abrasive hardness and sharpness.
- Chipping on the inferior edge of the kerf is not present thanks to a rigid fixturing system.
- Signal RMS, PSD peak value and PSD area are influenced by the abrasive mass flow and by the feed rate. An increase in feed rate causes an increase in the calculated values, an increase in abrasive mass flow causes a decrease in the values.
- Signal PSD peak frequency is influenced only by the feed rate. An increase in feed rate causes an increase in the observed values.
- The increase in signal RMS, PSD peak value and PSD area are related to an increase in the workpiece stress state due to an higher cutting front or cutting force.
- The increase in PSD peak frequency is probably related to an higher number of single droplets of water hitting the workpiece.

A. Experimental Results

A.1 List of experiments

Table A.1: List of preliminary cuts

PRELIMINARY CUTS				
Cut name	**Run order**	**Abrasive**	**feed rate [mm/min]**	**mass flow [g/min]**
garnet 1	1	garnet	10	80
garnet 2	2	garnet	300	80
garnet 3	3	garnet	300	80
garnet 4	4	garnet	70	80
garnet 5	5	garnet	70	80
garnet 6	6	garnet	70	20
garnet 7	7	garnet	70	200
pure water	8	none	70	0

Table A.2: List of DOE experimental plan cuts

DOE EXPERIMENTAL PLAN					
Cut name	**Run order**	**Sheet**	**abrasive**	**feed rate [mm/min]**	**mass flow [g/min]**
garnet 1	1	1	garnet	600	400
garnet 2	2	1	garnet	300	400
garnet 3	3	1	garnet	300	100
garnet 4	4	1	garnet	50	100
garnet 5	5	1	garnet	600	100
garnet 6	6	1	garnet	50	400
alumina 1	7	1	alumina	50	100
alumina 2	8	1	alumina	600	100
alumina 3	9	1	alumina	600	400
alumina 4	10	1	alumina	300	400
alumina 5	11	1	alumina	300	100
alumina 6	12	1	alumina	50	400
garnet 7	13	2	garnet	300	400
garnet 8	14	2	garnet	50	400
garnet 9	15	2	garnet	600	100
garnet 10	16	2	garnet	300	100
garnet 11	17	2	garnet	50	100
garnet 12	18	2	garnet	600	400
alumina 7	19	2	alumina	600	100
alumina 8	20	2	alumina	50	100
alumina 9	21	2	alumina	300	100
alumina 10	22	2	alumina	300	400
alumina 11	23	2	alumina	600	400
alumina 12	24	2	alumina	50	400
SiC 1	25	2	SiC	300	100
SiC 2	26	2	SiC	600	400
SiC 3	27	2	SiC	50	100
SiC 4	28	2	SiC	600	100
SiC 5	29	2	SiC	300	400
SiC 6	30	2	SiC	50	400
SiC 7	31	1	SiC	50	400
SiC 8	32	1	SiC	300	100
SiC 9	33	1	SiC	300	400
SiC 10	34	1	SiC	50	100
SiC 11	35	1	SiC	600	400
SiC 12	36	1	SiC	600	100

A.2 Roughness measures

Table A.3: Measured R_a of preliminary cuts

PRELIMINARY CUTS		
Cut name	**Run order**	**R_a [µm]**
garnet 1	1	4.47
garnet 2	2	4.24
garnet 3	3	3.38
garnet 4	4	4.78
garnet 5	5	4.71
garnet 6	6	4.83
garnet 7	7	5.06
pure water	8	3.81

Table A.4: Measured R_a of DOE experimental plan

DOE EXPERIMENTAL PLAN		
Cut name	**Run order**	**R_a [µm]**
garnet 1	1	2.43
garnet 2	2	2.8
garnet 3	3	3.2
garnet 4	4	3.38
garnet 5	5	3.16
garnet 6	6	3.95
alumina 1	7	2.85
alumina 2	8	3.72
alumina 3	9	3.31
alumina 4	10	2.64
alumina 5	11	2.29
alumina 6	12	2.95
garnet 7	13	3.05
garnet 8	14	2.65
garnet 9	15	3.31
garnet 10	16	3.32
garnet 11	17	3.64
garnet 12	18	2.67
alumina 7	19	3.04
alumina 8	20	2.82
alumina 9	21	2.60
alumina 10	22	3.10
alumina 11	23	4.88
alumina 12	24	7.35
SiC 1	25	2.69
SiC 2	26	3.12
SiC 3	27	2.66
SiC 4	28	3.24
SiC 5	29	3.08
SiC 6	30	2.76
SiC 7	31	2.50
SiC 8	32	2.21
SiC 9	33	2.57
SiC 10	34	2.21
SiC 11	35	2.68
SiC 12	36	2.38

A.3 Signal data

Table A.5: Signal data of preliminary cuts

PRELIMINARY CUTS						
Cut name	**Run order**	**Noise RMS [27]**	**Signal RMS [27]**	**PSD peak value [V^2/Hz]**	**PSD peak frequency [Hz]**	**PSD area [V^2]**
garnet 1	1	---	---	---	---	---
garnet 2	2	4.10E-01	1.14E+00	2.25E-05	3.42E+04	1.29E+00
garnet 3	3	4.26E-01	1.14E+00	2.22E-05	3.91E+04	1.29E+00
garnet 4	4	4.47E-01	8.27E-01	1.56E-05	3.91E+04	6.78E-01
garnet 5	5	4.24E-01	7.86E-01	1.24E-05	2.93E+04	6.11E-01
garnet 6	6	4.28E-01	6.37E-01	7.13E-06	2.93E+04	4.00E-01
garnet 7	7	4.51E-01	7.32E-01	1.06E-05	2.93E+04	5.30E-01
pure water	8	4.33E-01	7.37E-01	7.94E-06	4.88E+04	5.33E-01

Table A.6: Signal data of DOE experimental plan

DOE EXPERIMENTAL PLAN						
Cut name	**Run order**	**Noise RMS [27]**	**Signal RMS [27]**	**PSD peak value [V^2/Hz]**	**PSD peak frequency [Hz]**	**PSD area [V^2]**
garnet 1	1	6.10E-01	1.24E+00	3.61E-05	3.42E+04	1.53E+00
garnet 2	2	5.11E-01	1.18E+00	3.15E-05	3.42E+04	1.39E+00
garnet 3	3	7.17E-01	1.52E+00	4.42E-05	3.91E+04	2.29E+00
garnet 4	4	6.46E-01	7.61E-01	1.52E-05	2.93E+04	5.75E-01
garnet 5	5	5.57E-01	1.86E+00	7.25E-05	5.37E+04	3.42E+00
garnet 6	6	5.46E-01	6.80E-01	1.13E-05	2.93E+04	4.57E-01
alumina 1	7	5.67E-01	7.97E-01	1.68E-05	3.42E+04	6.31E-01
alumina 2	8	5.32E-01	1.91E+00	6.04E-05	4.88E+04	3.63E+00
alumina 3	9	5.53E-01	1.09E+00	1.94E-05	4.88E+04	1.18E+00
alumina 4	10	5.35E-01	8.61E-01	1.43E-05	3.91E+04	7.34E-01
alumina 5	11	5.30E-01	8.84E-01	1.52E-05	3.91E+04	7.75E-01
alumina 6	12	5.19E-01	6.62E-01	1.01E-05	3.42E+04	4.35E-01
garnet 7	13	8.19E-02	1.10E+00	2.98E-05	3.91E+04	1.20E+00
garnet 8	14	3.55E-01	7.51E-01	1.68E-05	3.42E+04	5.61E-01
garnet 9	15	3.71E-01	1.66E+00	5.21E-05	3.42E+04	2.72E+00
garnet 10	16	4.07E-01	1.17E+00	2.88E-05	3.42E+04	1.36E+00
garnet 11	17	3.88E-01	5.75E-01	9.46E-06	2.93E+04	3.28E-01
garnet 12	18	3.72E-01	9.45E-01	1.73E-05	3.42E+04	8.84E-01
alumina 7	19	7.70E-02	1.27E+00	3.05E-05	4.39E+04	1.59E+00
alumina 8	20	8.04E-02	5.77E-01	8.17E-06	3.42E+04	3.30E-01
alumina 9	21	7.78E-02	1.28E+00	4.00E-05	3.91E+04	1.63E+00
alumina 10	22	1.30E-01	9.58E-01	1.88E-05	3.91E+04	9.16E-01
alumina 11	23	8.09E-02	3.07E+00	2.24E-04	4.39E+04	9.35E+00
alumina 12	24	8.26E-02	1.75E+00	7.17E-05	4.39E+04	3.03E+00
SiC 1	25	8.44E-02	7.11E-01	1.11E-05	3.42E+04	5.02E-01
SiC 2	26	8.33E-02	1.07E+00	2.08E-05	3.42E+04	1.15E+00
SiC 3	27	8.68E-02	9.16E-01	2.16E-05	3.42E+04	8.35E-01
SiC 4	28	8.27E-02	1.53E+00	4.78E-05	5.37E+04	2.32E+00
SiC 5	29	7.79E-02	9.59E-01	2.08E-05	3.42E+04	9.14E-01
SiC 6	30	7.74E-02	5.28E-01	6.22E-06	2.93E+04	2.76E-01

B. Statistical Analysis

Analysis of variance (ANOVA) has been used to analyze the data. A blocking approach has been applied to the factor “PZT sheet” to check its relevance in the experimentation. For this reason, there are no statistical replicates and the model cannot include the triple interaction as it would results in no degrees of freedom for the error. Since there are no replicates, the test for equal variances cannot be performed. Data from cuts “alumina 11” and “alumina 12” has been discarded since there have been issues related to the abrasive feeding during the cut and the values are not acceptable both for roughness and signal analysis. As this is an explorative campaign and the number of experiments is limited, a fixed value of $\alpha = 5\%$ has been used without the Bonferroni correction. α is the significance level of a test and it is a threshold value used to judge whether a factor is statistically significant. If the p-value of a parameter is less than α, that factor has an effect on the response.

B.1 Surface roughness

The used model includes the factors feed rate, abrasive mass flow and abrasive type and their second degree interactions. The sheet factor is used as block and it must be included in the model only as additive factor. Before analyzing the data, it is useful to look at the main effect plot (**Figure B.1**) and interaction plot (**Figure B.2**). The abrasive type seems influent, feed rate and abrasive mass flow seems not to be relevant. The type of abrasive seems to have no influence. An abrasive type – feed rate interaction may be present.

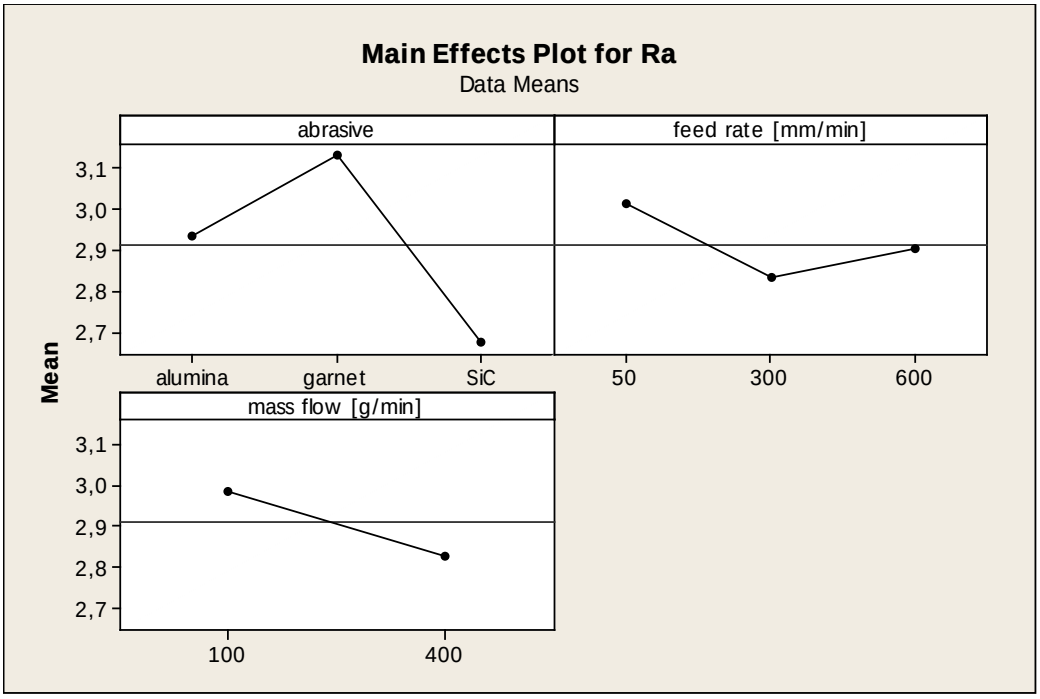

Figure B.1: Main effect plot of R_a

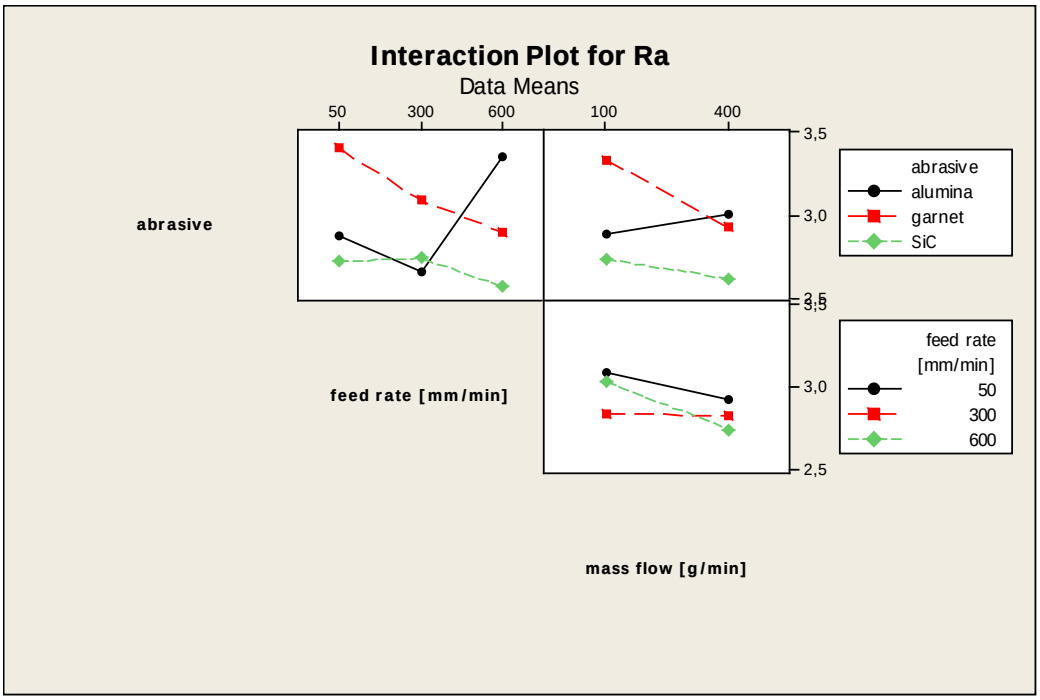

Figure B.2: Interaction plot of R_a

The ANOVA table is the following:

General Linear Model: Ra versus Sheet; abrasive; ...

```
Factor              Type   Levels  Values
Sheet               fixed       2  1; 2
abrasive            fixed       3  alumina; garnet; SiC
feed rate [mm/min]  fixed       3  50; 300; 600
mass flow [g/min]   fixed       2  100; 400


Analysis of Variance for Ra. using Adjusted SS for Tests

Source                                  DF  Seq SS  Adj SS  Adj MS     F      P
Sheet                                    1  0.3948  0.2917  0.2917  2.34  0.143
abrasive                                 2  1.2426  1.2561  0.6280  5.04  0.018
feed rate [mm/min]                       2  0.1731  0.1528  0.0764  0.61  0.552
mass flow [g/min]                        1  0.2309  0.1459  0.1459  1.17  0.293
abrasive*feed rate [mm/min]              4  1.1739  1.1987  0.2997  2.40  0.086
abrasive*mass flow [g/min]               2  0.4012  0.3745  0.1873  1.50  0.248
feed rate [mm/min]*mass flow [g/min]     2  0.0598  0.0598  0.0299  0.24  0.789
Error                                   19  2.3696  2.3696  0.1247
Total                                   33  6.0460


S = 0.353153   R-Sq = 60.81%   R-Sq(adj) = 31.93%
```

The ANOVA shows that only the abrasive type is significant as its p-value is lower than the α value set to 5%. With a p-value of 0.143, the block results not relevant and results are not influenced by a change in material sheet. It is necessary to verify the statistical hypothesis of ANOVA: the test of normality of the residuals (**Figure B.3**) and the independence of the residuals (**Figure B.4**). The test of equal variances cannot be performed as there are no replicates.

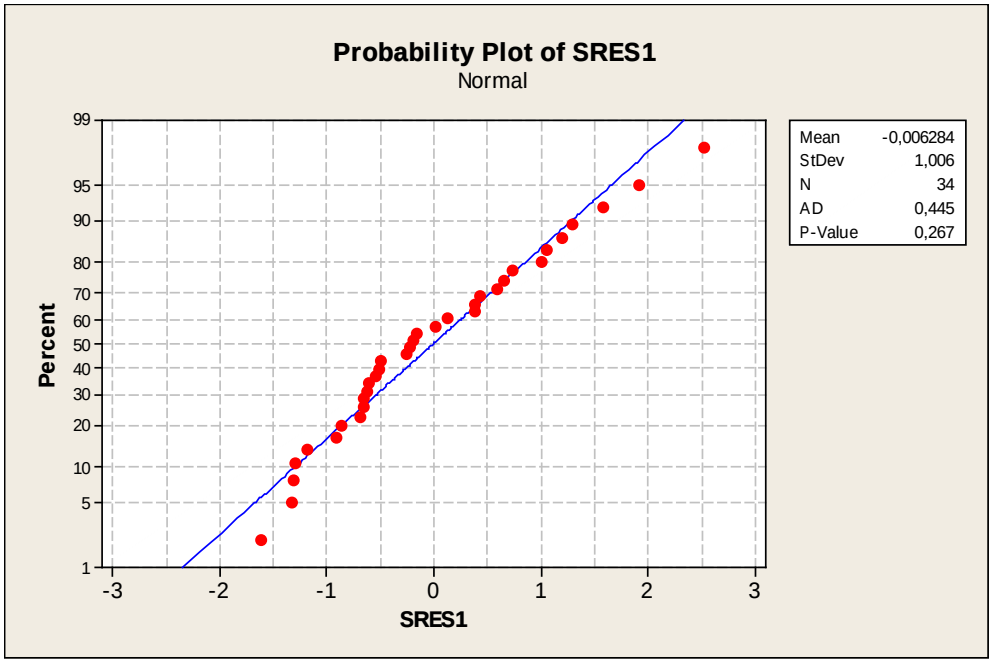

Figure B.3: R_a residuals normality test

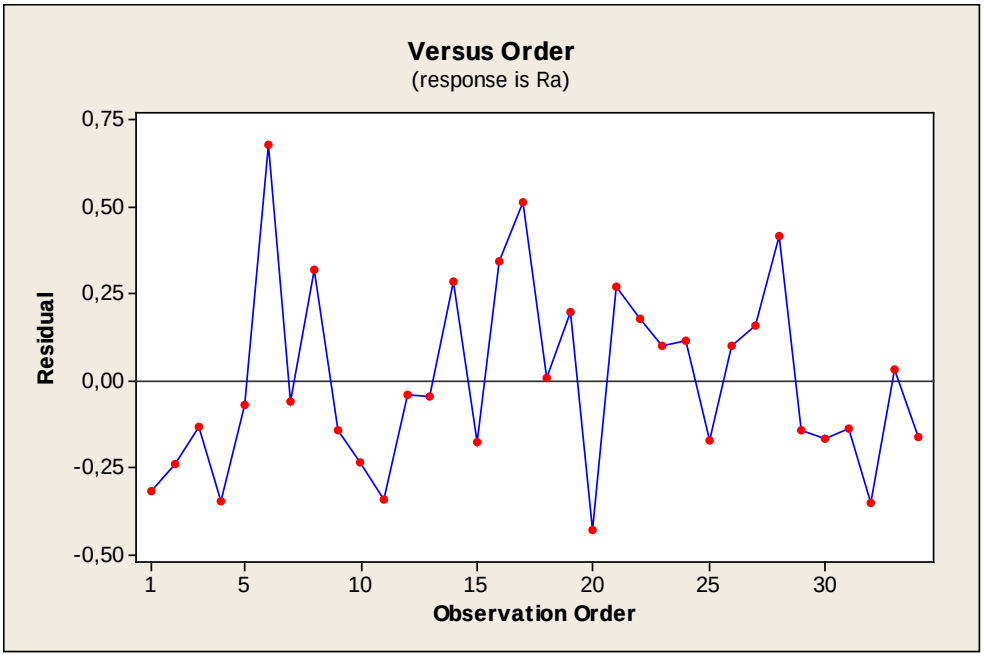

Figure B. 4: R_a Standardized residuals vs Run order graph

Residuals are normal since the p-value is higher than 0.05 and independent since the graph Standardized residuals vs Run order shows no specific trends. The ANOVA results are acceptable.

B.2 Filtered signal RMS

The used model includes the factors feed rate, abrasive mass flow and abrasive type and their second degree interactions. The sheet factor is used as block and it must be included in the model only as additive factor.

Before analyzing the data, it is useful to look at the main effect plot (**Figure B.5**) and interaction plot (**Figure B.6**). It is evident the effect of the feed rate and mass flow. The type of abrasive seems to have no influence. A feed rate – mass flow interaction may be present.

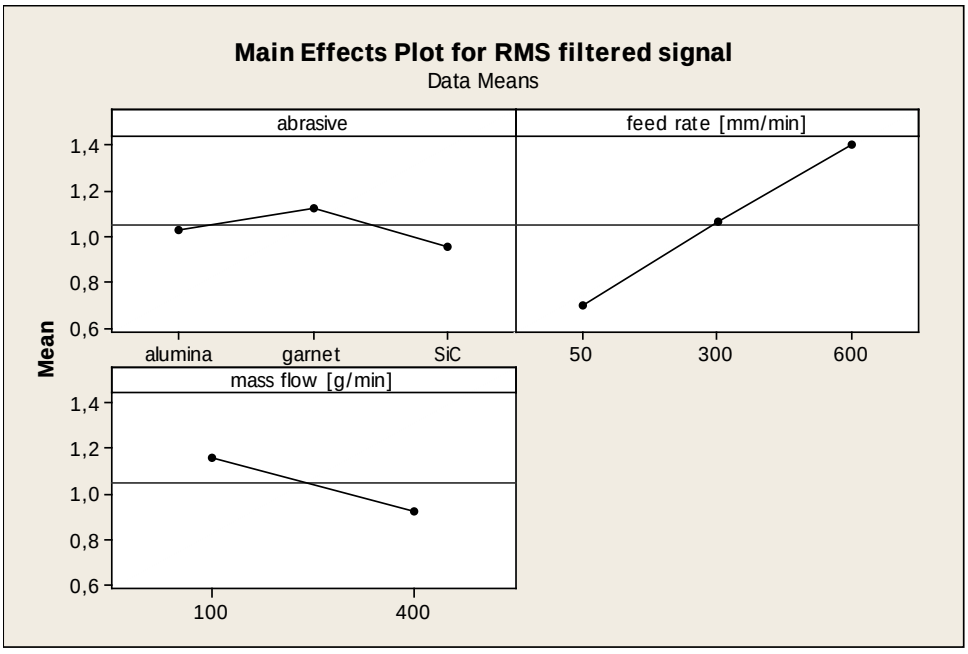

Figure B.5: Main effect plot of filtered signal RMS

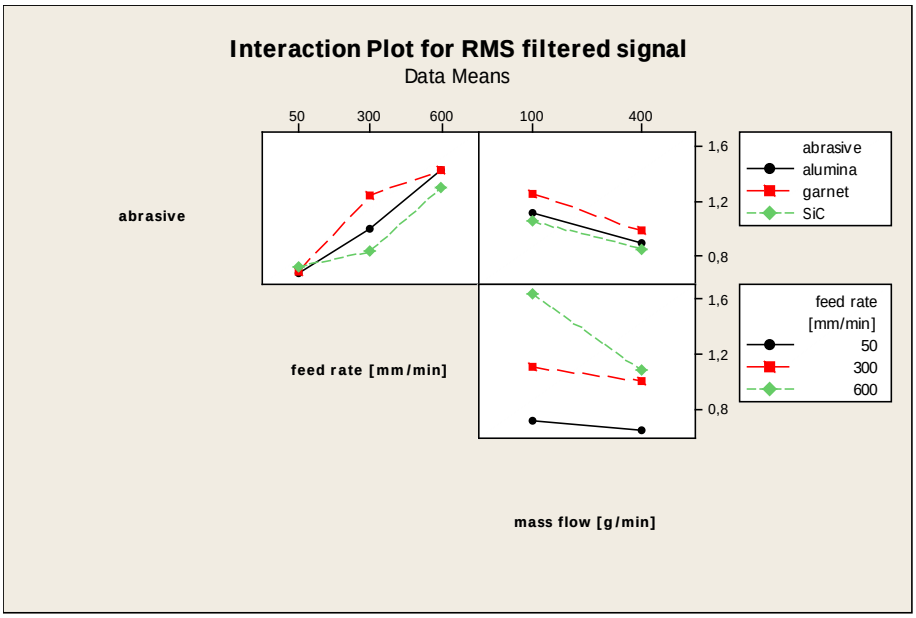

Figure B.6: Interaction plot of filtered signal RMS

The ANOVA table is the following:

General Linear Model: RMS filtered signal versus Sheet; abrasive; ...

```
Factor              Type   Levels  Values
Sheet               fixed       2  1; 2
abrasive            fixed       3  alumina; garnet; SiC
feed rate [mm/min]  fixed       3  50; 300; 600
mass flow [g/min]   fixed       2  100; 400


Analysis of Variance for RMS filtered signal, using Adjusted SS for Tests

Source                                DF   Seq SS   Adj SS   Adj MS      F
Sheet                                  1  0.10098  0.10973  0.10973   2.80
abrasive                               2  0.07595  0.11278  0.05639   1.44
feed rate [mm/min]                     2  2.23732  1.79102  0.89551  22.86
mass flow [g/min]                      1  0.44281  0.39910  0.39910  10.19
abrasive*feed rate [mm/min]            4  0.13999  0.13342  0.03336   0.85
abrasive*mass flow [g/min]             2  0.00561  0.00763  0.00381   0.10
feed rate [mm/min]*mass flow [g/min]   2  0.35279  0.35279  0.17640   4.50
Error                                 13  0.50924  0.50924  0.03917
Total                                 27  3.86469

Source                                    P
Sheet                                 0.118
abrasive                              0.272
feed rate [mm/min]                    0.000
mass flow [g/min]                     0.007
abrasive*feed rate [mm/min]           0.518
abrasive*mass flow [g/min]            0.908
feed rate [mm/min]*mass flow [g/min]  0.033
Error
Total
S = 0.197919   R-Sq = 86.82%   R-Sq(adj) = 72.63%
```

The ANOVA shows that feed rate, mass flow and the interaction feed rate – abrasive mass flow are significant as their p-value is lower than the α value set to 5%. With a p-value of 0.118, the block results not relevant and results are not influenced by a change in material sheet. It is necessary to verify the statistical hypothesis of ANOVA: the test of normality of the residuals (**Figure B.7**) and the independence of the residuals (**Figure B.8**). The test of equal variances cannot be performed as there are no replicates.

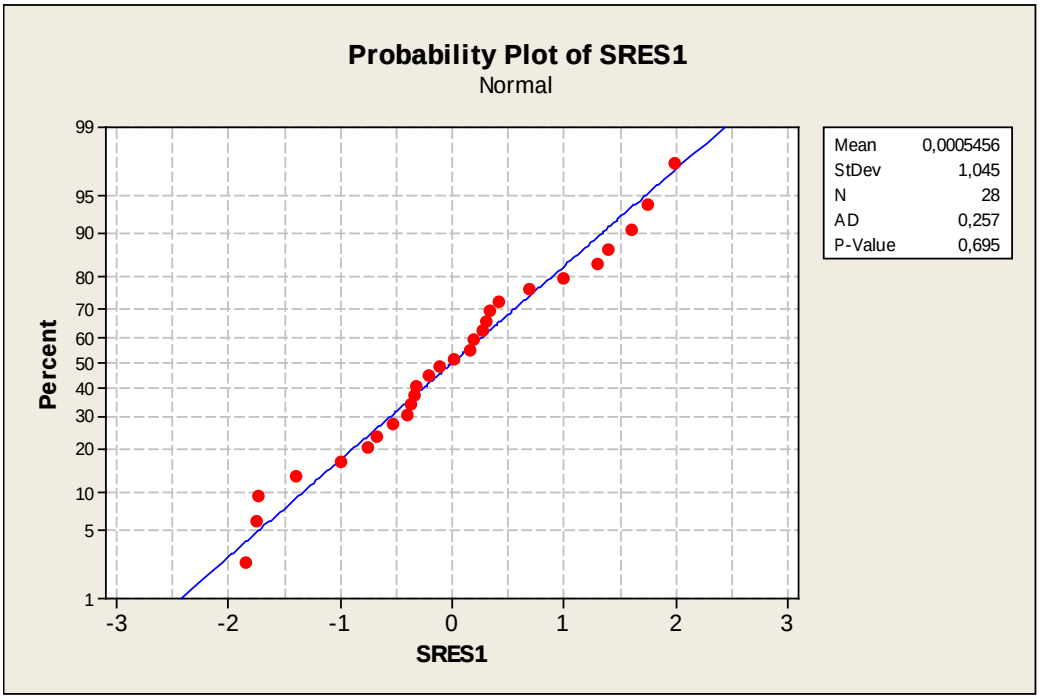

Figure B.7: Filtered signal RMS residuals normality test

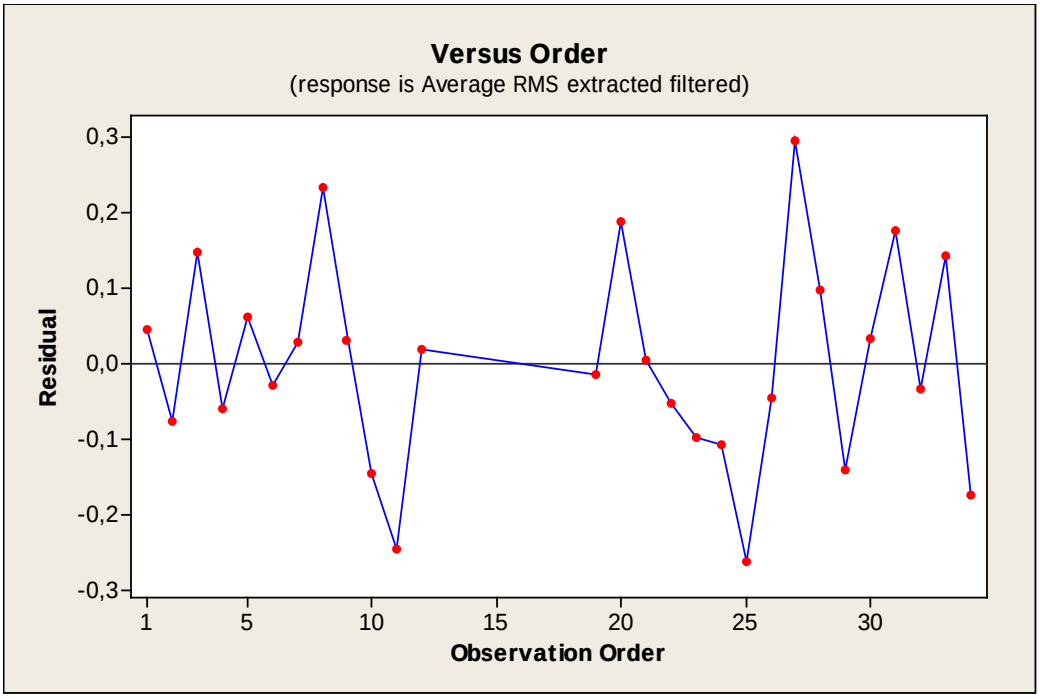

Figure B. 8: Filtered signal RMS Standardized residuals vs Run order graph

Residuals are normal since the p-value is higher than 0.05 and independent since the graph Standardized residuals vs Run order shows no specific trends. The ANOVA results are acceptable.

B.3 Filtered signal PSD peak

The used model includes the factors feed rate, abrasive mass flow and abrasive type and their second degree interactions. The sheet factor is used as block and it must be included in the model only as additive factor.

Before analyzing the data, it is useful to look at the main effect plot (**Figure B.9**) and interaction plot (**Figure B.10**). It is evident the effect of the feed rate and mass flow. The type of abrasive seems to have no influence. A feed rate – mass flow interaction may be present.

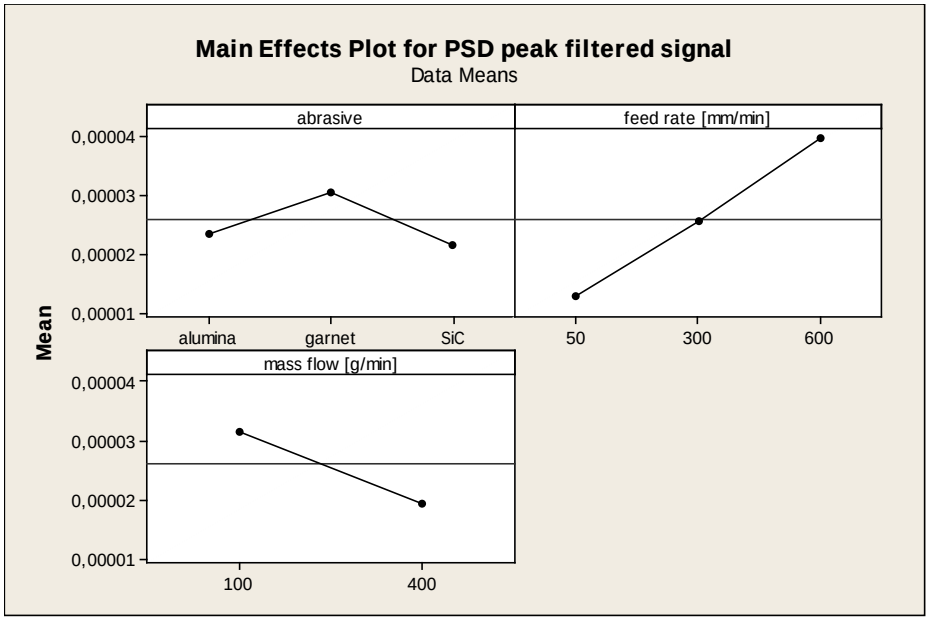

Figure B.9: Main effect plot of filtered signal PSD peak

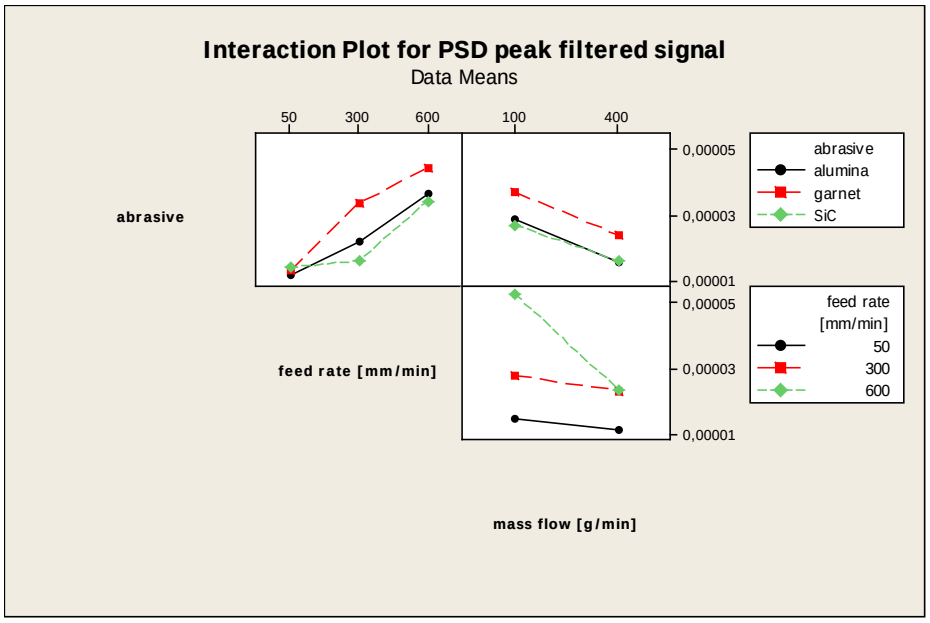

Figure B.10: Interaction plot of filtered signal PSD peak

The ANOVA table is the following:

General Linear Model: PSD peak filtered signal versus Sheet; abrasive; ...

```
Factor              Type   Levels  Values
Sheet               fixed       2  1; 2
abrasive            fixed       3  alumina; garnet; SiC
feed rate [mm/min]  fixed       3  50; 300; 600
```

```
mass flow [g/min]   fixed       2  100; 400


Analysis of Variance for PSD peak filtered signal, using Adjusted SS for Tests

Source                                DF     Seq SS     Adj SS     Adj MS
Sheet                                  1  0.0000000  0.0000000  0.0000000
abrasive                               2  0.0000000  0.0000000  0.0000000
feed rate [mm/min]                     2  0.0000000  0.0000000  0.0000000
mass flow [g/min]                      1  0.0000000  0.0000000  0.0000000
abrasive*feed rate [mm/min]            4  0.0000000  0.0000000  0.0000000
abrasive*mass flow [g/min]             2  0.0000000  0.0000000  0.0000000
feed rate [mm/min]*mass flow [g/min]   2  0.0000000  0.0000000  0.0000000
Error                                 13  0.0000000  0.0000000  0.0000000
Total                                 27  0.0000000

Source                                    F      P
Sheet                                  2.35  0.149
abrasive                               2.48  0.122
feed rate [mm/min]                    11.29  0.001
mass flow [g/min]                     10.58  0.006
abrasive*feed rate [mm/min]            0.67  0.623
abrasive*mass flow [g/min]             0.13  0.882
feed rate [mm/min]*mass flow [g/min]   5.17  0.022
Error
Total


S = 0.0000102709   R-Sq = 82.10%   R-Sq(adj) = 62.83%
```

The ANOVA shows that feed rate, mass flow and the interaction feed rate – abrasive mass flow are significant as their p-value is lower than the α value set to 5%. With a p-value of 0.149, the block results not relevant and results are not influenced by a change in material sheet. It is necessary to verify the statistical hypothesis of ANOVA: the test of normality of the residuals (**Figure B.11**) and the independence of the residuals (**Figure B.12**). The test of equal variances cannot be performed as there are no replicates.

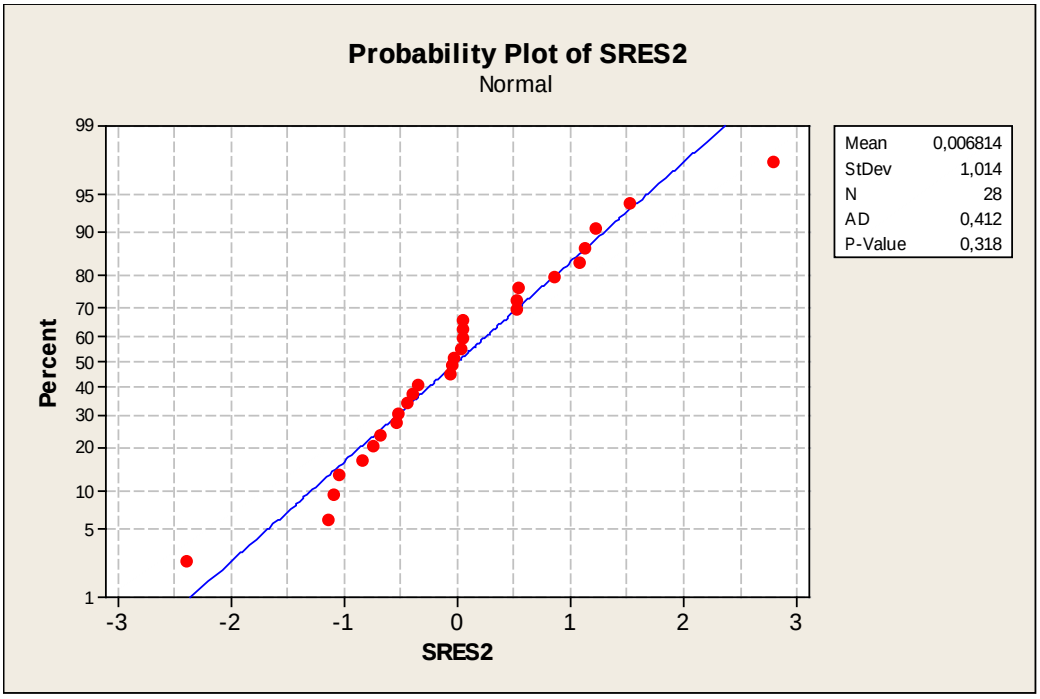

Figure B.11: Filtered signal PSD peak residuals normality test

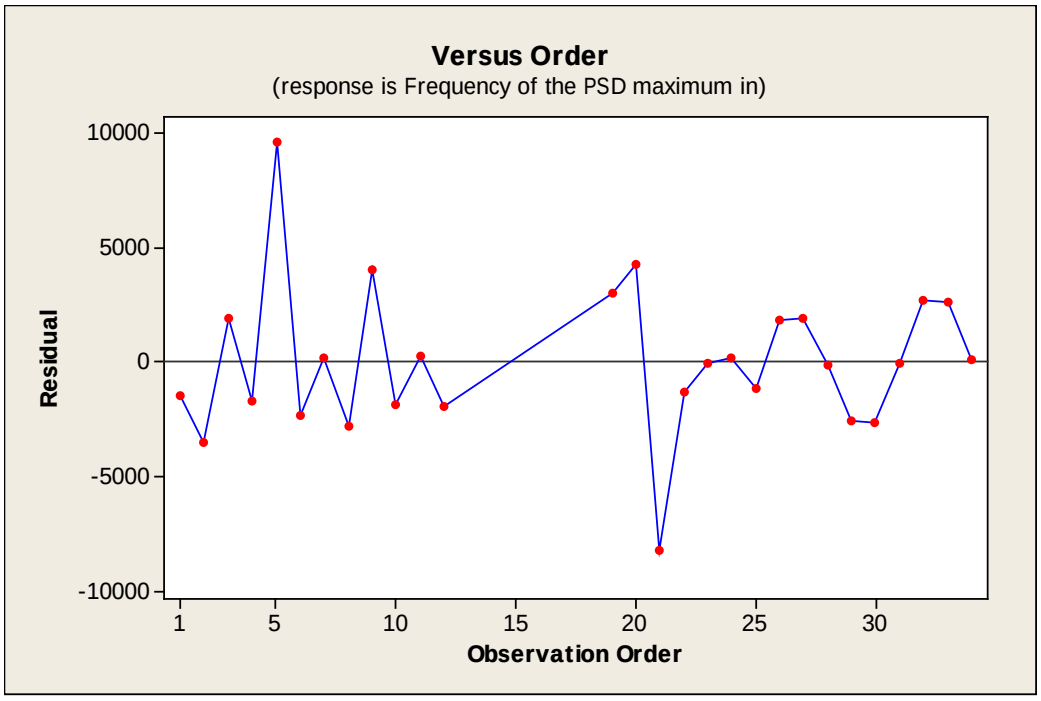

Figure B.12: Filtered signal PSD peak Standardized residuals vs Run order graph

Residuals are normal since the p-value is higher than 0.05 and independent since the graph Standardized residuals vs Run order shows no specific trends. The ANOVA results are acceptable.

B.4 Filtered signal PSD area

The used model includes the factors feed rate, abrasive mass flow and abrasive type and their second degree interactions. The sheet factor is used as block and it must be included in the model only as additive factor.

Before analyzing the data, it is useful to look at the main effect plot (**Figure B.13**) and interaction plot (**Figure B.14**). It is evident the effect of the feed rate and mass flow. The type of abrasive seems to have no influence. A feed rate – mass flow interaction may be present.

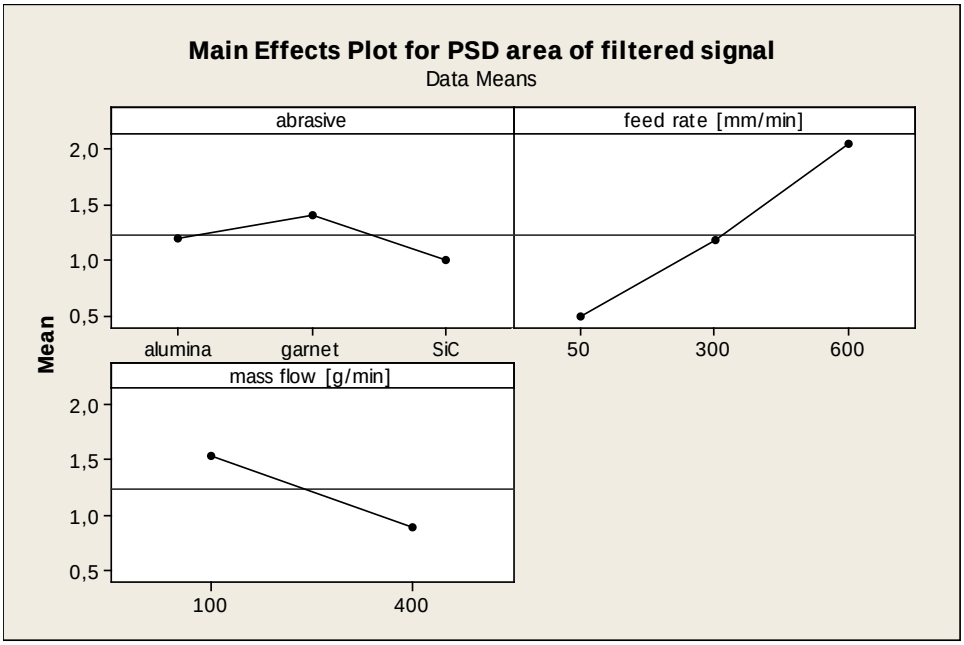

Figure B.13: Main effect plot of filtered signal PSD area

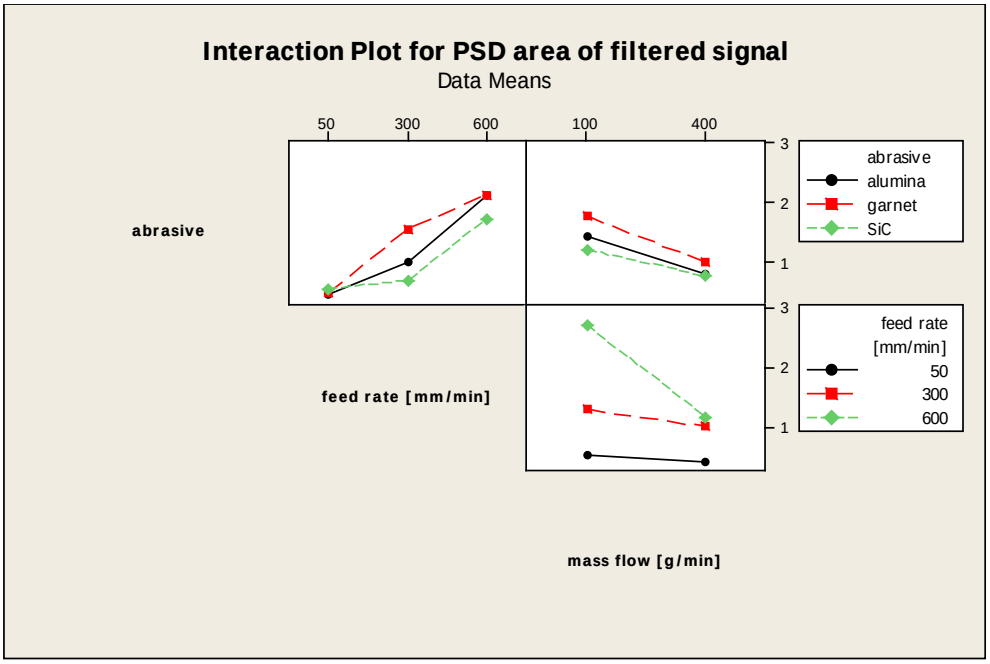

Figure B.14: Interaction plot of filtered signal PSD area

The ANOVA table is the following:

General Linear Model: PSD area of filt versus Sheet; abrasive; ...

```
Factor              Type   Levels  Values
Sheet               fixed       2  1; 2
abrasive            fixed       3  alumina; garnet; SiC
feed rate [mm/min]  fixed       3  50; 300; 600
mass flow [g/min]   fixed       2  100; 400


Analysis of Variance for PSD area of filtered signal, using Adjusted SS for
     Tests

Source                                DF   Seq SS  Adj SS  Adj MS      F      P
Sheet                                  1   0.7282  0.7942  0.7942   3.28  0.093
abrasive                               2   0.3941  0.6139  0.3070   1.27  0.314
feed rate [mm/min]                     2  10.9202  8.3224  4.1612  17.17  0.000
mass flow [g/min]                      1   3.1309  2.6883  2.6883  11.09  0.005
abrasive*feed rate [mm/min]            4   0.6294  0.5886  0.1472   0.61  0.665
abrasive*mass flow [g/min]             2   0.1156  0.1273  0.0637   0.26  0.773
feed rate [mm/min]*mass flow [g/min]   2   2.9122  2.9122  1.4561   6.01  0.014
Error                                 13   3.1505  3.1505  0.2423
Total                                 27  21.9812


S = 0.492290   R-Sq = 85.67%   R-Sq(adj) = 70.23%
```

The ANOVA shows that feed rate, mass flow and the interaction feed rate – abrasive mass flow are significant as their p-value is lower than the α value set to 5%. With a p-value of 0.093, the block results not relevant and results are not influenced by a change in material sheet. It is necessary to verify the statistical

hypothesis of ANOVA: the test of normality of the residuals (**Figure B.15**) and the independence of the residuals (**Figure B.16**). The test of equal variances cannot be performed as there are no replicates.

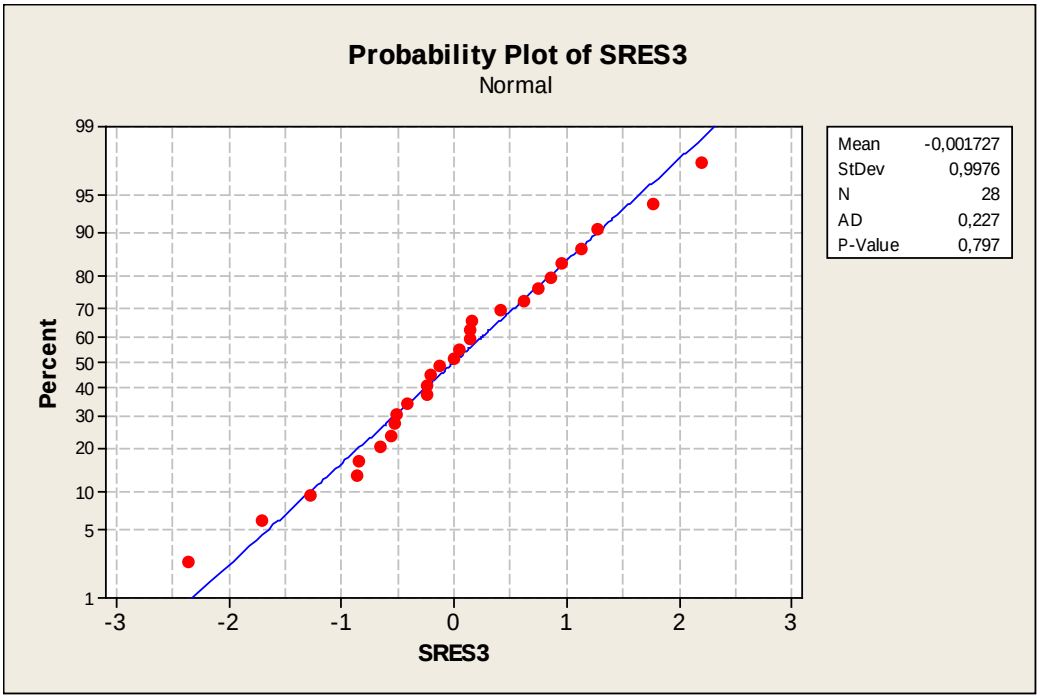

Figure B.15: Filtered signal PSD area residuals normality test

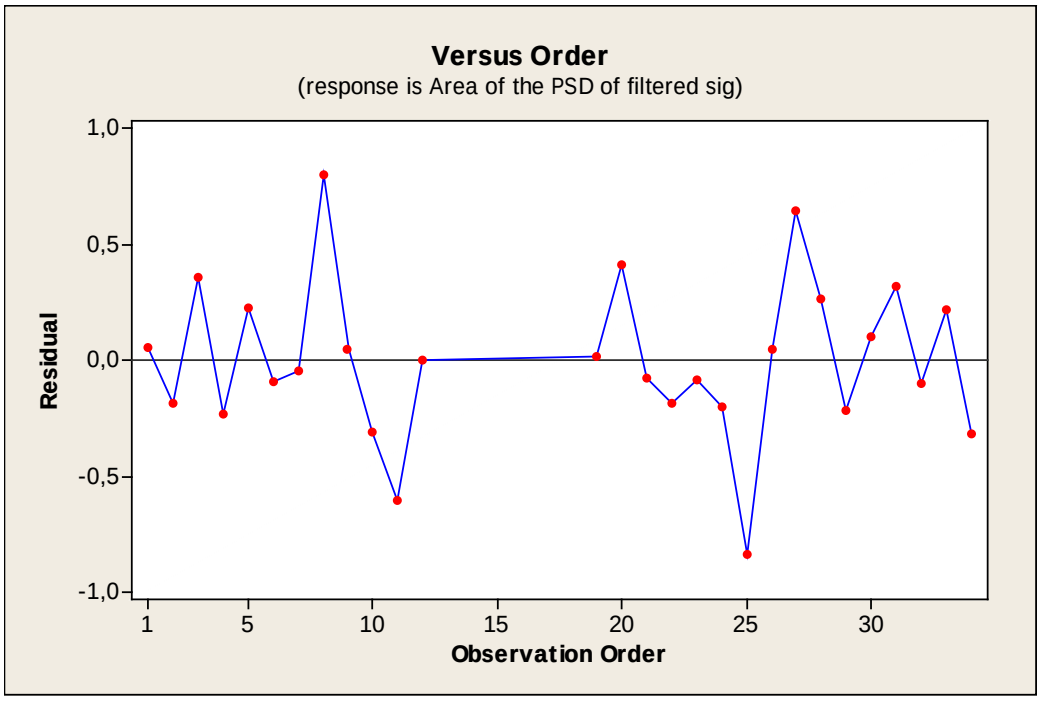

Figure B.16: Filtered signal PSD area Standardized residuals vs Run order graph

Residuals are normal since the p-value is higher than 0.05 and independent since the graph Standardized residuals vs Run order shows no specific trends. The ANOVA results are acceptable.

B.5 Filtered signal PSD peak frequency

The used model includes the factors feed rate, abrasive mass flow and abrasive type and their second degree interactions. The sheet factor is used as block and it must be included in the model only as additive factor.

Before analyzing the data, it is useful to look at the main effect plot (**Figure B.17**) and interaction plot (**Figure B.18**). It is evident the effect of the feed rate. The effect of abrasive mass flow and abrasive seems less evident and need a confirm by the ANOVA. The three interaction may be present.

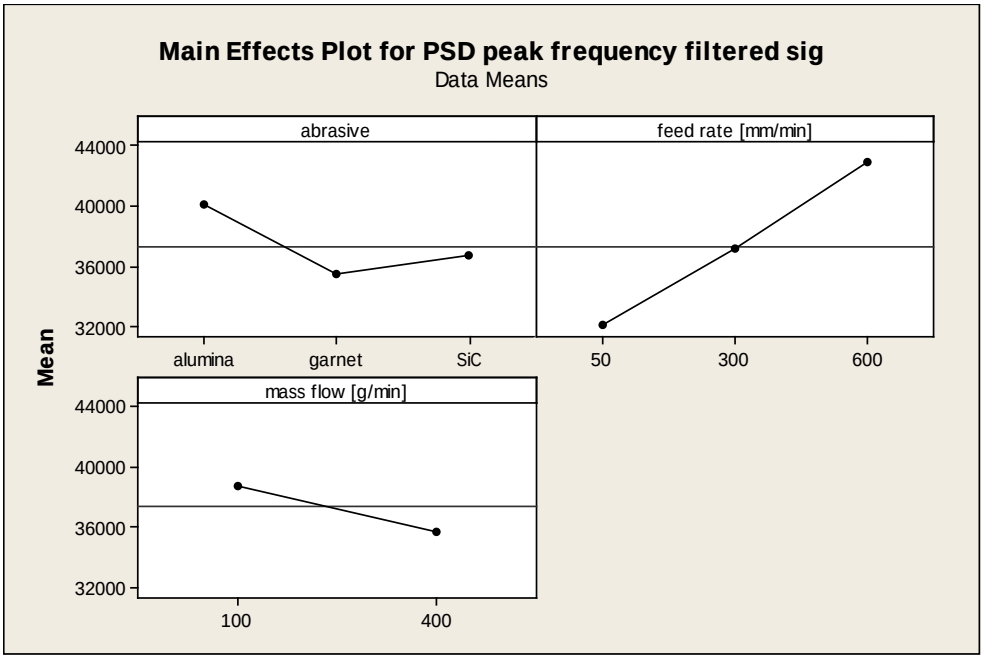

Figure B.17: Main effect plot of filtered signal PSD peak frequency

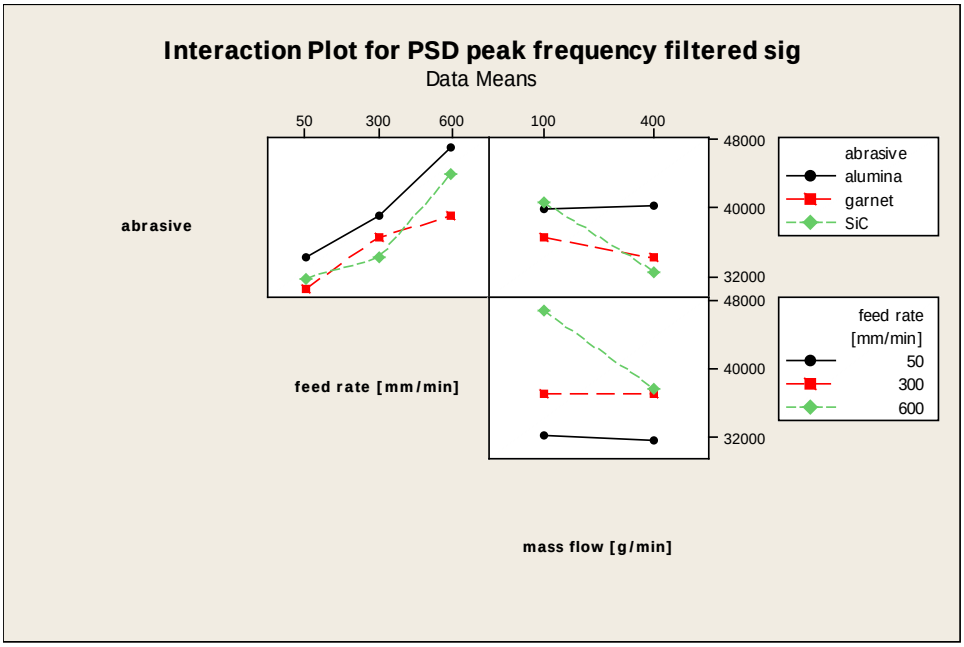

Figure B.18: Interaction plot of filtered signal PSD peak frequency

The ANOVA table is the following:

General Linear Model: PSD peak frequency versus Sheet; abrasive; ...

Factor	Type	Levels	Values
Sheet	fixed	2	1; 2
abrasive	fixed	3	alumina; garnet; SiC
feed rate [mm/min]	fixed	3	50; 300; 600
mass flow [g/min]	fixed	2	100; 400

Analysis of Variance for PSD peak frequency filtered sig, using Adjusted SS for Tests

Source	DF	Seq SS	Adj SS	Adj MS	F	P
Sheet	1	37536735	24513808	24513808	1.03	0.328
abrasive	2	106902034	97241306	48620653	2.05	0.168
feed rate [mm/min]	2	531302763	483753544	241876772	10.21	0.002
mass flow [g/min]	1	56405827	81790624	81790624	3.45	0.086
abrasive*feed rate [mm/min]	4	47218851	40592063	10148016	0.43	0.786
abrasive*mass flow [g/min]	2	62502093	56413626	28206813	1.19	0.335
feed rate [mm/min]*mass flow [g/min]	2	100095230	100095230	50047615	2.11	0.161
Error	13	308031018	308031018	23694694		
Total	27	1249994550				

S = 4867.72 R-Sq = 75.36% R-Sq(adj) = 48.82%

The ANOVA shows that only the feed rate is significant as its p-value is lower than the α value set to 5%. With a p-value of 0.328, the block results not relevant and results are not influenced by a change in material sheet. It is necessary to verify the statistical hypothesis of ANOVA: the test of normality of the residuals (**Figure B.19**) and the independence of the residuals (**Figure B.20**). The test of equal variances cannot be performed as there are no replicates.

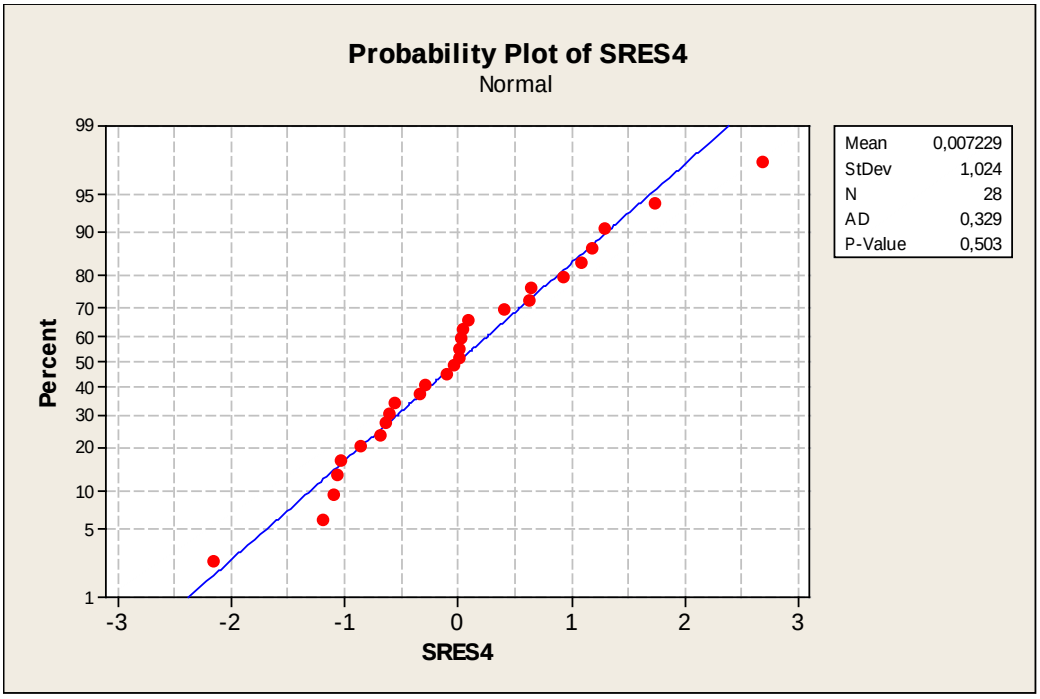

Figure B.19: Filtered signal PSD peak frequency residuals normality test

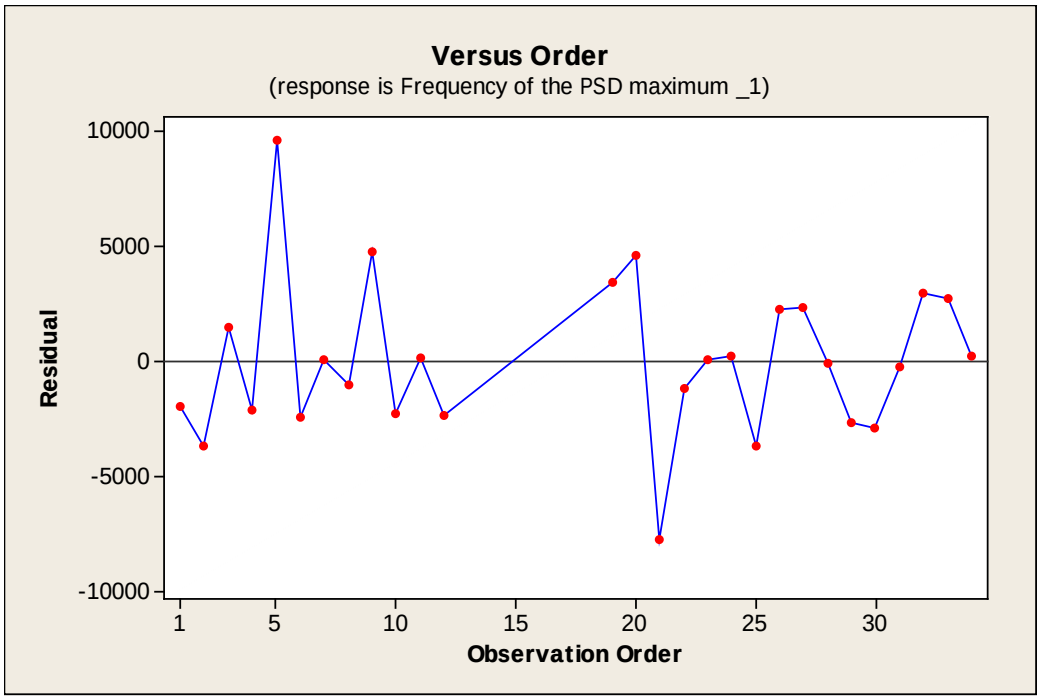

Figure B.20: Filtered signal PSD peak frequency Standardized residuals vs Run order graph

Residuals are normal since the p-value is higher than 0.05 and independent since the graph Standardized residuals vs Run order shows no specific trends. The ANOVA results are acceptable.

Appendix C

Matlab Code for Signal Analysis

The following Appendix will present the Matlab code used in the signal analysis described in **Chapter 4**.

```
clc
close all
clear all


[acquired_signal path]=uigetfile('.txt');
cd(path);
signal = load(acquired_signal);
[row column]=size(signal); % Dimensions of the signal vector


%% General data

signal_length = length(signal); % Length of the acquired signal
vector
f_samp = 2500000; % Acquisition frequency in Hz
dt = 1/f_samp;    % Distance in time domain between each point
in seconds
cut_length = 10; % Length of the cut in mm
feed_rate = 600; % Jet feed rate in mm/min
cut_duration = cut_length/feed_rate * 60 ; % Duration of the cut
in seconds
acquisition_duration = signal_length*dt;   % Duration of the
acquisition in seconds


%% Time domain plot

time_vector = [0:1:row-1]*dt; % Vector of time domain axis
f1=figure()
plot(time_vector,signal)      % Plot of signal in time domain
title('Raw signal vs time');
ylabel('signal [27]');
xlabel('time [19]');
ylim([-12 12])
```

```
%% FFT noise, RMS noise

Fs = 2500000;     % Sampling frequency
T = 1/Fs;         % Sample time span
start_time=0;     % Beginning of signal of interest in seconds
end_time=1;       % End of signal of interest in seconds
L =(end_time-start_time)*2.5e6;  % Length of signal
t = (0:L-1)*T;                   % Time vector
f_res = Fs/L;                    % Ffrequency resolution
noise=signal(1+start_time*2.5e6:end_time*2.5e6); % Extraction of
a portion of noise

Y_noise= fft(noise)/L;                     % FFT of noise
f = 0:f_res:(L/2)*f_res;                   % Frequency axis
mod_noise=abs(Y_noise(1:L/2+1));           % Module of FFT
modnorm_noise(1)= mod_noise(1);            % Module normalization
modnorm_noise(2:L/2)= 2*mod_noise(2:L/2); % Module normalization
modnorm_noise(L/2+1)= mod_noise(L/2+1);    % Module normalization


% Plot of noise vs time
time_vector = [1:L]*dt; % Vector of time domain axis
f2=figure()
plot(time_vector,noise) % Plot of signal in time domain
title('Noise signal vs time');
ylabel('signal [27]');
xlabel('time [19]');
ylim([-12 12])

% Plot single-sided amplitude spectrum of noise
f3=figure()
plot(f, modnorm_noise)
title('Single-Sided Amplitude Spectrum of y(t) noise')
xlabel('Frequency (Hz)')
ylabel('|Y(f)| [27]')

% Noise RMS
rms_noise=rms(noise);
```

```
%% FFT signal, RMS signal

Fs = 2500000;      % Sampling frequency
T = 1/Fs;          % Sample time span
start_time=3.2;    % Beginning of signal of interest in seconds
(must be changed according to the signal)
end_time=3.7;      % End of signal of interest in seconds (must
be changed according to the signal)
L =(end_time-start_time)*2.5e6;     % Length of signal
t = (0:L-1)*T;                      % Time vector
f_res = Fs/L;                       % Frequency resolution
signal_new=signal(1+start_time*2.5e6:end_time*2.5e6);%
Extraction of a portion of signal

Y_sig= fft(signal_new)/L;           % FFT of noise
f = 0:f_res:(L/2)*f_res;            % Frequency axis
mod_signal=abs(Y_sig(1:L/2+1));    % Discard half part of the
FFT
modnorm_signal(1)= mod_signal(1);  % Module normalization
modnorm_signal(2:L/2)= 2*mod_signal(2:L/2); % Module
normalization
modnorm_signal(L/2+1)= mod_signal(L/2+1);   % Module
normalization

% Plot of signal vs time
time_vector = [1:L]*T;      % Vector of time domain axis
f4=figure()
plot(time_vector,signal_new) % Plot of signal in time domain
title('Extracted raw signal vs time');
ylabel('signal [27]');
xlabel('time [19]');
ylim([-12 12])

% Plot single-sided amplitude spectrum of machining
f5=figure()
plot(f, modnorm_signal)
title('Single-Sided Amplitude Spectrum of y(t) extracted raw
signal')
xlabel('Frequency (Hz)')
ylabel('|Y(f)| [27]')

% Signal RMS

rms_signal=rms(signal_new);
```

```
%% Equiripple Lowpass filter designed using the FIRPM function.

% All frequency values are in kHz.
Fs = 2500;  % Sampling Frequency

Fpass = 200;              % Passband Frequency
Fstop = 300;              % Stopband Frequency
Dpass = 0.0057563991496;  % Passband Ripple
Dstop = 1e-05;            % Stopband Attenuation
dens  = 20;               % Density Factor

% Calculate the order from the parameters using FIRPMORD.
[N, Fo, Ao, W] = firpmord([Fpass, Fstop]/(Fs/2), [1 0], [Dpass,
Dstop]);

% Calculate the coefficients using the FIRPM function.
b  = firpm(N, Fo, Ao, W, {dens});
Hd1 = dfilt.dffir(b);


%% Filtering

signal_filtered=filter(Hd1, signal);

% Plot in time domain
time_vector = [0:1:row-1]*dt; % Vector of time domain axis
f6=figure()
plot(time_vector,signal_filtered) % Plot of signal in time
domain
title('Filtered signal vs time');
ylabel('signal [27]');
xlabel('time [19]');
ylim([-12 12])
```

```
%% FFT of filtered signal

Fs = 2500000;                    % Sampling frequency
T = 1/Fs;                        % Sample time
start_time=3.2;                  % Beginning of signal of
interest in seconds (must be changed according to the signal)
end_time=3.7;                    % End of signal of interest in
seconds (must be changed according to the signal)
L =(end_time-start_time)*2.5e6; % Length of signal
t = (0:L-1)*T;                   % Time vector
f_res = Fs/L;                    % Frequency resolution
signal_new_filtered=signal_filtered(1+start_time*2.5e6:end_time*
2.5e6);    % Extraction of a portion of signal


Y_sig_filtered= fft(signal_new_filtered)/L; %FFT of filtered
signal
f = 0:f_res:(L/2)*f_res;  % Frequency axis
mod_sig_filtered=abs(Y_sig_filtered(1:L/2+1));  % Discard half
part of the FFT
modnorm_signal_filtered(1)= mod_sig_filtered(1);
% Module normalization
modnorm_signal_filtered(2:L/2)= 2*mod_sig_filtered(2:L/2);
% Module normalization
modnorm_signal_filtered(L/2+1)= mod_sig_filtered(L/2+1);
% Module normalization

% Plot single-sided amplitude spectrum of machining
f7=figure()
plot(f, modnorm_signal_filtered)
title('Single-Sided Amplitude Spectrum of y(t) extracted
filtered signal')
xlabel('Frequency (Hz)')
ylabel('|Y(f)| [27]')

% RMS of filtered signal
rms_signal_filtered=rms(signal_new_filtered);
```

```
%% mobile windows RMS

%calculation of RMS in smaller windows
k=0;   % Counter
n=200; % Number of data in each window
L=length(signal_new); % Signal length
w=L/n; % Number of windows
w_time=n/f_samp;   % Duration in [19] of each window

for i=1:w

rms_filtered_window(i)=rms(signal_new_filtered(1+k*n:(k+1)*n));%
RMS of filtered signal in each window
        rms_window(i)=rms(signal_new(1+k*n:(k+1)*n)); % RMS of
original signal in each window
        k=k+1;   % Increase counter
end


% Plot of signal RMS vs window number
f8=figure()
plot((1:w)*w_time,rms_window)  % Plot of rms vs window number
title('windowed RMS of raw extracted signal vs time');
xlabel('time [19]')
ylabel('rms [V^2]')
grid on

% Plot of filtered signal RMS vs window number
f9=figure()
plot((1:w)*w_time,rms_filtered_window)  % Plot of RMS vs window
number
title('windowed RMS of extracted filtered signal vs time');
xlabel('time [19]')
ylabel('rms [V^2]')
grid on
```

```
%% PSD with pwelch

window_points=128; % Points in each window
n_overlap=64;      % Number of points which overlaps
NFFT=512;          % Number of points in frequency domain
Fs=2500000;        % Sampling frequency

[Pxx_signal,freq_signal] =
pwelch(signal_new,window_points,n_overlap, NFFT,Fs);   % PSD of
original signal, f is [0,fs/2]
[Pxx_signal_filtered,freq_signal_filtered] =
pwelch(signal_new_filtered,window_points,n_overlap,NFFT,Fs);
% PSD of filtered signal, f is [0,fs/2]

% Plot of PSD of original signal
f10=figure()
plot(freq_signal,Pxx_signal)
title('PSD of raw extracted signal');
xlabel('frequencies [Hz]')
ylabel('PSD [V^2/Hz] ')

% Plot of PSD of filtered signal
f11=figure()
plot(freq_signal_filtered,Pxx_signal_filtered)
title('PSD of extracted filtered signal');
xlabel('frequencies [Hz]')
ylabel('PSD [V^2/Hz] ')


Pxx_signal_db=pow2db(Pxx_signal);    % Convert amplitude in dB
Pxx_signal_filtered_db=pow2db(Pxx_signal_filtered);   % Convert
amplitude in dB

% Plot of PSD of original signal in dB
f12=figure()
plot(freq_signal,Pxx_signal_db)
title('PSD of extracted raw signal');
xlabel('frequencies [Hz]')
ylabel('PSD [dB/Hz] ')

% Plot of psd of filtered signal in dB
f13=figure()
plot(freq_signal_filtered,Pxx_signal_filtered_db)
title('PSD of extracted filtered signal');
xlabel('frequencies [Hz]')
```

```
ylabel('PSD [dB/Hz] ')



%% Frequency of PSD peak

[max_PSD_signal, max_index_signal] = max(Pxx_signal);  % Maximum
value and position into array of the maximum in PSD of raw
signal
[max_PSD_signal_filtered, max_index_signal_filtered] =
max(Pxx_signal_filtered);    % Maximum value and position into
array of the maximum in PSD of filtered signal

freq_max_signal = freq_signal(max_index_signal); % Frequency of
the maximum value and position into array of the maximum in PSD
of raw signal
freq_max_signal_filtered =
freq_signal_filtered(max_index_signal_filtered); % Frequency of
the maximum value and position into array of the maximum in PSD
of filtered signal

%% Area of PSD from 0 to 200 kHz

k=200000; % Right limit of integration in Hz
[min_difference, array_position] = min(abs(freq_signal - k)); %
Find the index of the frequency in frequency array closest to
200 kHz
spacing=freq_signal(2)-freq_signal(1);

data=Pxx_signal(1:array_position); % Extraction of data from PSD
data of original signal
data_filtered=Pxx_signal_filtered(1:array_position);
% Extraction of data from PSD data of filtered signal
area=trapz(data)*spacing;   % Area of  PSD of original signal
from 0 to 200 kHz
area_filtered=trapz(data_filtered)*spacing; % Area of  PSD of
filtered signal from 0 to 200 kHz
```

```
%% Save graphs to excel worksheet

% First open an Excel Server
Excel = actxserver('Excel.Application');
set(Excel, 'Visible', 1);

% Insert a new workbook
Workbooks = Excel.Workbooks;
Workbook = invoke(Workbooks, 'Add');

% Make the second sheet active
Sheets = Excel.ActiveWorkBook.Sheets;
sheet1 = get(Sheets, 'Item', 1);
invoke(sheet1, 'Activate');


% Paste figures from matlab to excel sheet 1
print(f1, '-dbitmap'); sheet1.Range('A1').PasteSpecial; %time
domain plot
print(f6, '-dbitmap'); sheet1.Range('J1').PasteSpecial;

print(f2, '-dbitmap'); sheet1.Range('A22').PasteSpecial; %time
domain plot of sections
print(f14, '-dbitmap'); sheet1.Range('J22').PasteSpecial;
print(f4, '-dbitmap'); sheet1.Range('T22').PasteSpecial;

print(f3, '-dbitmap'); sheet1.Range('A45').PasteSpecial; %FFT
print(f5, '-dbitmap'); sheet1.Range('J45').PasteSpecial;
print(f7, '-dbitmap'); sheet1.Range('T45').PasteSpecial;

print(f8, '-dbitmap'); sheet1.Range('A70').PasteSpecial; %RMS
print(f9, '-dbitmap'); sheet1.Range('J70').PasteSpecial;

print(f10, '-dbitmap'); sheet1.Range('A90').PasteSpecial; %PSD
in V^2/Hz
print(f11, '-dbitmap'); sheet1.Range('J90').PasteSpecial;

print(f12, '-dbitmap'); sheet1.Range('A115').PasteSpecial; %PSD
in dB/Hz
print(f13, '-dbitmap'); sheet1.Range('J115').PasteSpecial;
```

```
%% Save data to excel

% Make the second sheet active
Sheets = Excel.ActiveWorkBook.Sheets;
sheet2 = get(Sheets, 'Item', 2);
invoke(sheet2, 'Activate');

% Get a handle to the active sheet
Activesheet = Excel.Activesheet;

% scrivi i dati
ActivesheetRange = get(Activesheet,'Range','A1');
set(ActivesheetRange, 'Value', 'Average RSM noise');
ActivesheetRange = get(Activesheet,'Range','B1');
set(ActivesheetRange, 'Value', rms_noise);
ActivesheetRange = get(Activesheet,'Range','C1');
set(ActivesheetRange, 'Value', 'V^2');

ActivesheetRange = get(Activesheet,'Range','A2');
set(ActivesheetRange, 'Value', 'Average RSM extracted raw
signal');
ActivesheetRange = get(Activesheet,'Range','B2');
set(ActivesheetRange, 'Value', rms_signal);
ActivesheetRange = get(Activesheet,'Range','C2');
set(ActivesheetRange, 'Value', 'V^2');

ActivesheetRange = get(Activesheet,'Range','A3');
set(ActivesheetRange, 'Value', 'Average RSM jet signal');
ActivesheetRange = get(Activesheet,'Range','B3');
set(ActivesheetRange, 'Value', rms_jet);
ActivesheetRange = get(Activesheet,'Range','C3');
set(ActivesheetRange, 'Value', 'V^2');

ActivesheetRange = get(Activesheet,'Range','A4');
set(ActivesheetRange, 'Value', 'Average RSM extracted filtered
signal');
ActivesheetRange = get(Activesheet,'Range','B4');
set(ActivesheetRange, 'Value', rms_signal_filtered);
ActivesheetRange = get(Activesheet,'Range','C4');
set(ActivesheetRange, 'Value', 'V^2');

ActivesheetRange = get(Activesheet,'Range','A5');
set(ActivesheetRange, 'Value', 'Maximum value PSD extracted raw
signal');
ActivesheetRange = get(Activesheet,'Range','B5');
```

```
set(ActivesheetRange, 'Value', max_PSD_signal);
ActivesheetRange = get(Activesheet,'Range','C5');
set(ActivesheetRange, 'Value', 'V^2');

ActivesheetRange = get(Activesheet,'Range','A6');
set(ActivesheetRange, 'Value', 'Frequency of the PSD maximum in
raw signal');
ActivesheetRange = get(Activesheet,'Range','B6');
set(ActivesheetRange, 'Value', freq_max_signal);
ActivesheetRange = get(Activesheet,'Range','C6');
set(ActivesheetRange, 'Value', 'Hz');

ActivesheetRange = get(Activesheet,'Range','A7');
set(ActivesheetRange, 'Value', 'Maximum value PSD extracted
filtered signal');
ActivesheetRange = get(Activesheet,'Range','B7');
set(ActivesheetRange, 'Value', max_PSD_signal_filtered);
ActivesheetRange = get(Activesheet,'Range','C7');
set(ActivesheetRange, 'Value', 'V^2');

ActivesheetRange = get(Activesheet,'Range','A8');
set(ActivesheetRange, 'Value', 'Frequency of the PSD maximum in
filtered signal');
ActivesheetRange = get(Activesheet,'Range','B8');
set(ActivesheetRange, 'Value', freq_max_signal_filtered);
ActivesheetRange = get(Activesheet,'Range','C8');
set(ActivesheetRange, 'Value', 'Hz');

ActivesheetRange = get(Activesheet,'Range','A9');
set(ActivesheetRange, 'Value', 'Area of the PSD of raw signal
[0,200 kHz]');
ActivesheetRange = get(Activesheet,'Range','B9');
set(ActivesheetRange, 'Value', area);
ActivesheetRange = get(Activesheet,'Range','C9');
set(ActivesheetRange, 'Value', 'V^2');

ActivesheetRange = get(Activesheet,'Range','A10');
set(ActivesheetRange, 'Value', 'Area of the PSD of filtered
signal [0,200 kHz]');
ActivesheetRange = get(Activesheet,'Range','B10');
set(ActivesheetRange, 'Value', area_filtered);
ActivesheetRange = get(Activesheet,'Range','C10');
set(ActivesheetRange, 'Value', 'V^2');

ActivesheetRange = get(Activesheet,'Range','A11');
set(ActivesheetRange, 'Value', 'Start of extraction of signal');
ActivesheetRange = get(Activesheet,'Range','B11');
set(ActivesheetRange, 'Value', start_time);
ActivesheetRange = get(Activesheet,'Range','C11');
set(ActivesheetRange, 'Value', 's');
```

```
ActivesheetRange = get(Activesheet,'Range','A12');
set(ActivesheetRange, 'Value', 'End of extraction of signal');
ActivesheetRange = get(Activesheet,'Range','B12');
set(ActivesheetRange, 'Value', end_time);
ActivesheetRange = get(Activesheet,'Range','C12');
set(ActivesheetRange, 'Value', 's');

ActivesheetRange = get(Activesheet,'Range','A13');
set(ActivesheetRange, 'Value', 'Start of extraction of jet
signal');
ActivesheetRange = get(Activesheet,'Range','B13');
set(ActivesheetRange, 'Value', start_time_jet);
ActivesheetRange = get(Activesheet,'Range','C13');
set(ActivesheetRange, 'Value', 's');

ActivesheetRange = get(Activesheet,'Range','A14');
set(ActivesheetRange, 'Value', 'End of extraction of jet
signal');
ActivesheetRange = get(Activesheet,'Range','B14');
set(ActivesheetRange, 'Value', end_time_jet);
ActivesheetRange = get(Activesheet,'Range','C14');
set(ActivesheetRange, 'Value', 's');

ActivesheetRange = get(Activesheet,'Range','A15');
set(ActivesheetRange, 'Value', 'feed rate');
ActivesheetRange = get(Activesheet,'Range','B15');
set(ActivesheetRange, 'Value', feed_rate);
ActivesheetRange = get(Activesheet,'Range','C15');
set(ActivesheetRange, 'Value', 'mm/min');

ActivesheetRange = get(Activesheet,'Range','A16');
set(ActivesheetRange, 'Value', 'cut duration (circa)');
ActivesheetRange = get(Activesheet,'Range','B16');
set(ActivesheetRange, 'Value', cut_duration);
ActivesheetRange = get(Activesheet,'Range','C16');
set(ActivesheetRange, 'Value', 's');

ActivesheetRange = get(Activesheet,'Range','A17');
set(ActivesheetRange, 'Value', 'maximum of FFT');
ActivesheetRange = get(Activesheet,'Range','B17');
set(ActivesheetRange, 'Value', max_FFT_signal);
ActivesheetRange = get(Activesheet,'Range','C17');
set(ActivesheetRange, 'Value', 'V^2');


ActivesheetRange = get(Activesheet,'Range','A18');
set(ActivesheetRange, 'Value', 'frequency of the maximum of
FFT');
ActivesheetRange = get(Activesheet,'Range','B18');
set(ActivesheetRange, 'Value', max_freq_FFT);
ActivesheetRange = get(Activesheet,'Range','C18');
```

```
set(ActivesheetRange, 'Value', 'Hz');

invoke(Workbook, 'SaveAs', file_name.xls');
```

D. Datasheets

In this Appendix, the data sheet of water jet system and technical instruments are presented.

D.1 Water jet cutting system

The machine is made of an Ormond 5-axis CNC programmable cutting system and a KMT Streamline SL-V 100D pump (**Figure D.1**)

Table D.1: Water jet cutting system datasheet

Motion system	Ormond 5-axis cutting system
Pump	KMT Streamline SL-V 100D
Cutting range	X = 1.8 m, Y = 1.8 m, Z = 1 m
Maximum operating pressure	380 MPa
Maximum feed rate	20000 mm/min
Position accuracy	±0.01 mm
Electrical power consumption	75 kW

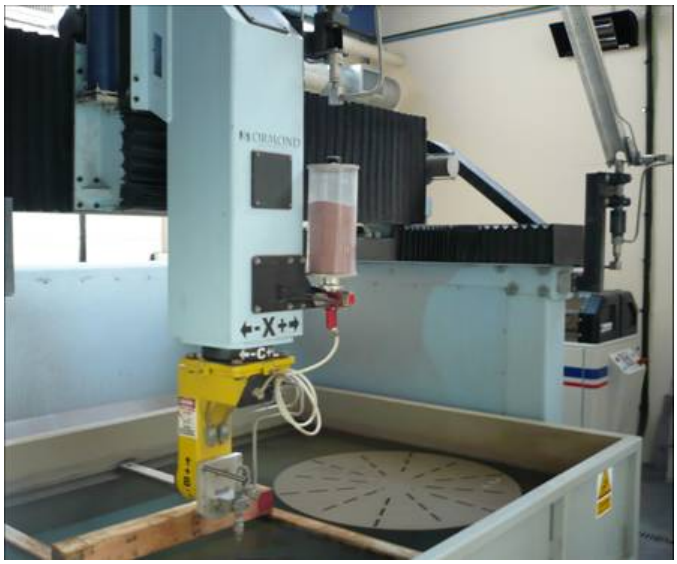

Figure D.1: Water jet cutting system at University of Nottingham

D.2 Optical microscope

The optical microscope used is a Keyence VHX-100K (**Figure D.2**)

Table D.2: Keyence VHX - 100K optical microscope datasheet

Name	Keyence VHX-100K
Image pick-up element	1/2-inc, 2.11-million-pixel CCD image sensor
Number of pixels	1688 (H) x 1248 (V)
Scan method	Interlace
Light source	12 V, 100 W, Halogen lamp
Video output	Analog RGB (1600 x 1200 pixels)

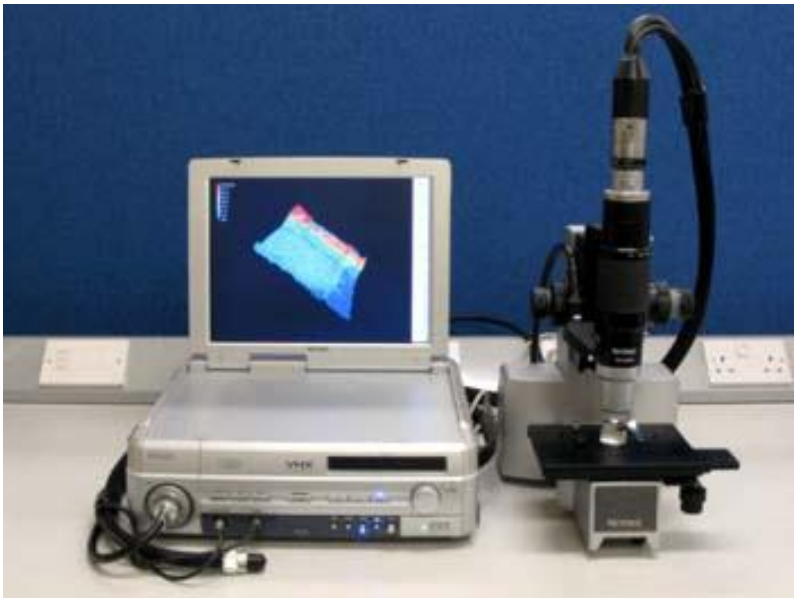

Figure D.2: Keyence VHX-100K optical microscope

D.3 Profilometer

The Taylor-Hobson Talysurf CLI 1000 (**Figure D.3**) has been used to measure the surface and evaluate the roughness parameters.

Table D.3: Taylor-Hobson Talysurf CLI 1000 datasheet

Name	Taylor-Hobson Talysurf CLI 1000
Measuring capacity	X: 100 mm, Y: 100 mm, Z = 100 mm
Axis resolution (data spacing)	X: 0.5 µm, Y: 0.5 µm
Gauge type	Laser triangulation
Scanning frequency	2000 Hz
Vertical resolution	1 µm
Lateral resolution	30 µm

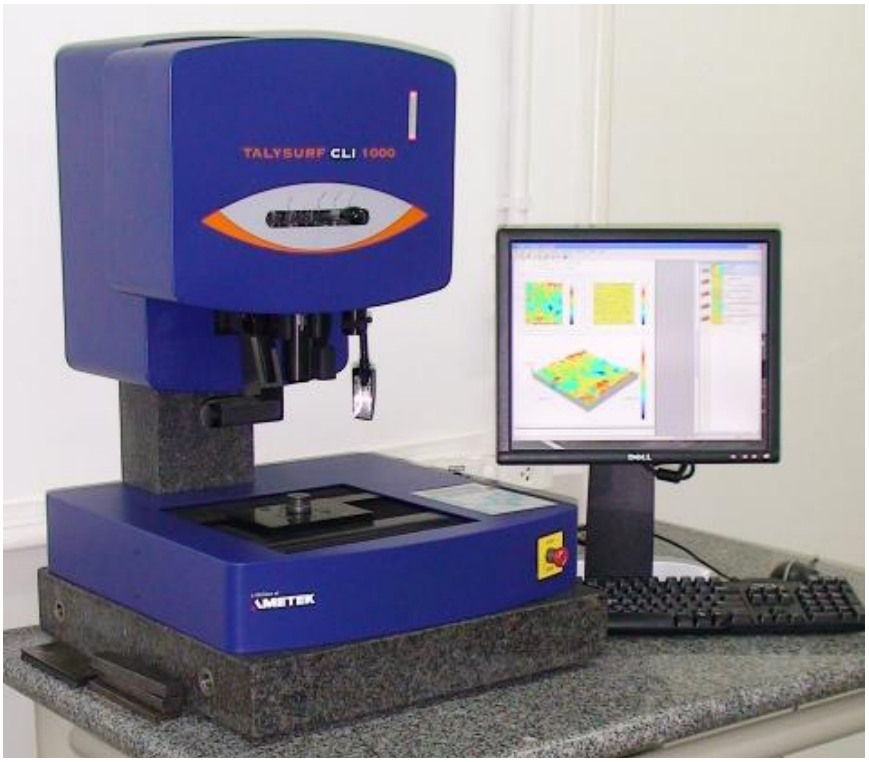

Figure D.3: Taylor-Hobson Talysurf CLI 1000

D.4 Scanning electron microscope

The scanning electron microscope is a Philips XL 30 ESEM-FEG (**Figure D.4**). The datasheet is presented in **Table D.4**

Table D.4: Philips XL 30 ESEM-FEG

Name	Philips XL 30 ESEM-FEG
Performance resolution	1.5 nm at 10 kV or higher, 2.5 nm at 1kV
Electron source	Schottky-based thermionic field emission electron gun
Beam current range	1 pA – 25 nA
Beam acceleration voltage	Continuously variable from 0.2 to 30 kV
Magnification range	20X – 80.000X
Chamber pressure	Gun chamber: $2x10^{-7}$ Pa, Specimen chamber: $2x10^{-5}$ Pa
Specimen chamber diameter	284 mm
Analytical capabilities	Secondary electron (SE) detector Back-scattered electron (BSE) detector Energy dispersive X-ray spectrometer (EDS)

Figure D.4: Philips XL 30 ESEM-FEG

List of Figures

List of Tables

Bibliography

[1] I. Finnie, J. Wolak, Y. Kabil, Erosion of metals by solid particles, *Journal of materials*, Vol 2. (1967), pp. 682-700

[2] I. Finnie, The mechanism of erosion of ductile metals, *Proceedings of the 3rd U.S. national congress of applied mechanics*, 1958, ASME, pp.527-532

[3] M. Hahish, The effect of beam angle in abrasive water jet machining, *Journal of engineering for industry*, Vol. 115 (1993), pp. 51-56

[4] M. Hashish, A modeling study of metal cutting with abrasive waterjets, *Journal of engineering materials and technology*, Vol. 106 (1984), pp. 88-100

[5] M. Hashish, Aspects of abrasive waterjet performance optimization, *Proceedings of the 8th international symposium on jet cutting technology*, England (1986), pp. 297-308

[6] P.J. Slikkerveer, P.C.P. Bouten, F.H in't Veld, H. Scholter, Erosion and damage by sharp particles, *Wear*, Vol. 217 (1998), pp. 237–250

[7] I. Kleis, P. Kulu, Solid Particle Erosion: Occurrence, Prediction and Control, Springer, 2007

[8] H.T. Zhu, C.Z. Huang, J. Wang, Q.L. Li, C.L. Che, Experimental study on abrasive waterjet polishing for hard–brittle materials, *International journal of machine tools and manufacture*, Vol. 49 (2009), pp. 569–578

[9] P. Gudimetla, J. Wang, W. Wong, Kerf formation analysis in the abrasive waterjet cutting of industrial ceramics, *Journal of materials processing technology*, Vol. 128 (2002), pp. 123–129

[10] L. Kahlman, K.M.C. Ojmertz, L.K.L. Falk, Abrasive-waterjet testing of thermo-mechanical wear of ceramics, *Wear*, Vol. 248 (2001), pp. 16–28

[11] A. El-Domiaty, A. Abdel-Rahman, Fracture mechanics-based model of abrasive waterjet cutting for brittle materials, The international journal of advanced manufacturing technology, Vol. 13 (1997), pp. 172-181

[12] J. Zeng, T. J. Kim, An erosion model of polycrystalline ceramics in abrasive waterjet cutting, *Wear*, Vol. 193 (1996), pp. 207-217

[13] D.A. Axinte, D.S. Srinivasu, M.C. Kong, P.W. Butler-Smith, Abrasive waterjet cutting of polycrystalline diamond: a preliminary investigation, *International journal of machine tools and manufacture*, Vol. 49 (2009), pp. 797-803

[14] P.H. Shipway, I.M. Hutchings, The role of particle properties in the erosion of brittle materials, *Wear*, Vol. 193 (1996), pp. 105-113

[15] S. Srinivasan, R.O. Scattergood, Effect of erodent hardness on brittle material, *Wear*, Vol. 128 (1988), pp. 139-152

[16] A.W. Momber, R. Kovacevic, Hydro-abrasive erosion of refractory ceramics, *Journal of materials science*, Vol. 38 (2003), pp. 2861 – 2874

[17] A.W. Momber, Fluid jet erosion as a non-linear fracture process: a discussion, *Wear*, Vol. 250 (2001), pp. 100–106

[18] H. Hocheng, K.R. Chang, Material removal analysis in abrasive waterjet cutting of ceramic plates, *Journal of materials processing technology*, Vol. 40 (1994), pp. 287-304

[19] U. Çaydaş, A. Hasçalık, A study on surface roughness in abrasive waterjet machining process using artificial neural networks and regression analysis method, *Journal of material processing technology*, Vol. 202 (2008), pp. 574 - 582.

[20] M. Annoni, F. Arleo, A. Trolli, A. Suarez, A. Alberdi, Fine abrasive water jet machining of piezoelectric ceramics: cutting parameters optimization, BHR Group conference, 2012

[21] M.Monno, M. Annoni, C. Ravasio, *Water jet, a flexible technology*, Polipress, 2007

[22] http://www.waterjets.org/

[23] Appunti del corso *Laboratorio di Tecnologie Speciali*

[24] M. Monno, Tecnologia water jet / abrasive water jet, Technical report, Politecnico di Milano - Dipartimento di Meccanica.

[25] http://www.gardella-srl.it/

[26] M. Hashish, Pressure effects in abrasive-waterjet (AWJ) machining, *Journal of engineering materials and technology*, Vol. 111 (1989), pp. 221-228

[27] W.A Momber, R. Kovacevic, *Principles of abrasive water jet machining*, Springer, 1998

[28] H.T. Liu, E. Schubert, Micro abrasive-waterjet technology, OMAX Corporation, white paper

[29] http://www.wardjet.com/5-axis.html

[30] D.A Axinte, J.P Stepanian, M.C. Kong, J. McGourlay, Abrasive waterjet turning-An efficient method to profile and dress grinding wheels, *International journal of machine tools and manufacture*, Vol. 49 (2009), pp. 351-356

[31] http://www.mmsonline.com/articles/milling-with-waterjet

[32] http://www.conformjet.eu/

[33] W.C. Emmens, Water jet forming of steel beverage cans, *International journal of machine tools and manufacture*, Vol. 46 (2006), pp. 1243-1247

[34] L. Denissen, V. Massaut, J. Dadoumont, H. Davain, High pressure abrasive water jet cutting as a dismantling tool, *Proceedings of the international conference on radioactive waste management and environmental remediation,* ICEM, 2002, pp. 1603-1608

[35] A. Guha, R.M. Barron, R. Balachandar, Experimental and numerical study of water jet cleaning process, *Journal of material processing technology*, Vol. 211 (2011), pp. 610-618

[36] D.D. Arolda, M.L McCain, Abrasive waterjet peening: a new method of surface preparation for metal orthopedic implants, *Journal of biomedical materials research*, Vol. 53 (2000), pp. 536-546

[37] J. Yang, *An introduction to the theory of piezoelectricity,* Springer, 2005

[38] http://resources.edb.gov.hk

[39] http://download.springer.com/static/pdf/838/bbm%253A978-94-007-0579-1%252F1.pdf?auth66=1354536076_95b9bc2dabd493b8d0af378cd8e1e32e&ext=.pdf

[40] http://www.piceramic.com/

[41] http://www.americanpiezo.com/

[42] http://www.noliac.com/

[43] http://www.ramtron.com/

[44] http://www.piceramic.com/piezo_materials_2.php

[45] http://www.piezo.com

[46] http://www.meas-spec.com/

[47] D. Aquaro, C. Fontani, Erosion of ductile and brittle materials, *Meccanica*, Vol. 36 (2001), pp. 651–661

[48] M.M. Chaudhri, S.M. Walley, A high-speed photographic investigation of the impact damage in soda-lime and borosilicate glasses by small glass and steel spheres, *Symposium on fracture mechanics of ceramics*, 1978, pp. 349-364

[49] J. Zeng, T.J. Kim, A study of brittle mechanism applied to abrasive waterjet process, *Proceedings of the 10th international symposium on jet cutting technology*, Amsterdam (1990), pp. 115-133

[50] http://www.barton.com/

[51] ISO 4288-1996

[52] R. Groppetti, T. Gutema, A. D. Lucchio, A contribution to the analysis of some kerf quality attributes for precision abrasive waterjet cutting, *14th international conference on jetting technology*, Belgium (1998)

[53] http://en.wikipedia.org/wiki/Decibel#Examples

Acknowledgements

The author would like to acknowledge the support of Politecnico di Milano and University of Nottingham for providing the materials and instrumentation used in the experimentation.
A special thanks to Prof. Massimiliano Annoni, Prof. Dragos Axinte and Dr. Amir Rabani for their precious support during the work.